Wachsmuth *et al. Epigenetics & Chromatin (2016) 9:57*
DOI 10.1186/s13072-016-0093-1

Epigenetics & Chromatin

RESEARCH

Open Access

Dynamic properties of independent chromatin domains measured by correlation spectroscopy in living cells

Malte Wachsmuth[1*], Tobias A. Knoch[2] and Karsten Rippe[3]

Abstract

Background: Genome organization into subchromosomal topologically associating domains (TADs) is linked to cell-type-specific gene expression programs. However, dynamic properties of such domains remain elusive, and it is unclear how domain plasticity modulates genomic accessibility for soluble factors.

Results: Here, we combine and compare a high-resolution topology analysis of interacting chromatin loci with fluorescence correlation spectroscopy measurements of domain dynamics in single living cells. We identify topologically and dynamically independent chromatin domains of ~1 Mb in size that are best described by a loop-cluster polymer model. Hydrodynamic relaxation times and gyration radii of domains are larger for open (161 ± 15 ms, 297 ± 9 nm) than for dense chromatin (88 ± 7 ms, 243 ± 6 nm) and increase globally upon chromatin hyperacetylation or ATP depletion.

Conclusions: Based on the domain structure and dynamics measurements, we propose a loop-cluster model for chromatin domains. It suggests that the regulation of chromatin accessibility for soluble factors displays a significantly stronger dependence on factor concentration than search processes within a static network.

Keywords: Chromatin structure, Polymer model, Chromatin conformation capture carbon copy (5C), Targeted chromatin capture (T2C), Fluorescence correlation spectroscopy (FCS), Quantitative microscopy

Background

The three-dimensional organization of chromosomes of eukaryotic interphase cells is emerging as an important parameter for the regulation of genomic function [1–4]. Beyond the mere storage of genetic information, the spatial structure fosters its compaction, replication and transcription on all scales ranging from the single base pair (bp) to ~100 Mbp of a whole chromosome. Chromatin interaction maps obtained by the chromatin conformation capture (3C) assay [5, 6] and derived methods like 5C, Hi-C [7] or T2C [8] provide detailed genome-wide information on the three-dimensional organization of the mammalian genome for cell ensembles [9–12] or even single cells [13]. These analyses suggest that the genome is organized into distinct topologically associating domains (TADs) [3, 11, 14]. They partition the genome into repressive and active chromatin regions, also referred to as subchromosomal domains [15, 16] and as concluded from a number of microscopy studies on the topology of active gene clusters [17–19] or the timing differences between early- and late-replicating DNA loci [20]. Notably, the spatial segregation of the genome into chromatin regions with different gene expression status is not simply the result of transcriptional activity. Rather, spatial chromatin organization actively participates in shaping cellular functions [4, 21–24]. Yet, details of the folding of the nucleosome chain into subchromosomal domains or TADs and entire chromosomes remain largely elusive. For the chromatin fiber, a variety of models covering a broad range from unordered and less compact to regular and more compacted states have been suggested [25–27], and likewise, for the higher-order

---

*Correspondence: m.wachsmuth@gmx.net
[1] Cell Biology and Biophysics Unit, European Molecular Biology Laboratory (EMBL), Meyerhofstrasse 1, 69117 Heidelberg, Germany
Full list of author information is available at the end of the article

folding of the fiber there is experimental evidence for both more ordered loop- or rosette-like [12, 28–31] and less ordered, e.g., fractal globule-like topologies [10].

Despite the impressive advancements in the field, details on the organization and dynamic properties of chromatin in single living cells are elusive. However, the plasticity of chromatin organization is a central determinant of genome function as it modulates access of factors to the genome and targets them to biologically active subcompartments [32]. In addition to large-scale chromosomal movements [33], local chromatin dynamics are mostly studied by tracking of few genomic loci and chromatin-associated or chromatin-embedded molecules and particles as reviewed previously [34–37]. The resulting translocation data can be quantified as mean-squared displacement (MSD) versus time curves to extract apparent velocities or diffusion coefficients. These studies revealed spatially confined movements of tagged chromatin loci as intuitively evident for a segment of a polymer without center-of-mass translocation [38–40]. However, extending this approach to a systematic analysis of endogenous chromatin loci faces a number of limitations. Imaging-based techniques typically require the labeling of specific genomic regions using repetitive, e.g., *lac*O operator arrays integrated into the genome at random or defined positions [41]. These arrays are big compared to the dimensions of the structures under investigation and potentially alter their architecture. Furthermore, this approach is limited in its time resolution to the image acquisition time, which is typically in the range of 50 ms or higher. At the molecular level, methods like fluorescence recovery after photobleaching (FRAP), continuous photobleaching (CP) and fluorescence correlation spectroscopy (FCS) provide information on the binding of proteins to chromatin and on their mobility within the chromosomal environment on the microsecond to minute time scale [42, 43]. However, with these methods no information on the dynamics of nucleosome chains and higher-order domains has yet been obtained. While biophysical polymer models have been widely used to quantitatively describe and directly or inversely compare 3D chromatin structure to experimental data as reviewed recently [44, 45], they mostly do not include dynamics. Thus, our current knowledge is lacking both experimental information and theoretical treatment of the conformational dynamics of chromatin in vivo that is important for the understanding of the differential readout of DNA sequence information or interactions between different genomic loci.

In a number of studies, intramolecular dynamics have been investigated by FCS [46, 47]. By uncoupling the center-of-mass diffusion from higher-order relaxation modes via trapping or tracking [48, 49], a series representation of relaxation modes was obtained to describe the internal dynamics of double-stranded DNA in vitro [49–51]. In this manner, the MSD of polymer segments can be described as confined diffusion relative to the center of mass. When taking into account hydrodynamic interactions, molecules like long DNA chains with a sufficiently large ratio of contour to persistence length, i.e., 'soft' polymers, show Zimm relaxation behavior [52].

Here, we combine for the first time the topological interpretation of 3C-derived data from large ensembles of fixed cells with the measurement of mesoscale chromatin dynamics in individual living cells. We confirm the formation of loop clusters in TADs from contact probability maps (5C, T2C) from other studies ([11, 53], NCBI GEO accession GSE35721) pointing to rosettes as a prominent structural feature of such topologically independent domains. By applying FCS, we measured chromatin dynamics extracted from fluorescence intensity fluctuations by exploiting the linker histone variant H1.0 tagged with EGFP (H1-EGFP) as a proxy for chromatin movement. H1 is particularly suited for this purpose since it decorates chromatin globally and reflects its density but binds only transiently [54, 55] such that photobleached molecules are constantly replaced by fluorescent ones. We found distinct chromatin relaxation times, hallmarking the presence of dynamically and topologically independent chromatin units with an average genomic content of ~1 Mb. Treatment of cells with trichostatin A (TSA) and azide-induced ATP depletion resulted in decelerated relaxations, revealing chromatin decondensation and compaction, respectively, hence delivering insight into factors that change chromatin dynamics. Based on the experimental data, an analytical polymer model was developed. It correctly describes both the contact probability maps from 3C-based ensemble analysis and the internal dynamics of chromatin domains observed by FCS. We hypothesize that these domains might be TADs. From the dynamic properties measured, we infer that the different time scales of structural reorganization and particle dynamics provide an additional regulatory layer for targeting soluble nuclear factors to chromatin subcompartments.

Results

A loop-cluster substructure domain model shows good agreement with experimental 5C and T2C data

To gain insight into the topological organization of chromatin, we applied a simple domain and peak detection approach to 5C data of a 4.5-Mb region containing the Xist gene crucial for X inactivation in female mouse embryonic stem cells [11] and T2C data of a 2.2-Mb region of the IGF/H19 locus in human HB2 cells [8]. Figure 1a shows the analysis of the experimental 5C data set for which we confirmed the existence of TAD-like domains such as the highlighted ~1.1-Mb region that emerged as square-shaped regions of increased internal contact probability as expected [7, 11, 14, 56]. A one-dimensional projection over the whole domain region yielded primary peaks corresponding to genomic sites involved in loop formation (Additional file 1: Fig. S1). Orthogonal local projections around each so-determined peak revealed all partner sites with which it interacts to form loops. We obtained 17 primary peaks within this domain (Additional file 1: Fig. S2). Most of them also emerged in the local projections, strongly indicating that this domain consisted to a significant extent of an intricately tied loop cluster such as a rosette. We followed the same procedure for an experimental T2C data set from Knoch et al. [53] (Fig. 1b). Again, we found domains such as the highlighted ~0.95-Mb region and 15 primary peaks within this domain (Additional file 1: Fig. S3), most of which also emerged in the local projections, again indicating a rosette-like loop-cluster organization of the domain.

Domain configurations are well described with a quantitative polymer model

While these examples support the notion of loop-induced domain formation, also less ordered crumpled, globular or ordinary domain structures were suggested previously [10, 12, 44]. Accordingly, we derived a quantitative polymer model that describes 4 different domain topologies to comprehensively cover the previously proposed features of chromatin domain organization (Fig. 1c; Additional file 1: Fig. S4): Scaling laws from polymer theory [57] suggest that chromatin adopts the shape of a chain of topologically and dynamically independent domains under the semi-dilute conditions met in mammalian interphase nuclei (see Additional file 1: Supplementary Text for more details). Thus, we first assumed the formation of such blobs, i.e., globular subchains of the full chromosome that are significantly shorter and behave like independent, almost self-penetrating molecules (so-called theta-solvent conditions where repulsive and attractive segment–segment interactions compensate each other), connected with a linker. Second, the formation of space-filling fractal or crumpled globules [10, 44] was evaluated. Third, we assumed the formation of single or rosette-like branched loops [29, 30, 58, 59] under theta-solvent conditions. Fourth, the same topology was used, but under so-called good-solvent conditions where the excluded volume interaction between segments dominates and the structure appears swollen as compared to theta-solvent conditions. The physical contour length L of the chromatin fiber contained in the domain is directly related to DNA content and density, and the persistence length l_p is a measure for the fiber flexibility. Together with the number of contained loops f, these parameters determine the radius of gyration R_g, which characterizes the volume effectively occupied by the domain—Additional file 1: Eq. S14, S20, S22, S24—according to Eq. 1:

$$R_g^2 = \begin{cases} \frac{L \cdot l_p}{6}\left(\frac{2f-1}{f^2}\right) & \text{loop-rosette conformation, theta-solvent conditions,} \\ \frac{L^{6/5} \cdot l_p^{4/5}}{9.59}\left(\frac{1.92f-0.92}{f^{11/5}}\right) & \text{loop-rosette conformation, good-solvent conditions,} \\ \frac{L^{2/3} \cdot l_p^{4/3}}{1.76} & \text{globular conformation,} \\ \frac{L \cdot l_p}{3} & \text{blob conformation.} \end{cases} \tag{1}$$

An estimation of stochastic contact probabilities—Additional file 1: Eq. S25—directly allowed to compute 5C-/T2C-like contact probability maps. Figure 1d, e shows such maps for both the theta-solvent loop-cluster and the globular conformation (Additional file 1: Supplementary Text), i.e., for a 5-Mb stretch comprising 4 rosette-like loop clusters and 4 globular domains, respectively, linked with a relaxed chromatin stretch. Here too, domains emerged as square-shaped regions of increased internal contact probability. The highlighted rosette domain in Fig. 1d was computed assuming 10 loops (three with positional noise). Applying the same analysis as above allowed us to quantitatively retrieve the topological details used for the simulation: Some ties were found in both projection directions, others, especially those with positional noise, less reliably in only one direction. Using the topology retrieved, we performed Monte Carlo (MC) simulations of the domain (with one example visualized, Fig. 1d) to yield its radius of gyration of ~240 nm. The globular domain model yielded a smaller radius of gyration of 210 nm but was incompatible with the experimental data since no peaks were detected (Fig. 1e). To further validate the analysis and simulation pipeline, we used the topology obtained from the experimental 5C and T2C data to re-calculate the experimental contact probability maps, which were in good agreement with the initial ones (Additional file 1: Figs. 5, 6). From MC simulations, we found a radius of gyration of ~240 nm for the domain highlighted in the 5C data set and of ~220 nm in the T2C data set (Fig. 1a, b). In summary, a much better agreement with the experimental data was found for the loop-cluster model than for the globular domain model.

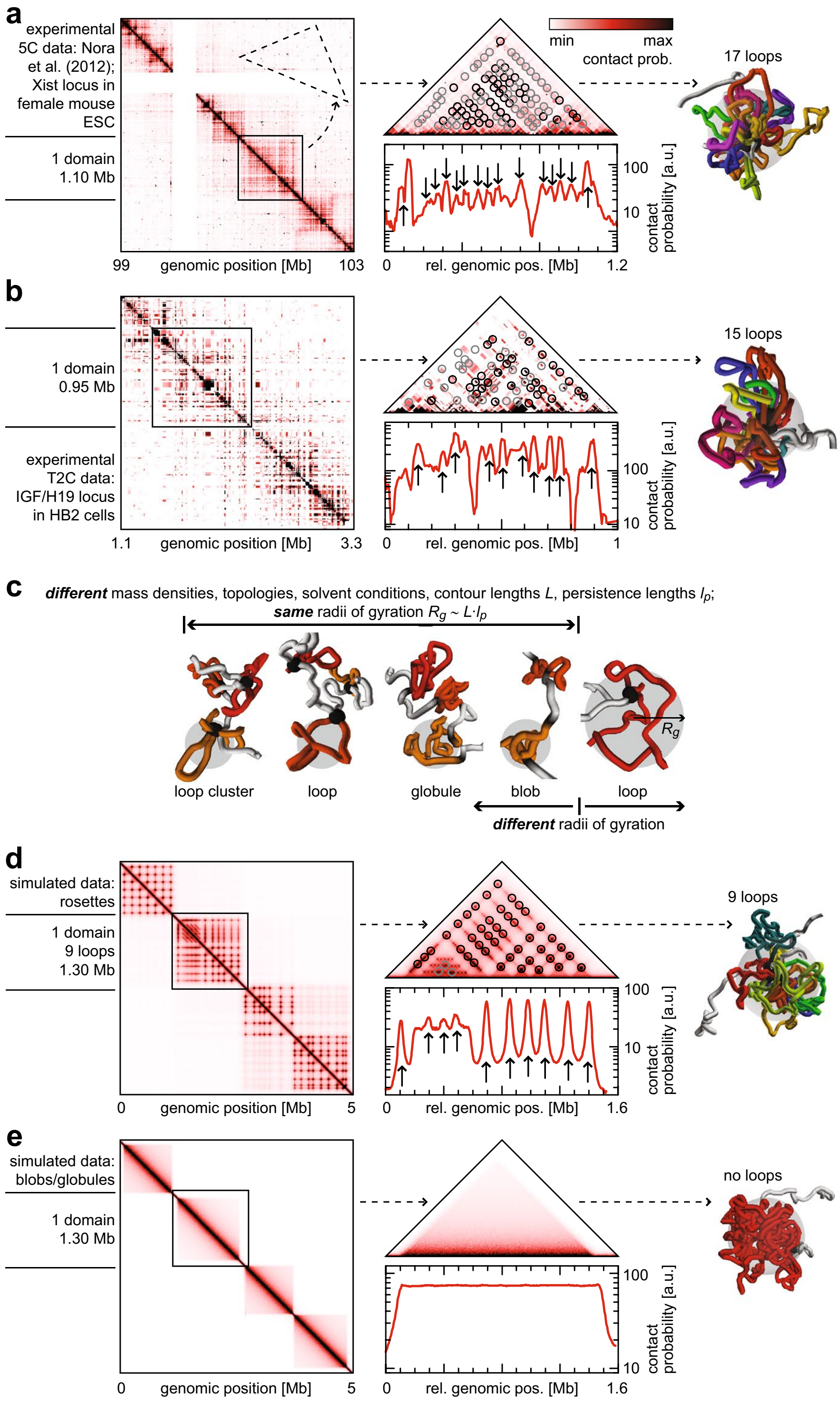
a
experimental 5C data: Nora et al. (2012); Xist locus in female mouse ESC
1 domain
1.10 Mb
99
genomic position [Mb]
103
min
max
contact prob.
100
10
contact probability [a.u.]
0
rel. genomic pos. [Mb]
1.2
17 loops
b
1 domain
0.95 Mb
experimental T2C data: IGF/H19 locus in HB2 cells
1.1
genomic position [Mb]
3.3
100
10
contact probability [a.u.]
0
rel. genomic pos. [Mb]
1
15 loops
c
different mass densities, topologies, solvent conditions, contour lengths L, persistence lengths l_p;
same radii of gyration $R_g \sim L \cdot l_p$
R_g
loop cluster
loop
globule
blob
loop
different radii of gyration
d
simulated data: rosettes
1 domain
9 loops
1.30 Mb
0
genomic position [Mb]
5
100
10
contact probability [a.u.]
0
rel. genomic pos. [Mb]
1.6
9 loops
e
simulated data: blobs/globules
1 domain
1.30 Mb
0
genomic position [Mb]
5
100
10
contact probability [a.u.]
0
rel. genomic pos. [Mb]
1.6
no loops

(See figure on previous page.)

Fig. 1 5C and T2C analysis and polymer modeling. **a** Genomic contact probability matrix for experimental 5C data [11]. The *black square* highlights a domain that is further studied. The *dashed profile* shows how the non-redundant triangular representation was extracted. We could identify loop bases (*circles*) with higher (*black*) or smaller (*gray*) significance. The 1D plot represents the global projection of the highlighted domain. *Arrows* indicate identified loop bases. The extracted loops allowed to simulate and visualize an exemplary configuration and to compute the R_g. **b** Same as **a**, but for experimental T2C data [53]. **c** The different chromatin domain conformations probed in this study to model the FCS data: blob, globule, loop and loop cluster. The radius of gyration R_g(*gray circle*) of domains depends on physical parameters, solvent conditions and the topology of the underlying chromatin fiber. It determines the characteristic time constants of internal relaxation kinetics observed in this study. **d** Same as **a**, but for a model configuration of the loop-cluster conformation under theta-solvent conditions (see Additional file 1: Supplementary Text). **e** Same as **a**, but for a model configuration of the globular conformation

Chromatin fiber dynamics can be evaluated with FCS of transiently bound linker histone

5C and T2C analyses yield structural information from large ensembles of fixed cells. However, the dynamic properties of the observed domains remain elusive. Therefore, we measured chromatin dynamics with FCS using the approach depicted in Fig. 2. The dynamics of linker histone H1-EGFP were determined in the cytoplasm, in less chromatin-dense areas in the nucleus referred to as ‘euchromatin’ and in denser chromatin regions in the nuclear and in the nucleolar periphery referred to as ‘heterochromatin’ in the following [60] (Fig. 2a; Additional file 1: Supplementary Text, Fig. S7 for details on classification). In the cytoplasm, we obtained a fast decay with a characteristic diffusion coefficient of $D \approx 20\ \mu\mathrm{m}^2\ \mathrm{s}^{-1}$ that we assigned to free diffusion of H1.0 (Fig. 2b). Inside the nucleus, the autocorrelation functions (ACFs) decayed bimodally. The first component decayed within 1 ms owing to a freely diffusive fraction. The second, slower decaying contribution was about two magnitudes slower between ~90 and ~160 ms depending on the previously defined nuclear subcompartments used for the measurement. We assigned these slower decays to chromatin-associated movements (Fig. 2c): Distinct relaxation times of chromatin measured by FCS clearly indicated the existence of topologically and dynamically independent chromatin units of a certain scale. The detailed analysis of H1.0 chromatin interactions with FRAP and FCS experiments as well as FCS measurements of H2A and H2B core histones (see below) further corroborated this. Processes that occur at times above 1 s like photobleaching or cellular movements were not detected in FCS due to the short effective measurement time (Additional file 1: Supplementary Text, Fig. S8). Thus, combining FCS measurements with hydrodynamic polymer models should enable us to extract the size of these domains as well as their topologies and physical properties (Fig. 1c).

Both transient chromatin-binding modes of H1.0 are slower than fluctuations seen by FCS

To further rule out that the relaxations in FCS were association–dissociation events, we precisely quantified transient chromatin binding of H1.0 labeled with EGFP with fluorescence recovery after photobleaching (FRAP) experiments. We bleached a strip through the cell nucleus (Fig. 3a) in non-, TSA- and azide-treated cells. The mobility of H1-EGFP was analyzed by fitting the bleach profile (Fig. 3b; Additional file 1: Fig. S11) with Additional file 1: Eq. S91 to follow its broadening as given by its width σ. From linear regressions of σ^2 plotted versus time, apparent diffusion coefficients of $D_{\mathrm{app}} = (10 \pm 5)\cdot 10^{-3}\ \mu\mathrm{m}^2\ \mathrm{s}^{-1}$, $(12 \pm 4)\cdot 10^{-3}\ \mu\mathrm{m}^2\ \mathrm{s}^{-1}$ and $(10 \pm 3)\cdot 10^{-3}\ \mu\mathrm{m}^2\ \mathrm{s}^{-1}$ were derived (non-, TSA- and azide-treated; Fig. 3c). These values were at least two orders of magnitude smaller than those for free H1-EGFP ($D \approx 20\ \mu\mathrm{m}^2\ \mathrm{s}^{-1}$) and at least one order of magnitude larger than the apparent diffusion coefficient of chromatin loci obtained by tracking [35]. Thus, the apparent diffusion process represents coupled diffusion and binding as reported previously [61]. Inspecting the integrated fluorescence intensity in the bleached region over time revealed that the expected intensity change calculated for diffusive redistribution using these D_{app} values differed significantly from the experimentally observed behavior (Fig. 3d; Additional file 1: Fig. S12). Therefore, at least two different binding states must be present, with D_{app} comprising the kinetics of the faster one. Accordingly, the intensity change was fitted with the uncoupled diffusion and binding model given in Additional file 1: Eq. S92. It includes fast free diffusion for which recovery is already complete at the first postbleach time point. The second term covers fast binding and diffusion, while slow dissociation was taken into account separately [62, 63]. This yielded free diffusive fractions of 6 ± 3, 11 ± 4 and 18 ± 12 % and slow dissociation rates of $(8.8 \pm 2.6)\cdot 10^{-3}\ \mathrm{s}^{-1}$, $(13.7 \pm 6.3)\cdot 10^{-3}\ \mathrm{s}^{-1}$ and $(12.2 \pm 2.3)\cdot 10^{-3}\ \mathrm{s}^{-1}$ for non-, TSA-, and azide-treated cells, respectively.

As an independent confirmation of the above results and to extract also the faster dissociation rate, we conducted a continuous photobleaching (CP) analysis (Fig. 3e). The much higher spatial resolution of CP allowed to address local differences in H1-EGFP mobility. Fitting CP curves with Additional file 1: Eq. S93 confirmed the existence of two chromatin-binding states. The analysis yielded fast dissociation rates of

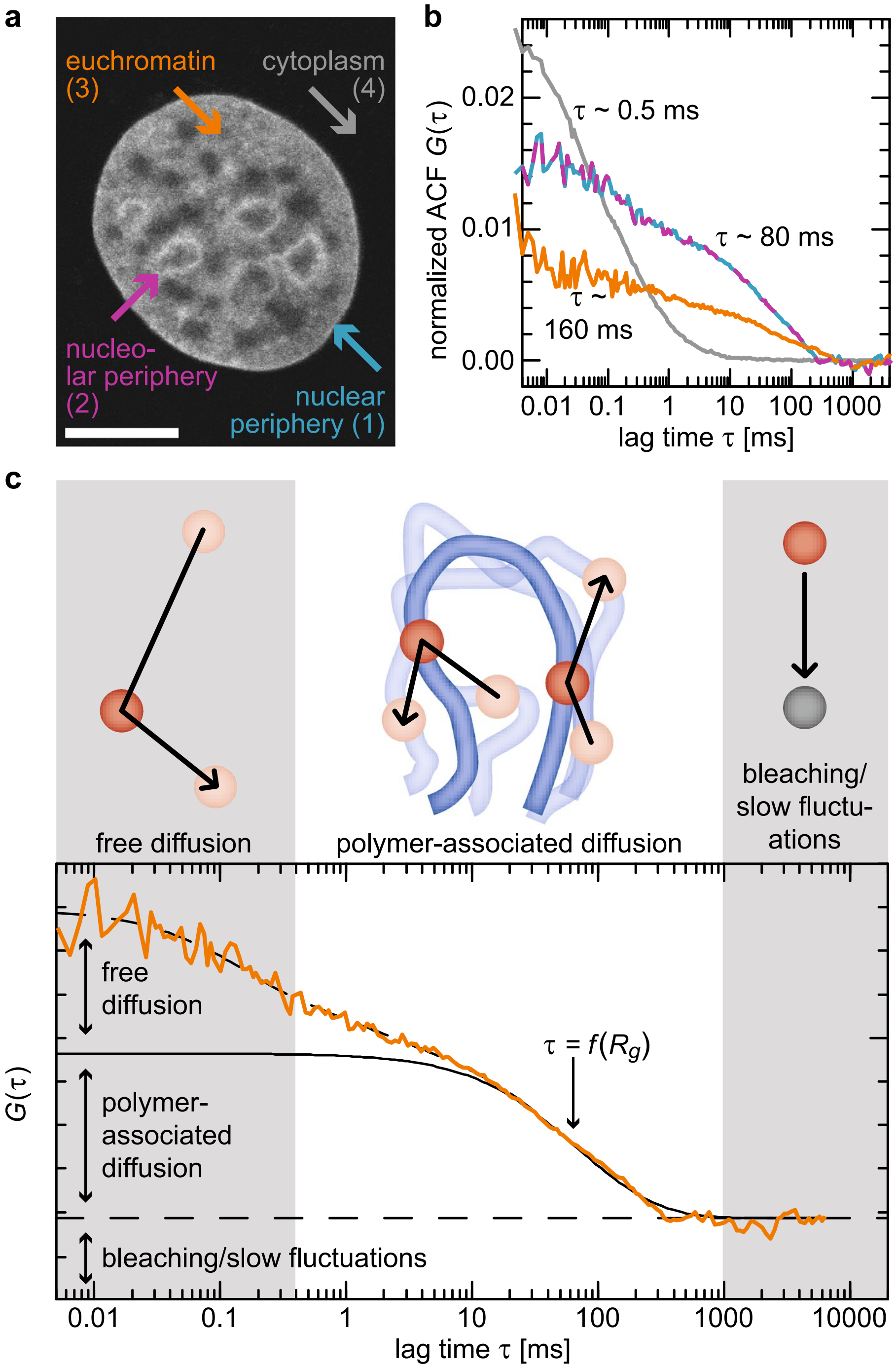

Fig. 2 Observation and interpretation of chromatin dynamics seen with FCS. **a** MCF7 cell stably expressing H1-EGFP with typical localizations for FCS measurements used throughout this study. **b** Typical ACFs obtained at the different locations, showing fast decay due to free diffusion in the cytoplasm and slower decay in the nuclear and nucleolar periphery and even slower decay in euchromatin. **c** Different regimes of the ACFs correspond to different processes: A fast initial decay results from free H1.0 diffusion, followed by a slow decay due to chromatin-associated diffusion or relaxation, whose time constant depends on R_g. Slower processes such as photobleaching do not show up

1.05 ± 0.13 s^{-1} in heterochromatin and 0.76 ± 0.21 s^{-1} in euchromatin of non-treated cells and fractions of 18 ± 2 and 31 ± 9 %, respectively, of the molecules in this association state. Point FRAP (Fig. 3f) confirmed these results by performing series of experiments acquired at single spots in euchromatin with different lengths of the

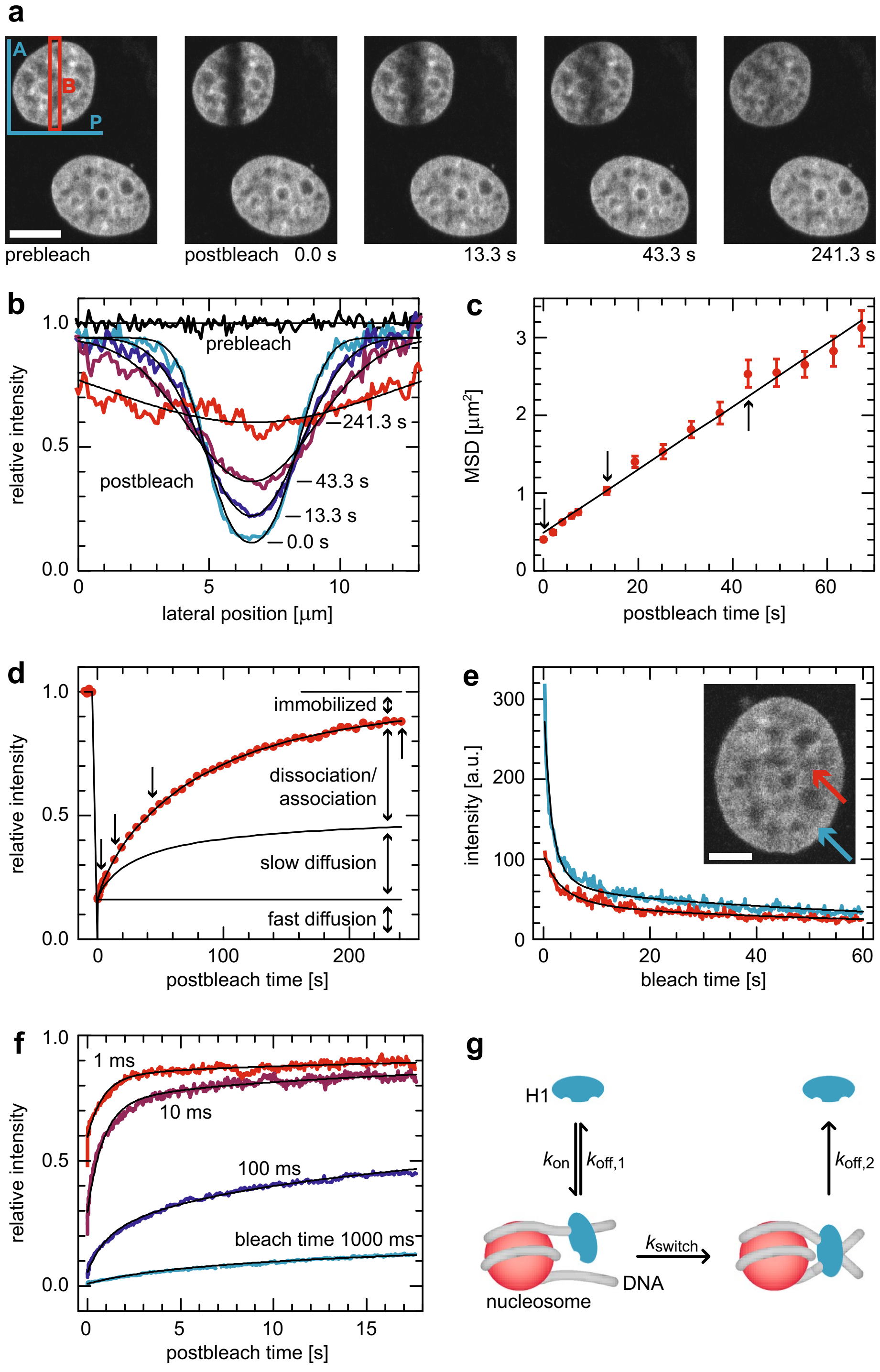
a
A
B
P
prebleach
postbleach 0.0 s
13.3 s
43.3 s
241.3 s
b
relative intensity
1.0
0.5
0.0
prebleach
postbleach
241.3 s
43.3 s
13.3 s
0.0 s
0
5
10
lateral position [μm]
c
MSD [μm²]
3
2
1
0
20
40
60
postbleach time [s]
d
relative intensity
1.0
0.5
0.0
immobilized
dissociation/
association
slow diffusion
fast diffusion
0
100
200
postbleach time [s]
e
intensity [a.u.]
300
200
100
0
0
20
40
60
bleach time [s]
f
relative intensity
1.0
0.5
0.0
1 ms
10 ms
100 ms
bleach time 1000 ms
0
5
10
15
postbleach time [s]
g
H1
k_{on}
$k_{off,1}$
$k_{off,2}$
k_{switch}
nucleosome
DNA

(See figure on previous page.)

Fig. 3 Photobleaching analysis of H1.0-chromatin binding. **a** Imaging FRAP experiment of H1-EGFP expressed in an MCF7 cell. Strip B (*red*) is bleached into the nucleus. The redistribution is followed over time and analyzed in different ways. **b** Averaging along the direction of the long strip dimension A (*blue* in **a**), plotting the profile perpendicularly in direction P and normalizing to the prebleach distribution (Additional file 1: Fig. S11) provided time-dependent profiles. They were fitted with Additional file 1: Eq. S91 to yield the MSD over time. **c** From a linear fit, apparent diffusion coefficients around 10^{-3} μm^2 s^{-1} were extracted. **d** However, the apparent diffusion model, already comprising a fast reaction–diffusion scheme, did not explain exhaustively the intensity time trace obtained by averaging over the bleach region B in **a**. It required additional fast diffusive, transiently binding and immobilized fractions of the molecules for comprehensive modeling of the recovery data. However, a closed expression for a full reaction–diffusion scheme with two immobilization states cannot be derived. **e** We used continuous fluorescence photobleaching (CP), for which a closed expression with two bound states existed and which also allowed to address more specifically the localization types used in this study. This yielded a short-lived (residence time ~1 s) and a long-lived (~2 min) type of immobilization, whose fractions and detailed properties depended on localization and treatment of the cells with ATP or azide. **f** Globally fitting point FRAP experiments featuring bleach times series confirmed the CP and imaging FRAP results. **g** Resulting model of H1.0 binding: molecules bind to the DNA entry–exit sites of nucleosomes with rate k_{on}. Either they rapidly dissociate again with rate $k_{off,1}$, or they engage with rate k_{switch} to the longer-lived conformation, from which they dissociate eventually with rate $k_{off,2}$

bleach segment [43]. The resulting dissociation rates of $(8.2 \pm 3.5)\cdot 10^{-3}$ s^{-1} and 0.83 ± 0.20 s^{-1} for the two binding states were in good agreement with the above findings.

Using this and the previously reported presence of two DNA binding domains in H1 [64], we suggest the following model (Fig. 3g): One binding domain of H1.0 interacts with the entry–exit site of DNA at the nucleosome and either dissociates quickly or engages the second domain to form a longer-lived binding state, from which it dissociates again later. Deriving the rate equations for the different binding states allowed us to calculate the remaining parameters in differently treated cells [65] and in euchromatin and heterochromatin (Additional file 1: Eq. S95; Table 1): The residence time of H1.0 in the short-lived binding state was ~1 s, whereas the average residence time on chromatin was ~4 s. Thus, the fluctuations observed with FCS with relaxation times of ~100 ms did not result from association/dissociation events but rather from chromatin dynamics. Despite our purely intensity-based distinction of euchromatin and heterochromatin, we found a higher effective affinity of H1.0 to heterochromatin as expected [66].

FCS measurements of core histones H2A and H2B confirm chromatin fluctuations with ~100 ms relaxation times

To confirm that the ~100 ms relaxation times indeed represent chain dynamics and not unbinding events or photophysical effects of the fluorescent protein domains, we repeated the measurements in HeLa cells stably expressing histone H2B–mCherry fusions and transiently expressing H2A–EGFP fusions at a ratio of ~5 % to the corresponding endogenous protein [60]. As expected, both the spatial chromatin distribution and the relaxation times were virtually the same for both histones (Fig. 4a). The measured values for nuclear relaxation times were in excellent agreement with H1.0 measurements, which are elucidated in detail in the following section. Fitting the ACFs with model functions for chromatin relaxation based on the comprehensive set of 4 polymer models (Eq. 3) allowed us to quantify the differences between the intranuclear positions studied: In heterochromatin, we obtained 83±7 and 94±6 ms for H2A–EGFP

Table 1 Properties of histone H1.0 binding to chromatin obtained with FRAP and CP

	f_{free} [%]	f_{short} [%]	f_{long} [%]	k_{on} (s^{-1})	$k_{off,1}$ (s^{-1})	k_{switch} [10^{-3}s^{-1}]	$k_{off,2}$ [10^{-3}s^{-1}]
Untreated							
Heterochromatin	6 ± 3	18 ± 2	76 ± 4	3.3 ± 1.7	1.05 ± 0.13	33 ± 12	8 ± 3
Euchromatin	6 ± 3	31 ± 9	63 ± 9	4.0 ± 2.5	0.76 ± 0.21	16 ± 8	8 ± 3
TSA-treated	11 ± 4	89 ± 4		2.1 ± 1.2	0.89 ± 0.22	31 ± 11	12 ± 4
ATP-depleted	18 ± 12	82 ± 12		1.3 ± 1.0	0.89 ± 0.22	27 ± 13	12 ± 2

(mean value ± standard deviation)

f_{free}—free fraction, f_{short}—shortly bound fraction, f_{long}—long-bound fraction, k_{on}—association rate, k_{off}—dissociation rate, k_{switch}—switching rate, TSA—Trichostatin A, ATP—adenosine triphosphate

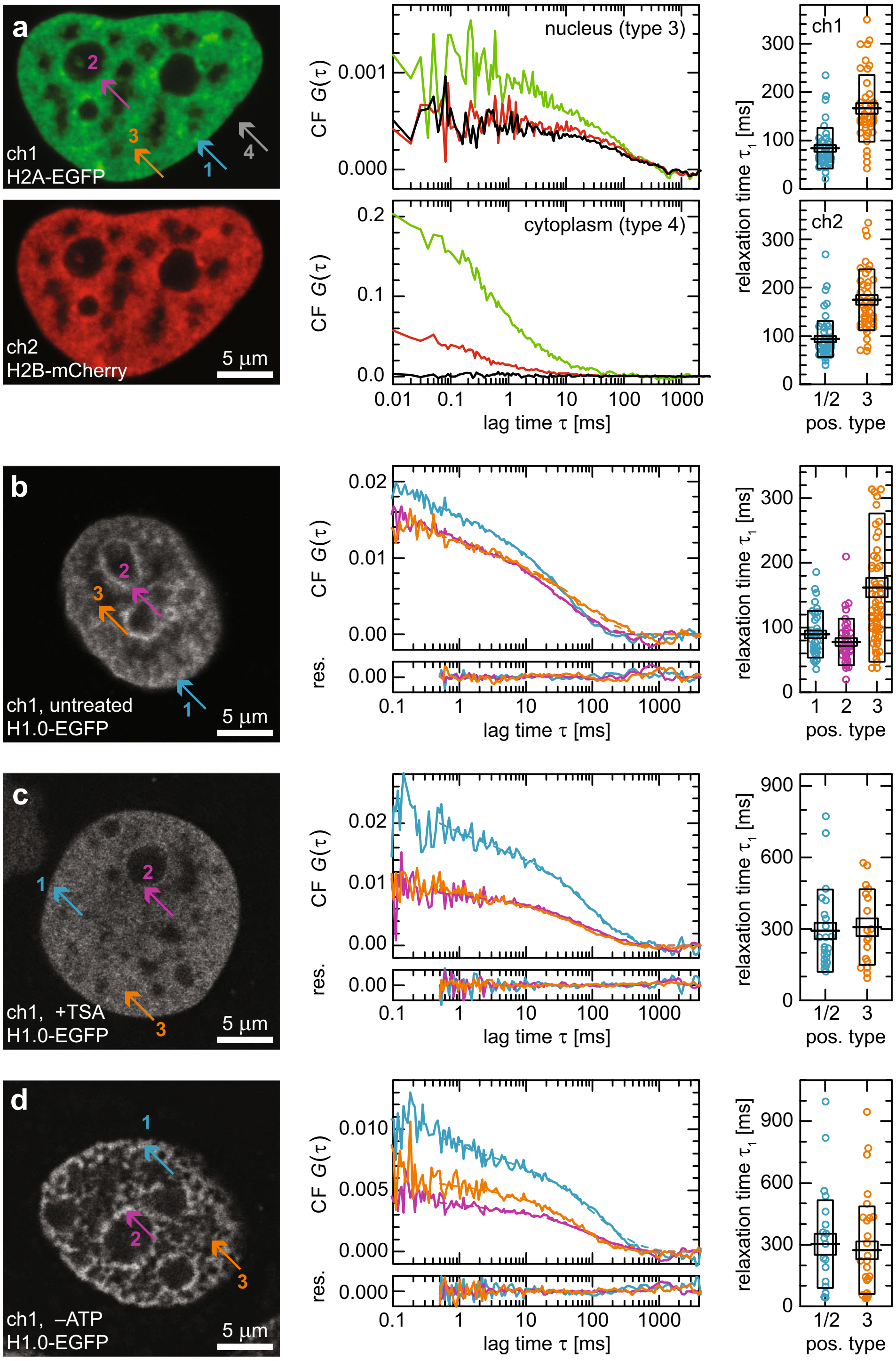

Fig. 4 FCS analysis of chromatin dynamics. **a** HeLa cell expressing H2A–EGFP (transient) and H2B–mCherry (stable). The correlation plots show H2A–EGFP ACFs (*green*), H2B–mCherry ACFs (*red*) and their CCF (*black*) acquired in the nucleus (euchromatin—3) and in the cytoplasm (4), revealing significant cross-correlation in the nucleus, but not in the cytoplasm. Fitting them with a relaxation model for loop-rosette-structured polymers under theta-solvent conditions yielded a significant difference in relaxation time distribution between hetero-(1/2) and euchromatin (3) both for H2A (ch1) and H2B (ch2). **b** Untreated MCF7 cell expressing H1-EGFP. At the three positions (nuclear periphery—1, *blue*; nucleolar periphery—2, *purple*; euchromatin—3, *orange*), the corresponding ACFs were acquired. Fitting them like in **a** (res—residuals) yielded a significant difference in relaxation time distribution between hetero- (1, 2) and euchromatin (3). **c** Same as **b**, but cells were treated with TSA, resulting in globally increased relaxation times without significant differences between 1, 2 and 3. **d** Same as **b**, but cells were ATP-depleted, resulting in globally increased relaxation times without significant differences between 1, 2 and 3

and H2B–mCherry, respectively, as first-order mode relaxation time under theta-solvent conditions (see next section for details and Table 2 for good-solvent and globular conditions). Corresponding values in euchromatin were approximately twofold slower with 165±11 and 174±10 ms, respectively, in contrast to the expectation that in lower density regions, relaxations would be faster. Importantly, the fluctuations showed a pronounced cross-correlation due to the co-diffusion of H2A and H2B simultaneously integrated into nucleosomes and chromatin. In contrast, there was no cross-correlation in the cytoplasm as expected. These observations corroborate our conclusion that chromatin dynamics are the source of the observed fluctuations. It can be ruled out that they are due to blinking of fluorescent protein domains because this would not result in a cross-correlated signal. Furthermore, the cross-correlation cannot result from spectral cross-talk because this would yield high cross-correlation in the cytoplasm, too.

Polymer relaxation modes seen by autocorrelation analysis reflect persistence length, mass density and topology of chromatin domains

To decompose the autocorrelation analysis into parameters that describe features of polymer domains, the Rouse–Zimm model was applied for a quantitative characterization of domain dynamics [52]. Independent relaxation modes represent distinct characteristic times τ_p and amplitudes $a_p = \langle \mathbf{X}_p^2 \rangle$ that are observable in the FCS experiments. These parameters depend on topology, solvent conditions, viscosity η_s, temperature T, Boltzmann constant k_B and radius of gyration R_g (see Additional file 1: Supplementary Text for more details):

$$
\begin{aligned}
&\tau_1 \approx 6.111\frac{\eta_s R_g^3}{k_B T}, \quad \tau_p = \frac{\tau_1}{p^{3/2}}, \quad a_p \approx 0.152\frac{R_g^2}{p^2}, && \begin{array}{r}\text{loop-rosette conformation,}\\ \text{theta-solvent conditions,}\end{array}\\
&\tau_1 \approx 4.114\frac{\eta_s R_g^3}{k_B T}, \quad \tau_p = \frac{\tau_1}{p^{17/20}}, \quad a_p \approx 0.172\frac{R_g^2}{p^{9/4}}, && \begin{array}{r}\text{loop-rosette conformation,}\\ \text{good-solvent conditions,}\end{array}\\
&\tau_1 \approx 7.151\frac{\eta_s R_g^3}{k_B T}, \quad \tau_p = \frac{\tau_1}{p}, \quad a_p \approx 0.236\frac{R_g^2}{p^{5/3}}, && \text{globular conformation,}\\
&\tau_1 \approx 5.849\frac{\eta_s R_g^3}{k_B T}, \quad \tau_p = \frac{\tau_1}{p^{3/2}}, \quad a_p \approx 0.152\frac{R_g^2}{p^2}, && \begin{array}{r}\text{blob/linear conformation;}\\ \text{mode number } p = 1, 2, 3, \ldots\end{array}
\end{aligned}
\tag{2}
$$

Table 2 Dynamic and structural parameters of histone-FP-labeled chromatin domains obtained with FCS at different nuclear localizations

		n	**Loop-rosette, blob; theta-solvent conditions**[a]			**Loop-rosette; good-solvent conditions**[b]			**Globular**[b]	
			τ_1 (ms)	R_g (nm)	*gc* (Mb)	τ_1 (ms)	R_g (nm)	*gc* (Mb)	R_g (nm)	*gc* (Mb)
H1-EGFP untreated	Perinuclear	35	91 ± 6	245 ± 5	0.80–1.12	100 ± 6	289 ± 6	1.31–1.83	240 ± 5	0.75–1.05
	Perinucleolar	34	78 ± 6	234 ± 6	0.70–0.98	94 ± 5	283 ± 5	1.23–1.73	235 ± 4	0.71–0.99
	Euchromatin	62	161 ± 15	297 ± 9	0.83–1.16	191 ± 20	359 ± 12	1.47–2.05	298 ± 10	0.84–1.17
H2A-EGFP untreated	Perinucle(ol)ar	84	83 ± 7	238 ± 4	0.73–1.03	90 ± 8	279 ± 4	1.18–1.65	232 ± 4	0.68–0.95
	Euchromatin	84	165 ± 11	299 ± 9	0.85–1.19	188 ± 14	356 ± 13	1.43–2.00	297 ± 11	0.83–1.16
H2B-mCherry untreated	Perinucle(ol)ar	84	94 ± 6	249 ± 4	0.84–1.18	102 ± 7	291 ± 4	1.34–1.88	242 ± 3	0.77–1.08
	Euchromatin	84	174 ± 10	304 ± 9	0.89–1.25	195 ± 12	361 ± 12	1.49–2.09	300 ± 10	0.86–1.12
H1-EGFP TSA-treated	Perinucle(ol)ar	25	292 ± 34	362 ± 14	1.65–2.31	366 ± 49	445 ± 20	3.07–4.30	370 ± 17	1.77–2.47
	Nucleoplasm	18	307 ± 37	368 ± 15	1.74–2.43	384 ± 51	453 ± 20	3.24–4.54	377 ± 17	1.87–2.61
H1-EGFP ATP-depleted	Perinucle(ol)ar	17	303 ± 51	367 ± 21	1.72–2.41	388 ± 74	454 ± 29	3.26–4.57	378 ± 24	1.88–2.64
	Nucleoplasm	25	278 ± 43	356 ± 18	1.57–2.20	351 ± 59	439 ± 25	2.95–4.13	365 ± 21	1.69–2.37

(mean value ± standard error; min. value–max. value)

τ_1—decay time of the first polymer relaxation mode, R_g—radius of gyration of topologically and dynamically independent chromatin domain, *gc*—genomic content of topologically and dynamically independent chromatin domain

[a] Relaxation times and radii of gyration are numerically identical for loop-rosette conformation under theta-solvent conditions and for blob conformation

[b] Relaxation times are numerically identical for loop-rosette conformation under good-solvent conditions and for globular conformation

These relaxations result in local concentration fluctuations of segments even when the center-of-mass translocation is negligible. An obvious way to study such fluctuations is their evaluation by autocorrelation analysis as conducted for FCS measurements. Relaxation modes are independent of each other and have exponentially decaying position correlation functions [52]. Thus, each mode is represented by a diffusion process in a harmonic potential, which is an Ornstein–Uhlenbeck process, the simplest example of a stationary Markovian process with Gaussian probability distribution at all times [67]. To this theoretical framework, the FCS formalism was applied [68, 69] (Additional file 1: Supplementary Text), yielding the autocorrelation function

$$G(\tau) \propto a_{\mathrm{p}} \left[\left(1 + \frac{1 - \exp\left[-\tau/\tau_{\mathrm{p}}\right]}{\upsilon}\right)^{-1} \left(1 + \frac{1 - \exp\left[-\tau/\tau_{\mathrm{p}}\right]}{\kappa^2 \upsilon}\right)^{-1/2} - \left(1 + \frac{1}{\upsilon}\right)^{-1} \left(1 + \frac{1}{\kappa^2 \upsilon}\right)^{-1/2} \right]. \quad (3)$$

Here, $\upsilon = \tau_D / \tau_p$ is the ratio of diffusion correlation and relaxation time and $\kappa = z_0 / w_0$ the structure parameter (Methods). Polymer relaxation was thus modeled by summing over $p = 1, 2, 3, \ldots$ of Eq. 3. The relaxation time τ_1 from a fit of the model function to experimental data yielded the radii of gyration according to Eq. 2 with the nuclear solvent viscosity determined independently (Additional file 1: Supplementary Text). For known genomic content, a well-defined relationship between chromatin persistence length, mass density and domain topology such as the number of loops in a cluster/rosette can be established. Thus, the formalism links structural domain parameters from 3C-derived methods with dynamic features measured by FCS.

FCS measurements of chromatin dynamics reveal different states of domain organization in hetero- and euchromatin

Fitting the ACFs with the polymer models (Eq. 1–3) allowed us to quantitatively determine chromatin relaxations times and other polymer parameters at different intranuclear positions and conditions (Fig. 4b; Table 2): In heterochromatin, e.g., at the nuclear or the nucleolar periphery, we obtained 90 ± 6 and 78 ± 6 ms, respectively, as first-order mode relaxation time under theta-solvent conditions. In the rest of the nucleus, in euchromatin, we measured 161 ± 15 ms, i.e., approximately twofold bigger values. Independent of the actual topological conformation, this can only be explained with a weaker local confinement of euchromatin due to a lesser degree of domain compaction because a purely chromatin density-driven relaxation would be faster in euchromatin compared to heterochromatin. In other words, comparing the relaxation with the oscillation of a bead on a string, the oscillation time is longer for a weaker string. Thus, the more open and less compact euchromatin can be compared to a weaker, more open string and the more compact heterochromatin to a stronger, more compact one.

After treatment of the cells with TSA, chromatin became hyperacetylated and adopted a decondensed state of the chromatin fiber [70, 71]. This process resulted in a homogeneous nuclear morphology and chromatin density distribution (Fig. 4c). The differences in chromatin relaxation at different nuclear loci vanished. The relaxations slowed down to time constants of 292 ± 34 ms at peripheral and 307 ± 37 ms at central nuclear positions (under theta-solvent conditions; Fig. 4c; see Table 2 for a summary of the different conformations). These values were even higher than those measured for euchromatin of untreated cells and indicated a further reduction in local confinement and an increased genomic content of domains.

The dynamics changed numerically similarly upon ATP depletion after treatment of the cells with azide. Here, however, the chromatin distribution became more aggregated with a less homogeneous morphology (Fig. 4d). The differences in chromatin relaxation vanished and the relaxations slowed down, resulting in time constants of 303 ± 51 ms in peripheral and 278 ± 43 ms in central positions (theta-solvent conditions, Fig. 4d; see Table 2 for a summary of the different conformations). This and the structural differences as seen in the images argue for increased sizes of domains due to agglutination effects. Interestingly, fundamentally different processes—decondensation and aggregation—result in the same effect of effective growth of independent domains. However, in the former case, the domains are distributed more and in the latter case less homogeneously than in untreated cells.

FCS measurements of chromatin dynamics identify 1-Mb-sized dynamic domains

From the observed relaxation times, the radii of gyration of dynamic domains could be extracted according to Eq. 2 for loop-cluster topologies under theta-solvent conditions, for the same under good-solvent conditions, for globular conformations and for blobs. For untreated cells, this resulted for heterochromatin in 240 ± 6 nm and for euchromatin in 297 ± 9 nm (theta-solvent conditions, Fig. 5a; see Table 2 for a summary of the different conformations). Next, from fluorescence images we extracted chromatin densities in euchromatin of 91 ± 1 % and in heterochromatin of 156 ± 5 % of the mean nucleosome

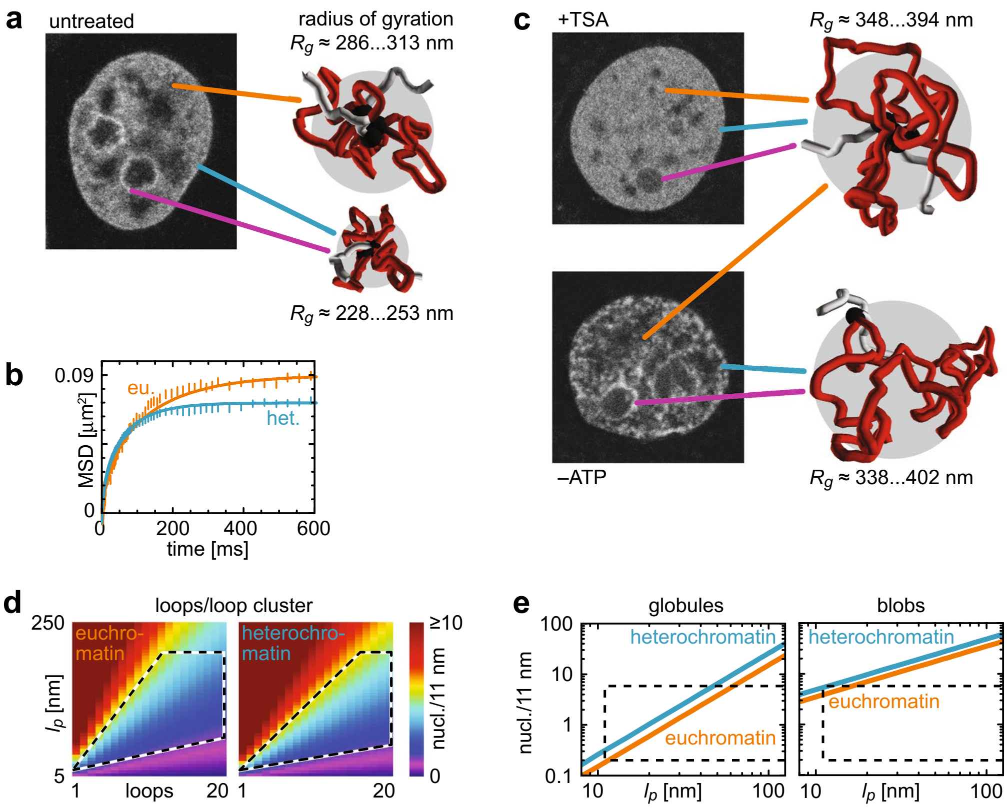

Fig. 5 Physical properties and dynamics of domain structure. **a** Radii of gyration for the three different localization classes as extracted from the FCS data in Fig. 4 for untreated cells. The given range covers the results from the blob and the loop-cluster conformation under theta-solvent conditions and from the globular conformation and reveals differences in local domain size between euchromatin and heterochromatin. **b** MSD plots for typical chromatin segments in hetero- (het) and euchromatin (eu) calculated (*straight lines*) using the loop-rosette model under theta-solvent conditions and the radii of gyration from **a** and extracted from typical FCS measurements (*symbols*), showing confined diffusion on the 100 ms and 100 nm time and length scale. **c** Same as **a** for TSA-treated and ATP-depleted cells, respectively, showing that the domain size increased to similar values upon perturbation of chromatin structure. **d** Chromatin mass density versus the number of loops per domain and the fiber persistence length calculated for the loop-cluster conformation under theta-solvent conditions. Highlighted areas represent the parameter subspace in agreement with previous studies. **e** Same as **d**, but for the globular and the blob conformation and thus without dependence on loop number

concentration of 100–140 µM [60, 72, 73] (Additional file 1: Supplementary Text, Fig. S7). In combination with a nucleosomal repeat length of 191 bp [72, 74], this enabled us to transform the domain volume determined from the radius of gyration into genomic content (Additional file 1: Eq. S10): We obtained 700–1120 and 830–1160 kb for hetero- and euchromatin, respectively, for blobs and loop clusters under theta-solvent conditions, 1230–1830 and 1470–2050 kb for loop clusters under good-solvent conditions, and 710–1050 and 840–1170 kb for globules.

For the good-solvent loop-cluster topology, the genomic content of domains was significantly larger than the previously observed 500–1000 kb for subchromosomal domains/TADs [11, 14], i.e., the assumption of good-solvent conditions would lead to a pronounced overestimation of domain size. Accordingly, the loop-cluster conformation under theta-solvent conditions was considered for further analysis. For this description, only minor excluded volume effects are present and thus a high structural flexibility on the level of the chain of nucleosomes. The blob and the globular polymer conformation would fit the TAD genome content but not the experimental interaction data from the 5C and T2C analysis as discussed above.

The polymer models predict a confined movement of chromatin segments relative to the center of mass of a domain, which is stationary on the time scale under consideration. Using the relaxation times obtained for the theta-solvent model, we calculated the MSD curves of a genomic site in euchromatin and heterochromatin (Fig. 5b), which clearly showed confinement of translocations and agreed well with experimental ones extracted directly from ACFs of exemplary measurements in euchromatin and heterochromatin according to Additional file 1: Eq. S83. Furthermore, the calculated MSDs corresponded well with previous studies of chromatin translocations [38–40, 72] and thus confirm our approach.

Hyperacetylation and ATP depletion differentially affect chromatin dynamics and alter the radius of gyration of domains

Chromatin hyperacetylation due to TSA treatment of the cells slowed down chromatin relaxation, as apparent from a similarly increased radius of gyration at peripheral ($R_g = 362 \pm 14$ nm) and central nuclear positions ($R_g = 368 \pm 15$ nm) under theta-solvent conditions (Fig. 5c; Table 2). With a homogeneous nucleosome concentration of 100–140 µM, the genomic size of dynamic domains was 1650–2610 kb (Table 2), i.e., twofold larger than in untreated cells. This corroborates the view that hyperacetylation induces a larger-scale rearrangement of chromatin toward a more uniform conformation [70, 71] and the notion of discriminable compact and passive domains [56] whose differences vanish upon TSA treatment.

For ATP-depleted cells, radii of gyration increased to 367 ± 21 nm at peripheral and 356 ± 18 nm at central nuclear positions (Fig. 5c; Table 2). We obtained 2680–4100 and 1430–2160 kb for peripheral and central positions, respectively, when using the same mean nucleosome concentrations as for untreated cells. This suggests that in contrast to hyperacetylation, ATP depletion affects euchromatin and heterochromatin differentially as reflected by the increased heterogeneity in the images possibly due to agglutination of domains and increased packing density of nucleosomes.

Local compaction of chromatin is determined by its flexibility, mass density and topology

To characterize the organization of the chromatin fiber into domains, a set of structural and physical parameters is required: the persistence length, the mass density and, in the case of looping, the number of loops per domain. We found that only certain combinations of the properties comply with the observed radius of gyration and genomic content. Figure 5d shows the relationship of number of loops per domain, chromatin persistence length and linear mass density computed for hetero- and euchromatin for loop clusters under theta-solvent conditions using Eq. 1 and a nucleosomal repeat length of 191 bp [72, 74]. The encircled area covers the parameter range compatible with previous knowledge [27, 74–77], i.e., a mass density of 0.5–6 nucleosomes/11 nm, a persistence length of 10–200 nm and up to 20 loops. A possible chromatin conformation with 9 loops per domain has a mass density of 4.5 nucleosomes/11 nm and a persistence length of 110 nm for euchromatin and 5.5 nucleosomes/11 nm and 100 nm for heterochromatin in very good agreement with Knoch et al. [53]. For a globular domain structure, the relation of persistence length and linear mass density computed for hetero- and euchromatin is depicted in Fig. 5e. Again, the marked area highlights the accessible part of parameter space and reveals a range of possible combinations, e.g., a mass density of 4.5 nucleosomes/11 nm and a persistence length of 55 nm for euchromatin and 5.5 nucleosomes/11 nm and 45 nm for heterochromatin. For both examples, the heterochromatin fiber would be more compacted but also locally more flexible. In contrast, for a blob-like domain structure, the relation of persistence length and mass density (Fig. 5e) does not overlap with previously obtained values, i.e., a purely generically formed chain-of-blob topology does not provide enough topological compaction. Thus, only the globule and the loop-cluster model agree with our observations for domain size and genomic content and only the latter with the 5C and T2C data.

Comparison of Fig. 5d with Fig. 1a, b showed that the large number of loops found for the ~1-Mb domains matched well with a persistence length of ~ 100 nm when assuming a mass density of ~4 nucleosomes/11 nm. Thus, FCS dynamics measurements allowed to detect dynamically independent subchromosomal domains, whereas 5C and T2C data allowed to detect topologically independent domains, and identifying them with each other enabled us to extract their size, genomic content, topology and average physical properties of the underlying chromatin fiber.

Local chromatin dynamics determine genome accessibility

From the initial linear increase in the MSD (Fig. 5b), an apparent diffusion coefficient of ~0.1 $\mu m^2 s^{-1}$ of chromatin segments could be extracted with a segment concentration of 10^4–10^5 μm^{-3} (Fig. 5d, e). From these parameters, a frequency of collisions with other sites could be estimated for a given genomic site inside a topological domain [78]: Intradomain collisions occur at a rates of ~100 collisions/s, whereas interdomain collisions are at least 100-fold less frequent. Therefore, contacts between genomic sites showing up in 3C-derived methods must be physically stable and long-lived enough to not be disrupted by the rapid local movements of the chromatin fiber, rendering stable looping a highly probable mechanism of domain formation.

The confined diffusion of chromatin segments (Fig. 5b) translates into pronounced volume fluctuations of the domains on the time scale of the observed relaxation times. The volume fluctuations are of the same order of magnitude as the volume itself, i.e., in the order of

0.1 µm^3 (Additional file 1: Eq. S9). The time it takes soluble factors to cross a volume of the size of the domains by diffusion is around a few ms and much shorter than the relaxation time on the 100 ms time scale. Thus, the short-term accessibility of the domains for a single molecule is given by the statically occupied volume (Fig. 6). Many lacunae and corrals in the chromatin environment [42, 79] are devoid of scarce factors, so that locally, their effective concentration can be significantly smaller than the mean. For abundant molecules or complexes, however, it is defined by the fluctuation-induced maximum accessible volume. Thus, domains are adiabatically replenished to the mean concentration with molecules or complexes except for the net chromatin volume. Therefore, diffusion-limited reactions such as transcription factor binding to DNA are expected to display a more than linear dependence on factor concentration, in contrast to the case of soluble binding partners [78].

We calculated the accessible volume fraction according to Additional file 1: Eq. S74, S75 for euchromatin and heterochromatin as well as for TSA-treated cells, assuming both static and fluctuating domain sizes (Fig. 6). The accessibility limit, i.e., the molecular radius, for which accessibility was reduced to 50 %, was approximately twofold larger for dynamic domains than for static ones. Assuming an effective chromatin fiber diameter of 14 nm and a mass density of 1.6 nucleosomes/11 nm, the limit was 5 and 10 nm for heterochromatin, 10 and 20 nm for

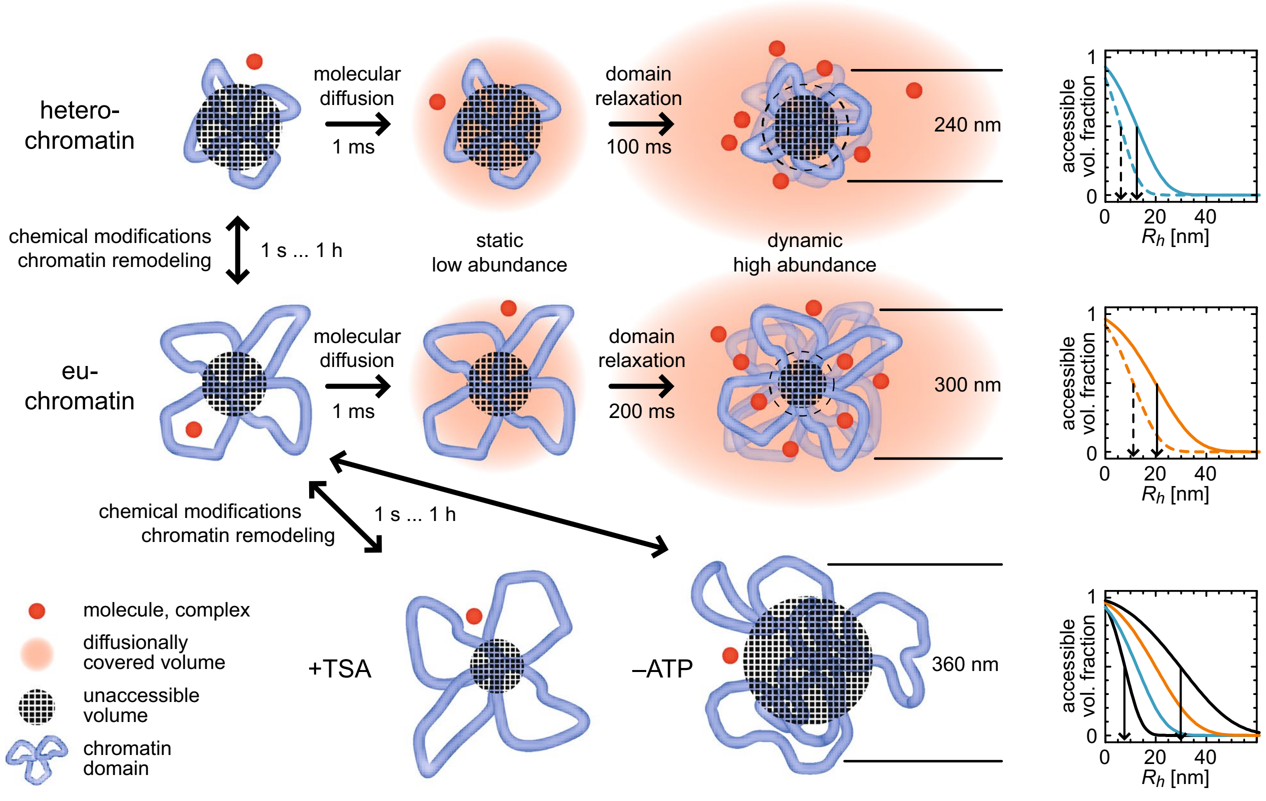

Fig. 6 Static and dynamic chromatin domain accessibility. Model for domain accessibility of heterochromatin, euchromatin, TSA-treated and ATP-depleted chromatin. A certain volume fraction of the domain (*blue*) is not accessible (*checkered*) for soluble factors (*red*) due to steric hindrance. The domain is virtually static on time scales long enough for a single molecule to roam the domain volume by diffusion (~1 ms; *light red*), resulting in an unaccessible volume significantly larger than the net fiber volume. The single molecule is highly unlikely to return to a previously visited domain so that it only senses the static, snapshot-like unaccessible volume. Thus, accessibility for low-abundance molecules is defined by the apparently static conformation during the ms passage time. This effect is more pronounced for compact heterochromatin than for open euchromatin. On the time scale of domain reorganization (~100–200 ms), molecules can search different domain areas such that the effectively unaccessible volume decreases toward the net fiber volume (including 'classical' excluded volume effects). Accordingly, high-abundance molecules effectively sense a significantly higher accessible volume, i.e., accessibility depends on molecular concentration in addition to a binding reaction itself. Moreover, it is determined by the size of the molecule or complex (*arrows* in 1D plots), confirming previous findings on static chromatin accessibility. Thus, formation of domains consisting of dynamic loops provides an additional degree of freedom to differentially regulate chromatin accessibility. Chemical modifications and chromatin remodeling processes take place on significantly longer time scales so that access for required molecules can be regulated by domain and loop dynamics

euchromatin, and 15 and 30 nm for TSA-treated cells for low- and high-abundance particles, respectively. This agreed well with previous results on chromatin accessibility [42, 71, 80] and showed that the fluctuations of the domains provide differential genome access in nonlinear dependence on particle size and concentration.

Discussion

The results presented here provide a missing link between chromatin organization maps that reveal the subchromosomal domain structure at steady state from 3C-type analyses and the dynamic properties of these compartments measured here by FCS. The 3C-derived methods such as 5C, Hi-C or T2C as well as light microscopy measurements by fluorescence in situ hybridization/FISH [1, 7, 11, 14, 29, 81] yield more or less direct information about the relation between genomic and spatial distance in steady state. These have been used to evaluate physical models of three-dimensional chromatin organization [5, 29, 75–77, 82–85]. By applying a simple peak detection algorithm to exemplary experimental 5C and T2C data, the presence of loops and loop clusters is apparent, corroborating previous models and findings. From our analysis, we conclude that the highly dynamic nature of domains observed in our study provides an additional constraint on three-dimensional modeling of chromatin structure for 3C-type data: A high contact probability can only result from sufficiently stable physical contact between two loci, otherwise the pronounced fluctuations would effectively segregate them. We estimate that the lifetime of chromatin interactions must exceed a few seconds, i.e., significantly longer than the observed relaxation time, to be detected by chromosome conformation capture techniques. Moreover, the frequently occurring intradomain collisions of genomic sites are not rate limiting for contact formation between them. So far, one could only conclude that the interactions persisted for a significant fraction of the cross-linking incubation time of a few minutes [86, 87]. To our knowledge, this aspect has not been considered previously for the interpretation of 3C-like data.

Chromatin dynamics have been studied mostly by time-lapse microscopy and tracking or bleaching of spatially defined loci [35, 36, 40, 41]. While the time dependence of the MSD derived in these experiments provides evidence for the existence of distinct topological domains, it is difficult to draw quantitative conclusions on the underlying chromatin structure, especially on the time scale below one second. On the other hand, with our FCS-based methods we detected characteristic chromatin domain relaxation times in the order of 100 ms from measurements of the nuclear H1-EGFP signal (as well as of chromatin-incorporated core histones H2A and H2B). Furthermore, we developed an analytical Rouse–Zimm-based model that allows to derive polymer features from these data. Different conformations with topologies ranging from generically formed blobs via crumpled or fractal globules to loop-cluster/rosette formations can be represented to derive corresponding physical properties like persistence length and fiber density. In conjunction with the 5C/T2C analyses, we conclude that the dynamics of topological domains are best described by a clustered loop model in a theta solvent with radii of gyration of the domains of ~300 nm in euchromatin and ~240 nm in heterochromatin and a genomic content of ~0.8–1.2 Mb in the unperturbed state. We suggest to assign these domains to previously reported subchromosomal domains [15, 16] or TADs [11, 14], which have emerged as general pattern for chromatin organization in vertebrates [1, 3] and have been further confirmed by recent low-noise high-resolution T2C data [53]. They feature a typical size of ~1 Mb. Our data are in excellent agreement with previous studies that tracked chromatin foci [38–40, 72] and with persistence lengths and mass densities inferred from other studies [5, 27, 74–77]. We conclude that our observations are an independent and methodologically complementary quantitative evidence for dynamically and topologically independent domains that define both structural and dynamic properties of chromatin on the 1 Mb scale. In TSA-treated cells, euchromatin and heterochromatin become indistinguishable and both domain volume and genomic content increase, indicating a significant rearrangement of domains possibly owing to alternative remodeling following transcription and replication. In ATP-depleted cells, however, chromatin becomes more aggregated and both domain volume and genomic content increase, here possibly due to arrested transcription and chromatin remodeling.

Physical interactions between genomic loci via chromatin loops are important for the repression and activation of genes in the three-dimensional nuclear environment [4, 21, 23]. While the stability of loops is crucial for the robustness of gene expression patterns, plasticity and potential of domains for reorganization are key for gene up- or down-regulation in response to cellular stimuli [24, 35]. The highly dynamic nature of chromatin on the size scale of up to 1 Mb observed here with a typical locus spatially fluctuating by ~100 nm within ~100 ms facilitates fast rearrangement of three-dimensional topologies. In addition, as depicted in Fig. 6, it increases the effective chromatin accessibility, in good quantitative agreement with previous results: More compact heterochromatic domains have a larger unaccessible volume fraction than more open euchromatic ones. This effect additionally depends on the size of the molecules or complexes trying to access the genome [42, 71, 88]. Molecular diffusion is fast enough to roam a complete domain within few milliseconds, during which the domain itself appears static. Relaxation of domains in the 100 ms range affects genome access in a nonlinear protein concentration-dependent manner: Highly abundant molecules at several 100 nM concentrations 'fill' the fluctuating domain so that a larger volume fraction than for a static TAD becomes adiabatically accessible. In contrast, for low-abundance molecules encounters with specific loci within a domain are not only diffusion limited, but further impeded by transient occlusion of binding sites. They sense a higher inaccessible volume fraction. As a result, domain dynamics introduce an additional factor for nuclear target search. The concentration-dependent differential accessibility of this process leads to largely different search times as compared to a static chromatin network. Furthermore, it allows of locus-specific variations as relaxation times between heterochromatin and euchromatin are different and additionally dependent on reversible chromatin modifications like the TSA-induced hyperacetylation. Thus, by integrating the structural features of chromatin domains with their dynamic properties we reveal an additional regulatory layer for target search processes in the nucleus that may contribute to establishing cell-type-specific gene expression programs.

Conclusions

In this study, we present a missing link between chromatin organization maps that reveal the subchromosomal domain structure at steady state from 3C-type analyses and the dynamic properties of these compartments measured here by FCS. Both 5C/T2C and FCS results suggest that chromatin is organized into topologically and dynamically independent domains of ~300 nm radius in euchromatin and ~240 nm in heterochromatin and a genomic content of ~0.8–1.2 Mb, confirming numerous previous results. Loops/loop clusters as domain-forming features are required to match the measured level of compaction and the observed features of 5C/T2C data. In addition to the structural aspects, the dynamics of domains in different epigenetic states propose that the regulation of chromatin accessibility for soluble factors displays a significantly stronger dependence on factor concentration than search processes within a static network.

Methods

Cell culture

The plasmid vector with the autofluorescent histone H1.0-GFP was constructed as described [89]. The human histone gene for H1.0 (Gene bank M87841) was amplified by PCR and inserted into the SalI–BamHI site of the promoterless plasmid pECFP-1 (Clontech, Mountain View, CA, USA). The HindIII fragment of simian virus 40 (SV40) was inserted in reverse direction into the HindIII site of the multiple cloning site of pECFP-1, and the ECFP sequence was replaced with EGFP. The resulting construct pSV-HIII-H1.0-EGFP expresses a 440-amino-acid fusion protein from the early SV40 promoter and consists of the human H1.0 gene, a 7-amino-acid linker and the C-terminal EGFP domain. This plasmid was introduced into MCF7 cells with Lipofectamin (Life Technologies, Carlsbad, CA, USA), and a stable monoclonal cell line was selected with 500 µg/ml G418 (Life Technologies). H1.0-expressing cells as well as non-transfected MCF7 cells were grown in RPMI 1640 (Life Technologies) supplemented with 10 % FCS in a humidified atmosphere under 5 % CO_2 at 37 °C. HeLa cells expressing H2B–mCherry stably and H2A–EGFP transiently were made as described elsewhere [90].

For microscopy, cells were allowed to attach for at least 24 h in Nunc LabTek chambered coverglasses (Nalge Nunc, Rochester, NY, USA) or in MatTek glass-bottom dishes (MatTek, Ashland, MA, USA) before the experiments. For TSA treatment, cells were allowed to attach for at least 24 h in chambered coverglasses and then incubated with 100 ng/ml TSA (Sigma-Aldrich, St. Louis, MO, USA) for 15–20 h before the experiments. For Na-azide treatment, cells were allowed to attach for at least 24 h in chambered coverglasses and then incubated with 10 mM Na-azide for 20 min. Experiments were then performed within 40 min.

Fluorescence microscopy

Confocal fluorescence microscopy images, FRAP image series, CP data, point FRAP data and FCS data were acquired with a Leica TCS SP2 AOBS FCS and with a Leica TCS SP5 AOBS FCS (Leica Microsystems, Mannheim, Germany) equipped with a 63×/1.2NA water immersion lens or with a Zeiss LSM 510 ConfoCor2 system (Carl Zeiss AIM, Jena, Germany) equipped with a 40×/1.2NA water immersion lens. For H1-EGFP, we used the 488 nm line of an Argon laser for excitation and a detection band-pass window of 500–550 nm. For imaging, photomultiplier tubes were used. For CP, point FRAP and FCS, avalanche photodiode single-photon counting detectors were used. Live cells were maintained at 37 °C on the microscopes using either a PeCon stage heating system (PeCon, Erbach, Germany), a Life Cell Imaging stage heating system (LCI, Seoul, South Korea) or an EMBL incubation box (EMBL-EM, Heidelberg, Germany).

Imaging FRAP, point FRAP, CP

For imaging FRAP, a rectangular strip bleach region was defined. Acquisition of 10 prebleach images (time resolution 0.6 s) was followed by two bleach frames, 10 postbleach images (time resolution 0.6 s) and additional 40 postbleach images (time resolution 6 s). The data were then processed as described elsewhere [91, 92] to yield the mean intensity recovery curve integrated over the bleach region. This was then fitted with Additional file 1: Eq. S92, resulting in three different fractions, a diffusion coefficient and a dissociation rate. Alternatively, an average projection along the direction of the longer dimension of the bleach strip was plotted as profile along the other direction for all time points studied. Appropriate normalization steps [64, 92] (Additional file 1: Fig. S11) yielded profile plots that were then fitted with Additional file 1: Eq. S91 to yield an apparent diffusion coefficient.

Point FRAP and CP data were acquired as described elsewhere [43, 93, 94]. CP data were fitted with Additional file 1: Eq. S93 to yield two independent dissociation rates and corresponding fractions. Point FRAP data were fitted as described in Im et al. [43], however with two binding states.

Fluorescence correlation spectroscopy

FCS data were acquired at cellular positions selected in confocal images for 30–60 s. A frequently encountered problem of FCS, especially in living samples, is slow but pronounced signal fluctuations, e.g., due to bulk photobleaching [43, 93–95] (Additional file 1: Fig. S8). Fluctuations contribute to the resulting correlation function (CF) weighted with the square of their brightness so that often slow fluctuations obscured completely the contributions from single diffusing molecules and rendered a further evaluation impossible. To overcome this obstacle, raw fluorescence intensity traces were saved to disk and then processed using the FluctuationAnalyzer software [90] written in our laboratory in C++ and LabVIEW (National Instruments, Austin, TX, USA) that used a local average approach where the CF is calculated over a small time window Θ and subsequently averaged over the complete length T according to

$$G_{kl}(t',\tau) = \frac{\langle \delta F_k(t)\delta F_l(t+\tau)\rangle_{t',\Theta}}{\langle F_k(t)\rangle_{t',\Theta}\langle F_l(t)\rangle_{t',\Theta}}$$
$$\text{with} \quad \langle\ldots\rangle_{t',\Theta} = \frac{1}{\Theta}\int_{t'}^{t'+\Theta} dt\ldots, \tag{4}$$
$$G_{kl}(\tau) = \langle G(t,\tau)\rangle \quad \text{with} \quad \langle\ldots\rangle = \langle\ldots\rangle_{0,T}.$$

Here, k, $l = 1$, 2 represent the two available detection channels. For $k = l = 1$, 2, the autocorrelation function (ACF) of channel 1, 2 is obtained, whereas $k = 1$, $l = 2$ yields the cross-correlation function (CCF). A good yet subjective criterion for a proper choice of the window size is a smooth transition of the CF to zero. In a more systematic way, we fitted the data with appropriate model functions, Eq. 3, 5. When finding a range of window sizes where, e.g., the relaxation time obtained from the fit was independent of the window size, we selected a window size within the range. Otherwise, the data were not taken into consideration.

To fit FCS data of the diffusive fraction of histone molecules and of free EGFP, we used the standard fit function modeling free anomalous diffusion and fluorescent protein-like blinking [96]

$$G_{kl}(\tau) = \frac{1}{N}\left[1 - \Theta_T + \Theta_T \exp\left(-\frac{\tau}{\tau_T}\right)\right]\cdot \left[1+\left(\frac{\tau}{\tau_D}\right)^{\alpha}\right]^{-1}\left[1+\frac{1}{\kappa^2}\left(\frac{\tau}{\tau_D}\right)^{\alpha}\right]^{-1/2} \tag{5}$$

where N is the number of molecules in the focal volume, Θ_T the fraction of molecules in a non-fluorescent state with lifetime τ_T, $\tau_D = w_0^2/4D$ the diffusion correlation time, α the anomaly parameter and $\kappa = z_0/w_0$ the ratio of axial and lateral focal radius. Fitting FCS data with a chromatin relaxation model is described above.

Numerical modeling of chromatin conformations

For the visualization and for the analysis of static physical properties of chromatin, we simulated chains as beads occupying sites on a three-dimensional cubic lattice with a grid constant of $a = 30$ nm. Neighboring sites were connected by chain segments, and neighbors could occupy any of the surrounding 26 sites, resulting in a mean distance or bond length of $b = \sqrt{2}a = 42$ nm corresponding to 2500 bp when assuming 60 bp/nm or 3.5 nucleosomes/11 nm and 195 bp nucleosomal repeat length. The grid constant is set to an assumed fiber diameter of 30 nm. Double occupancy of sites is suppressed to ensure self-avoidance of the chain. In general, chains were modeled as a sequence of loops and linear stretches. Properties such as radii of gyration were calculated according to the respective definition. Calculations were implemented in Python 3.3, and renderings were generated using the VPython module.

Calculation of genomic contact probability maps

We calculated genomic contact probability maps for simulated chromatin conformation using Additional file 1: Eq. S25 and the algorithm described in the Additional file 1: Supplementary Text. Data were saved as matrices with a resolution of 2.5 kb. For the configurations used in Fig. 1d, e we used the following parameters:

Figure 1d: theta-solvent loop-rosette conformation; lin(x)—linear stretch of x kb; dom(y)—domain of y kb consisting of a set of loops; loop(*z*)—looped stretch of *z* kb; loops with multiple numbers were varied synchronously in length and then averaged to generate variation in loop length. lin(100) – dom (1000) [loop(166) – loop(167) – loop(166) – loop(167) – loop(166)] – lin(150) – dom (1300) [loop(100/125/150/175/200) – loop(95) – loop(90) – loop(85) – loop(120/145/170/195/220) – loop(150) – loop(125) – loop(115) – loop(160) – loop(150)] – lin(150) – dom(1000) [loop(185) – loop(120) – loop(95) – loop(120) – loop(235) – loop(245)] – lin(50) – dom(1100) [loop(138) – loop(160) – loop(95) – loop(170) – loop(160) – loop(183) – loop(128) – loop(68)] – lin(150)

Figure 1e: globular conformation; lin(*x*)—linear stretch of *x* kb; dom(*y*)—domain of *y* kb consisting of a globular stretch; glob(*z*)—globular stretch of *z* kb. lin(100) – dom(1000) [glob(1000)] – lin(150) – dom(1300) [glob(1300)] – lin(150) – dom(1000) [glob(1000)] – lin(50) – dom(1100) [glob(1100)] – lin(150)

Analysis of genomic contact probability maps

To detect peaks in the two-dimensional contact probability maps, both experimental and simulated data were imported into a software module written in LabVIEW. It allowed to interpolate data to a resolution of 2.5 kb and to symmetrize them. After manually selecting a domain region easily recognizable as square area of increased contact probabilities (Fig. 1a, b, d, e), the diagonal and its vicinity of ±30–75 kb (±12–30 data points of 2.5 kb) were removed. A one-dimensional average of a maximum and a mean projection (Additional file 1: Fig. S1) yielded a one-dimensional profile, to which a peak detection algorithm was applied based on parabolic fitting to continuous stretches of 30 kb (12 data points). Maxima above 80 % of the profile average were accepted as peak locations.

Then, local average projections in a 25- to 30-kb vicinity of each peak were calculated (Additional file 1: Fig. S1), to which the same peak detection algorithm was applied. Thus, for each peak detected in this way, a pair of genomic sites of high interaction probability could be obtained, corresponding to a loop base. Pairs detected in both directions featured higher recognition probability and were marked with black circles (Fig. 1a, b, d, e), and those detected with lower probability, i.e., only in one direction, were marked with gray circles. This approach corresponds to an effective thresholding of distances instead of using their values [97] justified by the dynamic nature of domains and is applied to non-corrected and smoothed data similar to Giorgetti et al. [28]. The binarization is especially robust against bias effects, which are not completely known even though corrections can be applied [98, 99].

Additional file

Additional file 1. Additional documentation.

Authors' contributions

MW and KR conceived the project. MW, KR and TAK wrote the paper. TAK acquired T2C data. MW performed experiments, wrote software, evaluated results and developed theory. All authors read and approved the final manuscript.

Author details

[1] Cell Biology and Biophysics Unit, European Molecular Biology Laboratory (EMBL), Meyerhofstrasse 1, 69117 Heidelberg, Germany. [2] Biophysical Genomics Group, Department of Cell Biology and Genetics, Erasmus Medical Center, Dr. Molewaterplein 50, 3015 GE Rotterdam, The Netherlands. [3] Research Group Genome Organization and Function, Deutsches Krebsforschungszentrum (DKFZ) & BioQuant, Im Neuenheimer Feld 280, 69120 Heidelberg, Germany.

Acknowledgements

We are indebted to Thibaud Jegou for the cell line that stably expresses H1.0-EGFP and Jutta Bulkescher as well as Birgit Koch for some help with cell culture. We are grateful to Katalin Fejes-Tóth and A.M.A. Imam for critical comments. We would like to thank Kerstin Wendt for supporting the T2C experiments. This work was supported by EMBL research funding.

Competing interests

The authors declare that they have no competing interests.

Received: 7 September 2016 Accepted: 12 September 2016

References

1. Belmont AS. Large-scale chromatin organization: the good, the surprising, and the still perplexing. Curr Opin Cell Biol. 2014;26:69–78.
2. Bickmore WA. The spatial organization of the human genome. Annu Rev Genom Hum Genet. 2013;14:67–84.
3. Gibcus JH, Dekker J. The hierarchy of the 3D genome. Mol Cell. 2013;49:773–82.
4. Rouquette J, Cremer C, Cremer T, Fakan S. Functional nuclear architecture studied by microscopy: present and future. Int Rev Cell Mol Biol. 2010;282:1–91.
5. Dekker J, Rippe K, Dekker M, Kleckner N. Capturing chromosome conformation. Science. 2002;295:1306–11.
6. Tolhuis B, Palstra RJ, Splinter E, Grosveld F, de Laat W. Looping and interaction between hypersensitive sites in the active beta-globin locus. Mol Cell. 2002;10:1453–65.
7. Dekker J, Marti-Renom MA, Mirny LA. Exploring the three-dimensional organization of genomes: interpreting chromatin interaction data. Nat Rev Genet. 2013;14:390–403.
8. Kolovos P, van de Werken HJ, Kepper N, Zuin J, Brouwer RW, Kockx CE, Wendt KS, van Ijcken WF, Grosveld F, Knoch TA. Targeted chromatin capture (T2C): a novel high resolution high throughput method to detect genomic interactions and regulatory elements. Epigenet Chromatin. 2014;7:10.
9. Jin F, Li Y, Dixon JR, Selvaraj S, Ye Z, Lee AY, Yen C-A, Schmitt AD, Espinoza CA, Ren B. A high-resolution map of the three-dimensional chromatin interactome in human cells. Nature. 2014;503:290–4.
10. Lieberman-Aiden E, van Berkum NL, Williams L, Imakaev M, Ragoczy T, Telling A, Amit I, Lajoie BR, Sabo PJ, Dorschner MO, et al. Comprehensive mapping of long-range interactions reveals folding principles of the human genome. Science. 2009;326:289–93.
11. Nora EP, Lajoie BR, Schulz EG, Giorgetti L, Okamoto I, Servant N, Piolot T, van Berkum NL, Meisig J, Sedat J, et al. Spatial partitioning of the regulatory landscape of the X-inactivation centre. Nature. 2012;485:381–5.

12. Rao SS, Huntley MH, Durand NC, Stamenova EK, Bochkov ID, Robinson JT, Sanborn AL, Machol I, Omer AD, Lander ES, Aiden EL. A 3D map of the human genome at kilobase resolution reveals principles of chromatin looping. Cell. 2014;159:1665–80.
13. Nagano T, Lubling Y, Stevens TJ, Schoenfelder S, Yaffe E, Dean W, Laue ED, Tanay A, Fraser P. Single-cell Hi-C reveals cell-to-cell variability in chromosome structure. Nature. 2013;502:59–64.
14. Dixon JR, Selvaraj S, Yue F, Kim A, Li Y, Shen Y, Hu M, Liu JS, Ren B. Topological domains in mammalian genomes identified by analysis of chromatin interactions. Nature. 2012;485:376–80.
15. Cremer T, Cremer T, Cremer C, Cremer C. Chromosome territories, nuclear architecture and gene regulation in mammalian cells. Nat Rev Genet. 2001;2:292–301.
16. Misteli T. Beyond the sequence: cellular organization of genome function. Cell. 2007;128:787–800.
17. Müller WG, Rieder D, Karpova TS, John S, Trajanoski Z, McNally JG. Organization of chromatin and histone modifications at a transcription site. J Cell Biol. 2007;177:957–67.
18. Shopland LS, Johnson CV, Byron M, McNeil J, Lawrence JB. Clustering of multiple specific genes and gene-rich R-bands around SC-35 domains: evidence for local euchromatic neighborhoods. J Cell Biol. 2003;162:981–90.
19. Verschure PJ, van Der Kraan I, Manders EM, van Driel R. Spatial relationship between transcription sites and chromosome territories. J Cell Biol. 1999;147:13–24.
20. Pope BD, Ryba T, Dileep V, Yue F, Wu W, Denas O, Vera DL, Wang Y, Hansen RS, Canfield TK, et al. Topologically associating domains are stable units of replication-timing regulation. Nature. 2014;515:402–5.
21. Joffe B, Leonhardt H, Solovei I. Differentiation and large scale spatial organization of the genome. Curr Opin Genet Dev. 2010;20:562–9.
22. Kolovos P, Knoch TA, Grosveld FG, Cook PR, Papantonis A. Enhancers and silencers: an integrated and simple model for their function. Epigenet Chromatin. 2012;5:1.
23. Nora EP, Dekker J, Heard E. Segmental folding of chromosomes: a basis for structural and regulatory chromosomal neighborhoods? BioEssays. 2013;35:818–28.
24. Sexton T, Cavalli G. The role of chromosome domains in shaping the functional genome. Cell. 2015;160:1049–59.
25. Li G, Zhu P. Structure and organization of chromatin fiber in the nucleus. FEBS Lett. 2015;589(20 Pt A):2893–904. doi:10.1016/j.febslet.2015.04.023.
26. Maeshima K, Hihara S, Eltsov M. Chromatin structure: does the 30-nm fibre exist in vivo? Curr Opin Cell Biol. 2010;22:291–7.
27. Stehr R, Schöpflin R, Ettig R, Kepper N, Rippe K, Wedemann G. Exploring the conformational space of chromatin fibers and their stability by numerical dynamic phase diagrams. Biophys J. 2010;98:1028–37.
28. Giorgetti L, Galupa R, Nora EP, Piolot T, Lam F, Dekker J, Tiana G, Heard E. Predictive polymer modeling reveals coupled fluctuations in chromosome conformation and transcription. Cell. 2014;157:950–63.
29. Jhunjhunwala S, van Zelm MC, Peak MM, Cutchin S, Riblet R, van Dongen JJ, Grosveld FG, Knoch TA, Murre C. The 3D structure of the immunoglobulin heavy-chain locus: implications for long-range genomic interactions. Cell. 2008;133:265–79.
30. Münkel C, Langowski J. Chromosome structure described by a polymer model. Phys Rev E. 1998;57:5888–96.
31. Naumova N, Imakaev M, Fudenberg G, Zhan Y, Lajoie BR, Mirny LA, Dekker J. Organization of the mitotic chromosome. Science. 2013;342:948–53.
32. Cremer T, Cremer M, Hubner B, Strickfaden H, Smeets D, Popken J, Sterr M, Markaki Y, Rippe K, Cremer C. The 4D nucleome: evidence for a dynamic nuclear landscape based on co-aligned active and inactive nuclear compartments. FEBS Lett. 2015;589(20 Pt A):2931–43. doi:10.1016/j.febslet.2015.05.037.
33. Gerlich D, Beaudouin J, Kalbfuss B, Daigle N, Eils R, Ellenberg J. Global chromosome positions are transmitted through mitosis in mammalian cells. Cell. 2003;112:751–64.
34. Belmont AS. Visualizing chromosome dynamics with GFP. Trends Cell Biol. 2001;11:250–7.
35. Wachsmuth M, Caudron-Herger M, Rippe K. Genome organization: balancing stability and plasticity. Biochim Biophys Acta. 2008;1783:2061–79.
36. Pederson T. Repeated TALEs: visualizing DNA sequence localization and chromosome dynamics in live cells. Nucleus. 2014;5:1–4.
37. Dion V, Gasser SM. Chromatin movement in the maintenance of genome stability. Cell. 2013;152:1355–64.
38. Jegou T, Chung I, Heuvelmann G, Wachsmuth M, Görisch SM, Greulich-Bode K, Boukamp P, Lichter P, Rippe K. Dynamics of telomeres and promyelocytic leukemia nuclear bodies in a telomerase negative human cell line. Mol Biol Cell. 2009;20:2070–82.
39. Levi V, Ruan Q, Plutz M, Belmont AS, Gratton E. Chromatin dynamics in interphase cells revealed by tracking in a two-photon excitation microscope. Biophys J. 2005;89:4275–85.
40. Lucas JS, Zhang Y, Dudko OK, Murre C. 3D trajectories adopted by coding and regulatory DNA elements: first-passage times for genomic interactions. Cell. 2014;158:339–52.
41. Chen B, Gilbert LA, Cimini BA, Schnitzbauer J, Zhang W, Li GW, Park J, Blackburn EH, Weissman JS, Qi LS, Huang B. Dynamic imaging of genomic loci in living human cells by an optimized CRISPR/Cas system. Cell. 2013;155:1479–91.
42. Baum M, Erdel F, Wachsmuth M, Rippe K. Retrieving the intracellular topology from multi-scale protein mobility mapping in living cells. Nat Commun. 2014;5:4494.
43. Im K-B, Schmidt U, Kang MS, Lee JY, Bestvater F, Wachsmuth M. Diffusion and binding analyzed with combined point FRAP and FCS. Cytometry A. 2013;83:876–89.
44. Halverson JD, Smrek J, Kremer K, Grosberg AY. From a melt of rings to chromosome territories: the role of topological constraints in genome folding. Rep Prog Phys. 2014;77:022601.
45. Rosa A, Zimmer C. Computational models of large-scale genome architecture. Int Rev Cell Mol Biol. 2014;307:275–349.
46. Lumma D, Keller S, Vilgis T, Radler JO. Dynamics of large semiflexible chains probed by fluorescence correlation spectroscopy. Phys Rev Lett. 2003;90:218301.
47. Shusterman R, Alon S, Gavrinyov T, Krichevsky O. Monomer dynamics in double- and single-stranded DNA polymers. Phys Rev Lett. 2004;92:048303.
48. Cohen AE, Moerner WE. Principal-components analysis of shape fluctuations of single DNA molecules. Proc Natl Acad Sci USA. 2007;104:12622–7.
49. McHale K, Mabuchi H. Precise characterization of the conformation fluctuations of freely diffusing DNA: beyond Rouse and Zimm. J Am Chem Soc. 2009;131:17901–7.
50. Petrov EP, Ohrt T, Winkler RG, Schwille P. Diffusion and segmental dynamics of double-stranded DNA. Phys Rev Lett. 2006;97:258101.
51. Tothova J, Brutovsky B, Lisy V. Monomer dynamics in single- and double-stranded DNA coils. Eur Phys J E Soft Matter. 2007;24:61–7.
52. Doi M, Edwards SF. The theory of polymer dynamics. Oxford: Oxford University Press; 1986.
53. Knoch TA, Wachsmuth M, Kepper N, Lesnussa M, Abuseiris A, Ali Imam AM, Kolovos P, Zuin J, Kockx CEM, Brouwer RWW, van de Werken HJG, van IJken WFJ, Wendt5 KS, Grosveld FG (in press) The detailed 3D multi-loop aggregate/rosette chromatin architecture and functional dynamic organization of the human and mouse genomes. Epigenetics Chromatin. doi:10.1186/s13072-016-0089-x
54. Misteli T, Gunjan A, Hock R, Bustin M, Brown DT. Dynamic binding of histone H1 to chromatin in living cells. Nature. 2000;408:877–81.
55. Lever MA, Th'ng JP, Sun X, Hendzel MJ. Rapid exchange of histone H1.1 on chromatin in living human cells. Nature. 2000;408:873–6.
56. Tanay A, Cavalli G. Chromosomal domains: epigenetic contexts and functional implications of genomic compartmentalization. Curr Opin Genet Dev. 2013;23:197–203.
57. De Gennes PG. Dynamics of entangled polymer solutions. II. Inclusion of hydrodynamic interactions. Macromolecules. 1976;9:594–8.
58. Erenpreisa J. Large rossettes: the element of the suprachromonemal organisation of interphase cell nucleus (Russ.). Proc Latv Acad Sci. 1989;7:68–71.
59. Sachs RK, van den Engh G, Trask B, Yokota H, Hearst JE. A random-walk/giant-loop model for interphase chromosomes. Proc Natl Acad Sci USA. 1995;92:2710–4.
60. Weidemann T, Wachsmuth M, Knoch TA, Müller G, Waldeck W, Langowski J. Counting nucleosomes in living cells with a combination of fluorescence correlation spectroscopy and confocal imaging. J Mol Biol. 2003;334:229–40.

61. Carrero G, Crawford E, Hendzel MJ, de Vries G. Characterizing fluorescence recovery curves for nuclear proteins undergoing binding events. Bull Math Biol. 2004;66:1515–45.
62. Brown DT, Izard T, Misteli T. Mapping the interaction surface of linker histone H10 with the nucleosome of native chromatin in vivo. Nat Struct Mol Biol. 2006;13:250–5.
63. Catez F, Ueda T, Bustin M. Determinants of histone H1 mobility and chromatin binding in living cells. Nat Struct Mol Biol. 2006;13:305–10.
64. Stasevich TJ, Mueller F, Brown DT, McNally JG. Dissecting the binding mechanism of the linker histone in live cells: an integrated FRAP analysis. EMBO J. 2010;29:1225–34.
65. Raghuram N, Carrero G, Stasevich TJ, McNally JG, Th'ng J, Hendzel MJ. Core histone hyperacetylation impacts cooperative behavior and high-affinity binding of histone H1 to chromatin. Biochemistry. 2010;49:4420–31.
66. Harshman SW, Young NL, Parthun MR, Freitas MA. H1 histones: current perspectives and challenges. Nucleic Acids Res. 2013;41:9593–609.
67. van Kampen NG. Stochastic processes in physics and chemistry. Amsterdam: Elsevier; 1992.
68. Capoulade J, Wachsmuth M, Hufnagel L, Knop M. Quantitative fluorescence imaging of protein diffusion and interaction in living cells. Nat Biotechnol. 2011;29:835–9.
69. Wachsmuth M. Fluoreszenzfluktuationsmikroskopie: Entwicklung Eines Prototyps, Theorie Und Messung Der Beweglichkeit Von Biomolekülen Im Zellkern. Ruprecht-Karls-Universität Heidelberg, Fakultät für Physik und Astronomie; 2001.
70. Tóth KF, Knoch TA, Wachsmuth M, Stöhr M, Frank-Stöhr M, Bacher CP, Müller G, Rippe K. Trichostatin A induced histone acetylation causes decondensation of interphase chromatin. J Cell Sci. 2004;117:4277–87.
71. Görisch SM, Wachsmuth M, Fejes Tóth K, Lichter P, Rippe K. Histone acetylation increases chromatin accessibility. J Cell Sci. 2005;118:5825–34.
72. Hihara S, Pack C-G, Kaizu K, Tani T, Hanafusa T, Nozaki T, Takemoto S, Yoshimi T, Yokota H, Imamoto N, et al. Local nucleosome dynamics facilitate chromatin accessibility in living mammalian cells. Cell Rep. 2012;2:1645–56.
73. Zeskind BJ, Jordan CD, Timp W, Trapani L, Waller G, Horodincu V, Ehrlich DJ, Matsudaira P. Nucleic acid and protein mass mapping by live-cell deep-ultraviolet microscopy. Nat Methods. 2007;4:567–9.
74. Kepper N, Foethke D, Stehr R, Wedemann G, Rippe K. Nucleosome geometry and internucleosomal interactions control the chromatin fiber conformation. Biophys J. 2008;95:3692–705.
75. Bystricky K, Heun P, Gehlen L, Langowski J, Gasser SM. Long-range compaction and flexibility of interphase chromatin in budding yeast analyzed by high-resolution imaging techniques. Proc Natl Acad Sci USA. 2004;101:16495–500.
76. Cook PR, Marenduzzo D. Entropic organization of interphase chromosomes. J Cell Biol. 2009;186:825–34.
77. Rosa A, Becker NB, Everaers R. Looping probabilities in model interphase chromosomes. Biophys J. 2010;98:2410–9.
78. Berg OG, von Hippel PH. Facilitated target location in biological systems. J Biol Chem. 1989;264:675–8.
79. Di Rienzo C, Piazza V, Gratton E, Beltram F, Cardarelli F. Probing short-range protein Brownian motion in the cytoplasm of living cells. Nat Commun. 2014;5:5891.
80. Bancaud A, Lavelle C, Huet S, Ellenberg J. A fractal model for nuclear organization: current evidence and biological implications. Nucleic Acids Res. 2012;40:8783–92.
81. van de Corput MP, de Boer E, Knoch TA, van Cappellen WA, Quintanilla A, Ferrand L, Grosveld FG. Super-resolution imaging reveals three-dimensional folding dynamics of the beta-globin locus upon gene activation. J Cell Sci. 2012;125:4630–9.
82. Barbieri M, Chotalia M, Fraser J, Lavitas L-M, Dostie J, Pombo A, Nicodemi M. Complexity of chromatin folding is captured by the strings and binders switch model. Proc Natl Acad Sci USA. 2012;109:16173–8.
83. Baù D, Sanyal A, Lajoie BR, Capriotti E, Byron M, Lawrence JB, Dekker J, Marti-Renom MA. The three-dimensional folding of the α-globin gene domain reveals formation of chromatin globules. Nat Struct Mol Biol. 2011;18:107–14.
84. Hu M, Deng K, Qin Z, Dixon J, Selvaraj S, Fang J, Ren B, Liu JS. Bayesian inference of spatial organizations of chromosomes. PLoS Comput Biol. 2013;9:e1002893.
85. Meluzzi D, Arya G. Recovering ensembles of chromatin conformations from contact probabilities. Nucleic Acids Res. 2012;41:63–75.
86. Dostie J, Dekker J. Mapping networks of physical interactions between genomic elements using 5C technology. Nat Protoc. 2007;2:988–1002.
87. Orlando V. Mapping chromosomal proteins in vivo by formaldehyde-crosslinked-chromatin immunoprecipitation. Trends Biochem Sci. 2000;25:99–104.
88. Dross N, Spriet C, Zwerger M, Muller G, Waldeck W, Langowski J. Mapping eGFP oligomer mobility in living cell nuclei. PLoS ONE. 2009;4:e5041.
89. Knoch TA. Approaching the three-dimensional organization of the human genome. Ruprecht-Karls-Universität Heidelberg, Fakultät für Physik und Astronomie; 2002.
90. Wachsmuth M, Conrad C, Bulkescher J, Koch B, Mahen R, Isokane M, Pepperkok R, Ellenberg J. High-throughput fluorescence correlation spectroscopy enables analysis of proteome dynamics in living cells. Nat Biotechnol. 2015;33:384–9.
91. Wachsmuth M. Molecular diffusion and binding analyzed with FRAP. Protoplasma. 2014;251:373–82.
92. Wachsmuth M, Weisshart K. Fluorescence photobleaching and fluorescence correlation spectroscopy: two complementary technologies to study molecular dynamics in living cells. In: Shorte SL, Frischknecht F, editors. Imaging cellular and molecular biological functions. Berlin: Springer; 2007. p. 179–228.
93. Schmidt U, Im K-B, Benzing C, Janjetovic S, Rippe K, Lichter P, Wachsmuth M. Assembly and mobility of exon-exon junction complexes in living cells. RNA. 2009;15:862–76.
94. Wachsmuth M, Weidemann T, Müller G, Hoffmann-Rohrer UW, Knoch TA, Waldeck W, Langowski J. Analyzing intracellular binding and diffusion with continuous fluorescence photobleaching. Biophys J. 2003;84:3353–63.
95. Ries J, Bayer M, Csucs G, Dirkx R, Solimena M, Ewers H, Schwille P. Automated suppression of sample-related artifacts in Fluorescence correlation spectroscopy. Opt Express. 2010;18:11073–82.
96. Wachsmuth M, Waldeck W, Langowski J. Anomalous diffusion of fluorescent probes inside living cell nuclei investigated by spatially-resolved fluorescence correlation spectroscopy. J Mol Biol. 2000;298:677–89.
97. Lesne A, Riposo J, Roger P, Cournac A, Mozziconacci J. 3D genome reconstruction from chromosomal contacts. Nat Methods. 2014;11:1141–3.
98. Imakaev M, Fudenberg G, McCord RP, Naumova N, Goloborodko A, Lajoie BR, Dekker J, Mirny LA. Iterative correction of Hi-C data reveals hallmarks of chromosome organization. Nat Methods. 2012;9:999–1003.
99. Yaffe E, Tanay A. Probabilistic modeling of Hi-C contact maps eliminates systematic biases to characterize global chromosomal architecture. Nat Genet. 2011;43:1059–65.

Additional File 1: Additional Documentation for

Dynamic properties of independent chromatin domains measured by correlation spectroscopy in living cells

Malte Wachsmuth[1*], Tobias A. Knoch[2] and Karsten Rippe[3]

[1] Cell Biology and Biophysics Unit, European Molecular Biology Laboratory (EMBL), Meyerhofstrasse 1, D-69117 Heidelberg, Germany

[2] Biophysical Genomics Group, Dept. Cell Biology & Genetics, Erasmus Medical Center, Dr. Molewaterplein 50, NL-3015 GE Rotterdam, The Netherlands

[3] Research Group Genome Organization & Function, Deutsches Krebsforschungszentrum (DKFZ) & BioQuant, Im Neuenheimer Feld 280, D-69120 Heidelberg, Germany

[*] Correspondence: m.wachsmuth@gmx.net

Content

Supplementary Text

Supplementary Figures

Supplementary References

Supplementary Text

Static properties of polymers

1.1. The linear freely jointed chain

The freely jointed chain forms the basis to derive static and dynamic properties of polymers [1, 2]. Being a mere theoretical construct, it is well suited to describe more realistic models such as the Gaussian, the persistent/worm-like chain or the Kratky-Porod model.

The freely jointed chain is a linear chain of rigid rods of length b that are connected with completely flexible joints. Each segment i corresponds to the vector $\boldsymbol{u}_i$ of length l and the end-to-end vector is thus

$$\boldsymbol{R} = \sum_{i=1}^{N} \boldsymbol{u}_i, \quad |\boldsymbol{u}_i| = b. \tag{1}$$

The mean squared end-to-end distance is given as

$$\left\langle \boldsymbol{R}^2 \right\rangle = \left\langle \left(\sum_{i=1}^{N} \boldsymbol{u}_i \right)^2 \right\rangle = \sum_{i=1}^{N} \left\langle \boldsymbol{u}_i^2 \right\rangle + \sum_{i \neq j} \underbrace{\left\langle \boldsymbol{u}_i \boldsymbol{u}_j \right\rangle}_{=0} = Nb^2 = Lb \tag{2}$$

where b is the so-called Kuhn segment length and L the total contour length. Any hydrodynamic, electrostatic or excluded volume effects and interactions are disregarded.

1.2. The persistent or worm-like chain, Kratky-Porod model

These simplifications hold as well for continuous flexible or persistent chains where b becomes related to the elastic properties of the chain. It can be shown that for a continuous Markov chain, the average angle between segments at a distance s obeys

$$\left\langle \cos\Theta(s+s') \right\rangle = \left\langle \cos\Theta(s) \right\rangle \left\langle \cos\Theta(s') \right\rangle \quad \Rightarrow \quad \left\langle \cos\Theta(s) \right\rangle = \exp\left(-\frac{s}{l_p} \right), \tag{3}$$

i.e., the chain has an exponentially decaying directional memory, whose characteristic length l_p is the so-called persistence length. The Kratky-Porod model relates this so far empirical number to the bending elasticity or the energy required to bend it into a certain curvature.

In the continuous model, tangential vectors instead of segments are used to calculate the the mean squared end-to-end distance:

$$\begin{aligned} \left\langle \boldsymbol{R}^2 \right\rangle &= \int_0^L ds \int_0^L ds' \left\langle \boldsymbol{u}(s) \boldsymbol{u}(s') \right\rangle = 2l_p \left[\frac{L}{l_p} - 1 + \exp\left(-\frac{L}{l_p} \right) \right] \\ &= \begin{cases} L^2 & L < l_p, \\ 2Ll_p & L > l_p. \end{cases} \end{aligned} \tag{4}$$

The second case shows that in the long contour length limit, the worm-like chain behaves like a freely jointed chain and the Kuhn segment length relates to the persistence length as

$$b = 2l_p. \tag{5}$$

1.3. The Gaussian chain

If the direction of real or virtual (Kuhn) segments of a polymer are stochastically independent or feature an exponentially decaying correlation the central limit theorem allows to describe the end-to-end distribution of the chain with a Gaussian function

$$\psi(\boldsymbol{R}) = \left(\frac{3}{2\pi\langle \boldsymbol{R}^2\rangle}\right)^{3/2} \exp\left(-\frac{3\boldsymbol{R}^2}{2\langle \boldsymbol{R}^2\rangle}\right). \tag{6}$$

In case segments are completely independent at distances larger than *b*, the polymer is a Markov chain, and for points chosen equally distributed along the chain and sufficiently far apart the pair-wise distance distributions are independent and Gaussian, too, i.e., subchains behave in the same way.

Thus, both freely jointed and worm-like chains can be described as Gaussian chains of virtual beads on a string that have a Gaussian distance distribution. Their spacing usually does not match the chemical bond length but is chosen such that their static and dynamic properties match the real polymer. This serves as a basis to derive the dynamic properties of polymers in the Rouse and Zimm models.

1.4. Properties of Gaussian chains

The most obvious characteristic size of a coiled linear chain is the mean squared end-to-end distance, which can also be identified with the correlation length of the coil and which defines the order of magnitude of all characteristic size properties.

The radius of gyration is defined as the mean squared mutual distance of all segments or equivalently the mean squared distance of the segments from the center of mass:

$$\begin{aligned} R_g^2 &= \frac{1}{2N^2}\left\langle \sum_{i=1}^{N}\sum_{j=1}^{N} \boldsymbol{R}_{ij}^2 \right\rangle = \frac{1}{N}\left\langle \sum_{k=1}^{N} (\boldsymbol{R}_k - \boldsymbol{R}_{cm})^2 \right\rangle \\ &= \frac{1}{6}\langle \boldsymbol{R}^2\rangle = \frac{Nb^2}{6} \quad \text{with} \quad \langle \boldsymbol{R}_{ij}^2\rangle = |i-j|b^2. \end{aligned} \tag{7}$$

It is experimentally accessible with scattering methods [3] and determines internal relaxation processes.

The hydrodynamic radius corresponds to the radius of a sphere with the same diffusion coefficient as the coiled chain. It is defined as

$$\begin{aligned} R_h^{-1} &= \frac{1}{N^2}\left\langle \sum_{i=1}^{N}\sum_{j=1}^{N} \frac{1}{|\boldsymbol{R}_{ij}|} \right\rangle, \\ R_h^2 &= \frac{3\pi}{128}\langle \boldsymbol{R}^2\rangle = \frac{3\pi}{128}Nb^2 \quad \text{with} \quad \left\langle \frac{1}{|\boldsymbol{R}_{ij}|} \right\rangle = \sqrt{\frac{6}{\pi}}\frac{1}{|i-j|b}. \end{aligned} \tag{8}$$

The variance of the mean squared end-to-end distance is of the same order as the end-to-end distance itself

$$\frac{\left\langle \boldsymbol{R}^4 \right\rangle - \left\langle \boldsymbol{R}^2 \right\rangle^2}{\left\langle \boldsymbol{R}^2 \right\rangle^2} = \frac{2}{3}. \tag{9}$$

The same applies to the radius of gyration and provides an estimation for size fluctuations in different geometries and topologies.

According to the central limit theorem, the density distribution of segments around the center of mass obeys a Gaussian distribution. In a continuous approximation of the chain, the density distribution and the occupied volume are

$$\begin{gathered} \psi(\boldsymbol{r}) = \exp\left[-\frac{3(\boldsymbol{r} - \boldsymbol{R}_{cm})^2}{2R_g^2} \right], \\ V = \int d^3 r\, \psi(\boldsymbol{r}) = \left(\frac{2\pi}{3} R_g^2 \right)^{3/2} \approx 3.03 R_g^3, \end{gathered} \tag{10}$$

the latter allowing to determine average densities or concentrations. Applying Equation (9) to the definition of the radius of gyration results in an estimation of the upper volume limit induced by fluctuations:

$$\frac{V + \delta V}{V} = 1 + \frac{3}{2} \cdot \sqrt{\frac{2}{3}} = 1 + \sqrt{\frac{3}{2}} \approx 2.22. \tag{11}$$

1.5. Real polymers: interactions between segments

A real polymer is always in a balance between an excluded volume effect represented by a hard and sharp repulsive potential and a weak attractive interaction (van der Waals, electrostatic or entropic) that depends strongly on the solvent conditions [1]: in a ‘good solvent’, the excluded volume interaction dominates and the polymer coil is swollen compared to the ideal chain. In a ‘theta solvent’, repulsive and attractive interactions compensate each other such that the chain behaves like an ideal self-permeating polymer. The last case is a ‘poor solvent’ where the attractive potential dominates, the polymer collapses and it assumes a globular state. This concept was first introduced by Kuhn and Flory [4, 5] and subsequently refined using perturbation calculations and the concept of renormalization groups. In order to distinguish the different cases one can define a swelling coefficient

$$\alpha^2 = \frac{R_g^2}{R_{g,0}^2} \begin{cases} > 1 & \text{good solvent/swollen} \\ = 1 & \Theta \text{ solvent/ideal} \\ < 1 & \text{poor solvent/globular} \end{cases} \tag{12}$$

as the ratio of the radii of gyration of the real and the ideal polymer. It depends on the chain length, resulting in a different dependence of the mean squared distance of two segments [2]:

$$\left\langle \boldsymbol{R}_{nm}^2 \right\rangle = \left(|n-m|^{\nu} b\right)^2 \quad \text{with} \quad \begin{cases} \nu = 3/5 & \text{good solvent,} \\ \nu = 1/2 & \text{theta solvent,} \\ \nu = 1/3 & \text{poor solvent.} \end{cases} \tag{13}$$

For a discrete to a continuous parametrization of the chain, the radius of gyration is

$$R_g^2 = \frac{b^2}{2N^2} \int_0^N dn \int_0^N dm |m-n|^{2\nu} = \frac{N^{2\nu} b^2}{(2\nu+1)(2\nu+2)} = \begin{cases} \dfrac{N^{6/5} b^2}{176/25} \approx \dfrac{N^{6/5} b^2}{7.04} & \nu = \dfrac{3}{5}, \\ \dfrac{Nb^2}{6} & \nu = \dfrac{1}{2}, \\ \dfrac{N^{2/3} b^2}{40/9} \approx \dfrac{N^{2/3} b^2}{4.44} & \nu = \dfrac{1}{3}. \end{cases} \tag{14}$$

For the distance distribution of two segments or beads

$$\psi_{nm}(r) = \psi_{nm}\left(|\boldsymbol{R}_n - \boldsymbol{R}_m|\right) \tag{15}$$

again, the three cases must be treated separately. For the ideal and the globular chain, the compensation and overcompensation, respectively, of the repulsive by the attractive interaction allows to consider the polymer as soft chain [6] and to describe the segment distances as Gaussian distributions when neglecting correction terms of order r^2 and higher [7]:

$$\psi_{nm}(r) = \begin{cases} \left(\dfrac{3}{2\pi|n-m|b^2}\right)^{3/2} \exp\left(-\dfrac{3r^2}{2|n-m|b^2}\right) & \nu = \dfrac{1}{2}, \\ \left(\dfrac{3}{2\pi|n-m|^{2/3} b^2}\right)^{3/2} \exp\left(-\dfrac{3r^2}{2|n-m|^{2/3} b^2}\right) & \nu = \dfrac{1}{3}, \end{cases} \tag{16}$$

which yield the mean squared segment distances according to $\left\langle \boldsymbol{R}_{nm}^2 \right\rangle = \int d^3 r\, r^2 \psi_{nm}(r)$.

For the swollen chain, however, we apply the following conceptual constraints and approximations [1, 2]:

(i) it must be normalized,

(ii) it must yield the above-mentioned mean squared distance, Equation (14),

(iii) $\psi_{nm}(r) = \begin{cases} r^{5/18} & r < |n-m|^{\nu} b, \\ \exp\left(-c r^{5/2}\right) & r > |n-m|^{\nu} b, \end{cases}$

(iv) $\psi_{nm}(r) = f\left(\dfrac{r}{|n-m|^{3/5} b}\right)$,

resulting in the numerical approximation

$$\psi_{nm}(r) \approx \frac{0.29}{\left(|n-m|^{3/5} b\right)^{3.28}} r^{0.28} \exp\left[-1.22\left(\frac{r}{|n-m|^{3/5} b}\right)^{5/2}\right]. \tag{17}$$

1.6. Blobs as globular substructures of the chain

The emergence of globular substructures of a polymer chain in theta- or good-solvent conditions such as the chromatin fiber can be explained as the formation of a chain of so-called 'blobs' when the system is at semi-dilute concentrations [8, 9], i.e., when the concentration is too high for individual molecules to be considered isolated, see also Section 2.9 for further details. The blobs themselves have the same static and dynamic properties of the whole molecule under highly diluted conditions. They can be described as shorter independent linear chains in theta- or good-solvent conditions.

1.7. Properties of circular polymers

In addition, globular substructures may result from the formation of of loops. Therefore, here we describe the static properties of cicrular polymers following the same scheme as above [1, 10, 11]. However, only the ideal and the swollen chain are considered because under poor-solvent conditions, it inherently forms globular structures. The spatial distance distribution of two segments of a ring is composed of both possible paths, resulting in an effective segment distance along the chain

$$\mu(m,n,N) = \frac{|m-n|(N-m+1)}{N}, \quad 0 \le m,n \le N \tag{18}$$

and a mean squared distance of

$$\left\langle \boldsymbol{R}_{nm}^2 \right\rangle = \begin{cases} \mu b^2 & \nu = 1/2, \\ \mu^{6/5} b^2 & \nu = 3/5. \end{cases} \tag{19}$$

This yields a radius of gyration of

$$R_g^2 = \frac{b^2}{2N^2} \int_0^N dn \int_0^N dm\, \mu(m,n,N)^{2\nu} = \begin{cases} \dfrac{Nb^2}{12} = \dfrac{R_{g,\mathrm{lin}}^2}{2} & \nu = \dfrac{1}{2}, \\ \dfrac{N^{6/5} b^2}{16.70} \approx \dfrac{R_{g,\mathrm{lin}}^2}{2.37} & \nu = \dfrac{3}{5}. \end{cases} \tag{20}$$

1.8. Branched polymers: stars and rosettes

For loops and even more for branched polymers, a mean squared end-to-end distance cannot be determined and the mean squared pair-wise segment distance, i.e., the radius of gyration, is used to compare macromolecules of different topologies. Since in branched polymers, the density grows with increasing branching ratio, an excluded volume effect should also be more prominent.

The radius of gyration is calculated as the sum of the mean squared segment distance within branches and between branches. We restrict the previously established approach [12-14] to a single multiple branching point and extend it from ideal to swollen molecules. This yields for the

(i) ideal star-like branched linear chain (theta-solvent conditions with $\nu = 1/2$) the contributions

$$f\frac{b^2}{2N^2}\int_0^{N/f}dn\int_0^{N/f}dm\left|m-n\right| = \frac{Nb^2}{6f^2} \quad \text{within branches,}$$

$$f(f-1)\frac{b^2}{2N^2}\int_0^{N/f}dn\int_0^{N/f}dm(m+n) = \frac{Nb^2(f-1)}{2f^2} \quad \text{between branches} \tag{21}$$

$$\Rightarrow \quad R_g^2 = \frac{Nb^2}{6}\left(\frac{3f-2}{f^2}\right),$$

(ii) ideal rosette-like branched circular chain (theta-solvent conditions with $\nu = 1/2$) the contributions

$$f\frac{b^2}{2N^2}\int_0^{N/f}dn\int_0^{N/f}dm\,\mu(m,n,N/f) = \frac{Nb^2}{12f^2} \quad \text{within branches,}$$

$$f(f-1)\frac{b^2}{2N^2}\int_0^{N/f}dn\int_0^{N/f}dm[\mu(m,0,N/f)+\mu(n,0,N/f)] = \frac{Nb^2(f-1)}{6f^2} \quad \text{between branches} \tag{22}$$

$$\Rightarrow \quad R_g^2 = \frac{Nb^2}{12}\left(\frac{2f-1}{f^2}\right),$$

(iii) swollen star-like branched linear chain (good-solvent conditions with $\nu = 3/5$) using the same approach as above

$$R_g^2 = \frac{N^{6/5}b^2}{7.04}\left(\frac{3.59f-2.59}{f^{2.2}}\right), \tag{23}$$

(iv) swollen rosette-like branched circular chain (good-solvent conditions with $\nu = 3/5$)

$$R_g^2 = \frac{N^{6/5}b^2}{16.70}\left(\frac{1.92f-0.92}{f^{2.2}}\right). \tag{24}$$

1.9. Contact probabilities of polymer segments

The chromatin fiber of a chromosome might be organized in an intricate manner including loops and clusters thereof, but the underlying single linear molecule allows to arrange the polymer segments sequentially. Depending on the topology, the effective contour length or distance σ between two segments with the indices m and n can be calculated using $|n-m|$ for linear and Equation (18) for circular stretches. As an example, segment m is connected to segment $n = m + k + p$ through a linear stretch of k segments and a stretch of p segments into a loop of L segments. The effective distance is thus $\sigma = k + \mu(p,0,L)$. Depending on the topology and the physical properties of the fiber as well as on the solvent conditions, the contact probability, defined as the probability that the two segments come as close as the contact distance d_c or closer to each other, is calculated using Equation (16) and (17):

$$p(\sigma,b,d_c)=4\pi\int_0^{d_c} dr\, r^2\psi(r,\sigma,b),$$

$$\psi(r,\sigma,b)=\begin{Bmatrix} \left(\dfrac{3}{2\pi\sigma b^2}\right)^{3/2}\exp\left(-\dfrac{3r^2}{2\sigma b^2}\right) & \nu=\dfrac{1}{2} \\ \left(\dfrac{3}{2\pi\sigma^{2/3}b^2}\right)^{3/2}\exp\left(-\dfrac{3r^2}{2\sigma^{2/3}b^2}\right) & \nu=\dfrac{1}{3} \\ \dfrac{0.29}{\left(\sigma^{3/5}b\right)^{3.28}}r^{0.28}\exp\left[-1.22\left(\dfrac{r}{\sigma^{3/5}b}\right)^{5/2}\right] & \nu=\dfrac{3}{5} \end{Bmatrix} \Rightarrow$$

$$p(d_c,\sigma,b)=\begin{cases} \operatorname{erf}\left[\left(\dfrac{3d_c^2}{2\sigma b^2}\right)^{1/2}\right]-\dfrac{2}{\pi^{1/2}}\left(\dfrac{3d_c^2}{2\sigma b^2}\right)^{1/2}\exp\left(-\dfrac{3d_c^2}{2\sigma b^2}\right) & \nu=\dfrac{1}{2}, \\ \operatorname{erf}\left[\left(\dfrac{3d_c^2}{2\sigma^{2/3}b^2}\right)^{1/2}\right]-\dfrac{2}{\pi^{1/2}}\left(\dfrac{3d_c^2}{2\sigma^{2/3}b^2}\right)^{1/2}\exp\left(-\dfrac{3d_c^2}{2\sigma^{2/3}b^2}\right) & \nu=\dfrac{1}{3}, \\ 1-\Gamma_{\text{inc,upper}}\left[1.312, 1.22\left(\dfrac{d_c}{\sigma^{3/5}b}\right)^{5/2}\right] & \nu=\dfrac{3}{5}. \end{cases} \tag{25}$$

With this, modelling of the topological sequence of linear, looped or clustered stretches enables to calculate intrachromosomal interaction maps as known e.g. from 3C, 4C, 5C, Hi-C or T2C studies [15-17].

Dynamic properties of polymers

1.10. Rouse model for a linear chain

In order to determine the dynamic properties of polymers, Rouse [1, 18] proposed to model the molecules as Gaussian chains of beads connected with springs. Their spacing b is the the Kuhn segment length, which does not necessarily correspond to the bond length between monomeric units but is determined by the physical properties of the molecule, i.e., the thermally induced root mean squared distance of neighboring beads sensing a harmonic potential U.

Then, for every segment n, the Langevin equation is given as

$$\frac{\partial \boldsymbol{R}_n(t)}{\partial t}=\sum_m \hat{\boldsymbol{H}}_{nm}\left(-\frac{\partial U}{\partial \boldsymbol{R}_m}+\boldsymbol{F}_m(t)\right)+\frac{k_BT}{2}\sum_m\frac{\partial}{\partial \boldsymbol{R}_m}\hat{\boldsymbol{H}}_{nm}. \tag{26}$$

In the Rouse model, the excluded volume interaction and the hydrodynamic interaction (represented by the mobility or Oseen tensor $\hat{\boldsymbol{H}}$) are neglected so that this case is often referred to as free-draining polymer. The Oseen tensor and the interaction potential are written as

$$\hat{\boldsymbol{H}}_{nm}=\frac{\boldsymbol{1}}{\gamma}\delta_{nm}, \quad U=\frac{k}{2}\sum_{n=2}^{N}\left(\boldsymbol{R}_n-\boldsymbol{R}_{n-1}\right)^2 \quad \text{with} \quad k=\frac{3k_BT}{b^2}, \tag{27}$$

where γ stands for the friction coefficient, k for the entropic spring constant and $\boldsymbol{F}$ for the thermally induced random forces. With a transition from a discrete to a continuous model, the Langevin equation simplifies to

$$\gamma \frac{\partial \boldsymbol{R}_n}{\partial t} = k \frac{\partial^2 \boldsymbol{R}_n}{\partial n^2} + \boldsymbol{F}_n \tag{28}$$

with the boundary conditions

$$\left.\frac{\partial \boldsymbol{R}_n}{\partial n}\right|_{n=0} = \left.\frac{\partial \boldsymbol{R}_n}{\partial n}\right|_{n=N} = 0 \tag{29}$$

and the moments of the random forces

$$\langle \boldsymbol{F}_n(t) \rangle = 0, \quad \langle \boldsymbol{F}_n(t) \boldsymbol{F}_m(t') \rangle = 6\gamma k_B T \delta(n-m) \delta(t-t'). \tag{30}$$

An appropriate transform gives normal coordinates $\boldsymbol{X}_p$ according to

$$\boldsymbol{X}_p(t) = \frac{1}{N} \int_0^N dn \cos\left(\frac{p\pi n}{N}\right) \boldsymbol{R}_n(t), \tag{31}$$

for which the equations of motion are then written as

$$\gamma_p \frac{\partial \boldsymbol{X}_p}{\partial t} = -k_p \boldsymbol{X}_p + \boldsymbol{F}_p \tag{32}$$

where

$$\begin{aligned} &\gamma_0 = N\gamma, \quad \gamma_p = 2N\gamma \quad \text{for} \quad p = 1, 2, \ldots, \\ &k_p = \frac{6\pi^2 k_B T}{N b^2} p^2 \quad \text{for} \quad p = 0, 1, 2, \ldots \quad . \end{aligned} \tag{33}$$

For $p > 0$, a solution can be found employing the autocorrelation function of the normal coordinates:

$$\begin{aligned} &\langle \boldsymbol{X}_p(t) \boldsymbol{X}_q(0) \rangle = \delta_{pq} \langle \boldsymbol{X}_p^2(0) \rangle \exp\left(-\frac{t}{\tau_p}\right), \\ &\langle \boldsymbol{X}_p^2(0) \rangle = \frac{3 k_B T}{k_p} = \frac{N b^2}{2\pi^2 p^2}, \\ &\tau_1 = \frac{\gamma_1}{k_1} = \frac{\gamma N^2 b^2}{3\pi^2 k_B T}, \quad \tau_p = \frac{\tau_1}{p^2}, \end{aligned} \tag{34}$$

i.e., they represent independent modes with exponentially decaying correlation functions.

For $p = 0$, on the other hand, one can show using the inverse transform

$$\boldsymbol{R}_n(t) = \boldsymbol{X}_0(t) + 2 \sum_{p=1}^{\infty} \boldsymbol{X}_p(t) \cos\left(\frac{p\pi n}{N}\right) \tag{35}$$

that the mean squared displacement (MSD) of the center of mass of the molecule is described by

$$\left\langle \left[\boldsymbol{X}_0(t)-\boldsymbol{X}_0(0)\right]^2\right\rangle = 6Dt \quad \text{with} \quad D=\frac{k_BT}{N\gamma}. \tag{36}$$

It is worth noting that the end-to-end distance relaxation is dominated by the first mode. This mode corresponds to the rotation of the molecule and thus relates its relaxation time directly to the radius of gyration. However, especially the mass dependence of the diffusion coefficient D and of the relaxation times is contradictory to experimental observations mainly because the hydrodynamic interaction was disregarded so that the Rouse model serves as a good conceptual basis but must be adpated to experimental reality.

A readout that is well accessible experimentally for chromatin in the nucleus of a living cell in interphase is the relative movement of a segment with respect to the center of mass averaged over all segments, i.e., averaged over $n\in[0,N]$. The corresponding correlation function reads

$$\left\langle \boldsymbol{R}'_{\text{seg}}(t)\boldsymbol{R}'_{\text{seg}}(0)\right\rangle = 2\sum_{p=1}^{\infty}\left\langle \boldsymbol{X}_p^2(0)\right\rangle \exp\left(-\frac{t}{\tau_p}\right), \tag{37}$$

i.e., all modes contribute to the averaged movement of the segments according to their amplitude. Likewise, the mean squared displacement of a segment again with respect to the center of mass and averaged over all segments can be obtained, which shows confined diffusion behaviour:

$$\left\langle \left[\boldsymbol{R}'_{\text{seg}}(t)-\boldsymbol{R}'_{\text{seg}}(0)\right]^2\right\rangle = 4\sum_{p=1}^{\infty}\left\langle \boldsymbol{X}_p^2(0)\right\rangle\left[1-\exp\left(-\frac{t}{\tau_p}\right)\right] = 4\sum_{p=1}^{\infty}\left\langle \boldsymbol{X}_p^2(0)\right\rangle - 2\left\langle \boldsymbol{R}'_{\text{seg}}(t)\boldsymbol{R}'_{\text{seg}}(0)\right\rangle. \tag{38}$$

1.11. Rouse model for a ring

For a closed circular chain, the same approach is applied [19], however with different boundary conditions:

$$\boldsymbol{R}_0=\boldsymbol{R}_n,\quad \left.\frac{\partial \boldsymbol{R}_n}{\partial n}\right|_{n=0}=\left.\frac{\partial \boldsymbol{R}_n}{\partial n}\right|_{n=N}. \tag{39}$$

The transform is rewritten as

$$\boldsymbol{X}_p(t)=\frac{1}{N}\int_0^N dn\cos\left(\frac{2p\pi n}{N}\right)\boldsymbol{R}_n(t) \tag{40}$$

and the parameters are

$$\begin{aligned}&\gamma_0=N\gamma,\quad \gamma_p=2N\gamma \quad \text{for} \quad p=1,2,\ldots,\\ &k_p=\frac{24\pi^2k_BT}{Nb^2}p^2 \quad \text{for} \quad p=0,1,2,\ldots,\end{aligned} \tag{41}$$

and the relaxation of the modes changes to

$$\left\langle \boldsymbol{X}_p^2(0)\right\rangle = \frac{3k_BT}{k_p} = \frac{Nb^2}{8\pi^2 p^2},$$
$$\tau_1 = \frac{\gamma_1}{k_1} = \frac{\gamma N^2 b^2}{12\pi^2 k_B T}, \quad \tau_p = \frac{\tau_1}{p^2}. \tag{42}$$

Thus, the relaxation modes of a circular polymer are the even modes of a linear chain of the same length. The same result as for a linear chain is obtained for the zero order mode, the translational diffusion. Also the averaged segment movement relative to the center of mass is given as position correlation function and mean squared displacement, respectively:

$$\left\langle \boldsymbol{R}'_{\text{seg}}(t)\boldsymbol{R}'_{\text{seg}}(0)\right\rangle = 2\sum_{p=1}^{\infty}\left\langle \boldsymbol{X}_p^2(0)\right\rangle \exp\left(-\frac{t}{\tau_p}\right),$$
$$\left\langle \left[\boldsymbol{R}'_{\text{seg}}(t) - \boldsymbol{R}'_{\text{seg}}(0)\right]^2\right\rangle = 4\sum_{p=1}^{\infty}\left\langle \boldsymbol{X}_p^2(0)\right\rangle - 2\left\langle \boldsymbol{R}'_{\text{seg}}(t)\boldsymbol{R}'_{\text{seg}}(0)\right\rangle. \tag{43}$$

1.12. Zimm model for an ideal linear chain

The Zimm model is an extension of the Rouse model describing a so-called non-draining polymer, for which the hydroynamic interaction is also taken into account [20]. The formal approach is the same as for the Rouse model, however, the Oseen tensor or mobility matrix reads

$$\hat{\boldsymbol{H}}_{nm} = \begin{cases} \dfrac{\boldsymbol{1}}{\gamma}\delta_{nm} & n = m, \\ \dfrac{1}{8\pi\eta_s\left|\boldsymbol{R}_{nm}\right|}\left(\hat{\boldsymbol{R}}_{nm}\cdot\hat{\boldsymbol{R}}_{nm} + \boldsymbol{1}\right) & n \neq m, \end{cases} \tag{44}$$

yielding now a set of coupled differential equations

$$\frac{\partial \boldsymbol{R}_n}{\partial t} = \sum_m \hat{\boldsymbol{H}}_{nm}\left(k\frac{\partial^2 \boldsymbol{R}_n}{\partial m^2} + \boldsymbol{F}_m\right) \quad \text{with} \quad \frac{\partial}{\partial \boldsymbol{R}_m}\hat{\boldsymbol{H}}_{nm} = 0. \tag{45}$$

In order to simplify them, it is assumed that the system is sufficiently equilibrated, such that the distance-dependent parameters of the mobility matrix can be averaged over the steady state distribution. For the ideal chain under theta-solvent conditions, this distribution is Gaussian, Equation (16), and the Oseen tensor in Equation (45) is replaced by

$$\hat{\boldsymbol{H}}_{nm} \to \left\langle \hat{\boldsymbol{H}}_{nm}\right\rangle_{\text{eq}} = \int d\{\boldsymbol{R}_n\}\hat{\boldsymbol{H}}_{nm}\psi_{\text{eq}}(\{\boldsymbol{R}_n\}) = \frac{1}{8\pi\eta_s}\left\langle \frac{1}{\boldsymbol{R}_{nm}}\right\rangle_{\text{eq}} \frac{4}{3}\boldsymbol{1} = h(n-m)\,\boldsymbol{1}$$
$$\text{for} \quad n \neq m \quad \text{with} \quad h(k) = \frac{1}{\sqrt{6\pi^3}\,k^{1/2} b\,\eta_s}. \tag{46}$$

This so-called preaveraging approximation linearizes the Langevin equation. Furthermore, using the same normal coordinates as in the Rouse model, it can be shown that the transform of $h(n-m)$ is diagonal in the mode number:

$$\begin{aligned}
h_{pq} &= \frac{1}{N^2}\int_0^N dn \int_0^N dm \cos\left(\frac{p\pi n}{N}\right)\cos\left(\frac{q\pi m}{N}\right) h(n-m) = \frac{1}{N^2}\int_0^N dn \int_{-n}^{N-n} dk \cos\left(\frac{p\pi n}{N}\right)\cos\left(\frac{q\pi [k+n]}{N}\right) h(k) \\
&= \frac{1}{N^2}\int_0^N dn \left[\cos\left(\frac{p\pi n}{N}\right)\cos\left(\frac{q\pi n}{N}\right)\int_{-n}^{N-n} dk \cos\left(\frac{q\pi k}{N}\right) h(k) - \cos\left(\frac{p\pi n}{N}\right)\sin\left(\frac{q\pi n}{N}\right)\underbrace{\int_{-n}^{N-n} dk \sin\left(\frac{q\pi k}{N}\right) h(k)}_{=0}\right] \\
&\approx \frac{1}{N^2}\int_0^N dn \cos\left(\frac{p\pi n}{N}\right)\cos\left(\frac{q\pi n}{N}\right)\int_{-\infty}^{\infty} dk \cos\left(\frac{q\pi k}{N}\right) h(m) = \frac{1}{N^2}\int_0^N dn \cos\left(\frac{p\pi n}{N}\right)\cos\left(\frac{q\pi n}{N}\right)\frac{\sqrt{N}}{\sqrt{3\pi^3 q}\,\eta_s b} \\
&\approx \frac{\delta_{pq}}{\sqrt{12\pi^3 pNb^2}\,\eta_s} \approx \frac{0.0518}{\eta_s N^{1/2} b}\frac{1}{p^{1/2}}\delta_{pq} \quad \text{for} \quad p,q \neq 0, \\
h_{00} &= \frac{1}{N^2}\int_0^N dn \int_0^N dm\, h(n-m) = \frac{8}{\sqrt{54\pi^3 Nb^2}\,\eta_s} \approx \frac{0.196}{\eta_s N^{1/2} b}.
\end{aligned} \tag{47}$$

Thus, the differential equations for the normal coordinates are the same uncoupled ones as in the Rouse model with

$$\gamma_p = \frac{1}{h_{pp}} \quad \text{for} \quad p = 0,1,2,\ldots\ . \tag{48}$$

For the diffusion coefficient and the relaxation times and amplitudes, we obtain

$$\begin{aligned}
D &= \frac{k_B T}{\gamma_0} \approx 0.0798\frac{k_B T}{\eta_s R_g}, \\
\tau_1 &\approx 0.398\frac{\eta_s}{k_B T}\left(Nb^2\right)^{3/2} \approx 5.849\frac{\eta_s R_g^3}{k_B T}, \quad \tau_p = \frac{\tau_1}{p^{3/2}}, \\
\left\langle \boldsymbol{X}_p^2 \right\rangle &= \frac{3k_B T}{k_p} = \frac{Nb^2}{2\pi^2 p^2} \approx 0.0507\frac{Nb^2}{p^2} \approx 0.304\frac{R_g^2}{p^2}.
\end{aligned} \tag{49}$$

It is worth noting that the relaxation times are 2-fold larger than in the original publication [20], but in good agreement with more recent, corrected values [8, 21, 22] after employing the correction factor resulting from perturbation calculations [1]. Using Equation (37) one can show that the overall amplitude of segment fluctuations equals the radius of gyration:

$$\left\langle \boldsymbol{R}'^2_{\text{seg}}(0) \right\rangle = 2\sum_{p=1}^{\infty}\left\langle \boldsymbol{X}_p^2(0) \right\rangle = R_g^2\,, \tag{50}$$

confirming the more qualitative estimation, Equation (9), made before.

1.13. Zimm model for a swollen linear chain

For a swollen chain under good-solvent conditions, the excluded volume interaction must be taken into account. Instead of replacing the Oseen tensor by the Rotne-Prager tensor [23-27], we employ the Oseen tensor but use a non-Gaussian distance distribution, Equation (17), for the preaveraging approximation, which we consider more appropriate for a considerably flexible and soft polymer like the chromatin fiber:

$$\left\langle \hat{\boldsymbol{H}}_{nm} \right\rangle_{\text{eq}} = \frac{1}{6\pi\eta_{\text{s}}} \left\langle \frac{1}{\boldsymbol{R}_{nm}} \right\rangle_{\text{eq}} \boldsymbol{1} = h(n-m)\,\boldsymbol{1} \quad \text{for} \quad n \neq m \quad \text{with} \quad h(k) \approx \frac{0.0680}{\eta_s k^{3/5} b}. \tag{51}$$

Again, the Langevin equations are linearized and diagonalized, and the difference to the ideal case is covered by modified parameters k_p, γ_p – the linearization approximation. In full analogy to the case of the ideal chain, the hydrodynamic interaction matrix can be derived:

$$\begin{aligned} h_{pq} &\approx \frac{0.0772}{\eta_s N^{3/5} b} \frac{1}{p^{2/5}} \delta_{pq} \quad \text{for} \quad p, q \neq 0\,, \\ h_{00} &\approx \frac{0.243}{\eta_s N^{3/5} b}. \end{aligned} \tag{52}$$

Now, the generalized spring constant can be determined using the equipartition theorem stating that each mode carries an energy of

$$\frac{k_p}{2} \left\langle \boldsymbol{X}_p^2 \right\rangle = \frac{3}{2} k_B T, \tag{53}$$

and using Equation S(35), integration by parts and the relation

$$\frac{\partial \boldsymbol{R}_n}{\partial n} \frac{\partial \boldsymbol{R}_n}{\partial n} = -\frac{1}{2} \frac{\partial^2}{\partial n\, \partial n} (\boldsymbol{R}_n - \boldsymbol{R}_m)^2 = -\frac{1}{2} \frac{\partial^2}{\partial n\, \partial n} |n-m|^{2\nu} b^2 = \nu(2\nu - 1)|n-m|^{2\nu-2} b^2 \tag{54}$$

the generalized spring constant reads

$$\begin{aligned} k_p &= \left(\frac{\left\langle \boldsymbol{X}_p^2 \right\rangle}{3 k_B T} \right)^{-1} = \left[-\frac{1}{6\pi^2 k_B T p^2} \int_0^N dn \int_0^N dm \sin\!\left(\frac{p\pi n}{N}\right) \sin\!\left(\frac{p\pi m}{N}\right) \frac{\partial^2}{\partial n\, \partial m} \left\langle (\boldsymbol{R}_n - \boldsymbol{R}_m)^2 \right\rangle_{\text{eq}} \right]^{-1} \\ &\approx 71.1 \frac{k_B T}{N^{2\nu} b^2} p^{2\nu+1} \to 63.0 \frac{k_B T}{N^{2\nu} b^2} p^{2\nu+1}. \end{aligned} \tag{55}$$

In the last step, the numerical factor was adapted to fulfill for the overal amplitude of the segment fluctuations

$$\left\langle \boldsymbol{R}'^{2}_{\text{seg}}(0) \right\rangle = 2 \sum_{p=1}^{\infty} \left\langle \boldsymbol{X}_p^2(0) \right\rangle = R_g^2\,. \tag{56}$$

For the diffusion coefficient and the relaxation times and amplitudes, we obtain

$$
\begin{aligned}
&D \approx 0.0288\frac{k_B T}{\eta_s R_g},\\
&\tau_1 \approx 0.206\frac{\eta_s}{k_B T}\left(N^{3/5}b\right)^3 \approx 3.845\frac{\eta_s R_g^3}{k_B T}, \quad \tau_p = \frac{\tau_1}{p^{9/5}},\\
&\left\langle \boldsymbol{X}_p^2 \right\rangle \approx 0.0477\frac{\left(N^{3/5}b\right)^2}{p^{11/5}} \approx 0.335\frac{R_g^2}{p^{11/5}}.
\end{aligned}
\tag{57}
$$

1.14. Zimm model for a globular linear chain

For a globular chain under poor-solvent conditions, again the preaveraging approximation is employed, however, with a more compact Gaussian segment distance distribution, Equation (16), which we consider appropriate for the globular configuration of a considerably flexible and soft polymer like the chromatin fiber:

$$
\left\langle \hat{\boldsymbol{H}}_{nm} \right\rangle_{\text{eq}} = \frac{1}{6\pi\eta_s}\left\langle \frac{1}{\boldsymbol{R}_{nm}} \right\rangle_{\text{eq}} \boldsymbol{1} = h(n-m)\boldsymbol{1} \quad \text{for} \quad n \neq m \quad \text{with} \quad h(k) = \frac{1}{\sqrt{6\pi^3}\,k^{1/3} b\,\eta_s}. \tag{58}
$$

Again, the Langevin equations are linearized and diagonalized, and the difference to the ideal case is covered by modified parameters k_p, γ_p – the linearization approximation. In full analogy to the case of the ideal chain, the hydrodynamic interaction matrix can be derived:

$$
\begin{aligned}
&h_{pq} \approx \frac{\Gamma(2/3)\,\delta_{pq}}{\sqrt{24\pi^{13/3}N^{2/3}b^2 p^{4/3}}\,\eta_s} \approx \frac{0.0231}{\eta_s N^{1/3} b}\frac{1}{p^{2/3}}\delta_{pq} \quad \text{for} \quad p,q \neq 0,\\
&h_{00} = \frac{9}{\sqrt{150\pi^3 q N^{2/3} b^2}\,\eta_s} \approx \frac{0.132}{\eta_s N^{1/3} b}.
\end{aligned}
\tag{59}
$$

We could show, see Equation (55), that the generalized spring constant obeys

$$
k_p \propto \frac{k_B T}{N^{2\nu} b^2} p^{2\nu+1}, \tag{60}
$$

and the proportionality factor is adjusted such that for $\nu = 1/3$,

$$
\left\langle \boldsymbol{R}'^2_{\text{seg}}(0) \right\rangle = 2\sum_{p=1}^{\infty}\left\langle \boldsymbol{X}_p^2(0) \right\rangle = 6k_B T\sum_{p=1}^{\infty} k_p^{-1} = R_g^2 \tag{61}
$$

is fulfilled. This yields the diffusion coefficient and the relaxation times and amplitudes:

$$
\begin{aligned}
&D \approx 0.0626\frac{k_B T}{\eta_s R_g},\\
&\tau_1 \approx 0.763\frac{\eta_s}{k_B T} N b^3 \approx 7.151\frac{\eta_s R_g^3}{k_B T}, \quad \tau_p = \frac{\tau_1}{p},\\
&\left\langle \boldsymbol{X}_p^2 \right\rangle \approx 0.0530\frac{N^{2/3}b^2}{p^{5/3}} \approx 0.236\frac{R_g^2}{p^{5/3}}.
\end{aligned}
\tag{62}
$$

1.15. Zimm model for an ideal circular chain

In order to obtain the dynamic parameters of an ideal circular chain under theta-solvent conditions, the concept of the Rouse model for circular chains and the preaveraging and linearization approximations of the Zimm model for ideal linear chains can be combined [19, 28, 29]. We assume for the segment distance distribution (for both theta- and good-solvent conditions)

$$\psi_{nm}(r)=\begin{cases}\left(\dfrac{3}{2\pi\mu b^2}\right)^{3/2}\exp\left(-\dfrac{r^2}{\mu b^2}\right) & \nu=\dfrac{1}{2},\\ \left(\dfrac{3}{2\pi\mu^{2/3} b^2}\right)^{3/2}\exp\left(-\dfrac{r^2}{\mu^{2/3} b^2}\right) & \nu=\dfrac{1}{3},\end{cases}\quad\text{with}$$

$$\mu(m,n,N)=\frac{|m-n|(N-m+1)}{N},\quad 0\le m,n\le N. \tag{63}$$

This is used for the preaveraging approximation in analogy to Equation (46)

$$h(k)=\frac{1}{\sqrt{6\pi^3}\eta_s b}\frac{\sqrt{N}}{\sqrt{|k|(N-|k|)}}. \tag{64}$$

Again, the Langevin equation is linearized and diagonalized: in full analogy to the case of the ideal chain, the hydrodynamic interaction matrix reads

$$\begin{aligned}h_{pq}&=\frac{1}{N^2}\int_0^N dn\int_0^N dm\cos\left(\frac{2p\pi n}{N}\right)\cos\left(\frac{2q\pi m}{N}\right)h(n-m)=\frac{1}{N^2}\int_0^N dn\cos\left(\frac{2p\pi n}{N}\right)\int_{-n}^{N-n}dk\cos\left(\frac{q\pi[k+n]}{N}\right)h(k)\\ &=\frac{1}{N^2}\int_0^N dn\left[\cos\left(\frac{2p\pi n}{N}\right)\cos\left(\frac{2q\pi n}{N}\right)\underbrace{\int_{-n}^{N-n}dk\cos\left(\frac{2q\pi k}{N}\right)h(k)}_{=\sqrt{N}J_0(\pi q)\cos(\pi q)/\sqrt{6\pi}\eta_s b}-\cos\left(\frac{2p\pi n}{N}\right)\sin\left(\frac{2q\pi n}{N}\right)\underbrace{\int_{-n}^{N-n}dk\sin\left(\frac{2q\pi k}{N}\right)h(k)}_{=0}\right]\\ &=\frac{J_0(\pi q)\cos(\pi q)}{\sqrt{24\pi N b^2}\eta_s}\delta_{pq}\approx\frac{0.035}{\eta_s N^{1/2} b}\frac{1}{q^{1/2}}\delta_{pq}\quad\text{for}\quad p,q\neq 0,\\ h_{00}&=\frac{1}{N^2}\int_0^N dn\int_0^N dm\,h(n-m)=\frac{1}{\sqrt{6\pi N b^2}\eta_s}\approx\frac{0.230}{\eta_s N^{1/2} b}.\end{aligned} \tag{65}$$

Including the same corrections from perturbation calculations as for the linear chain, see Equation (49), we obtain for the diffusion coefficient and the relaxation times and amplitudes

$$\begin{aligned}D&=\frac{k_BT}{\gamma_0}=k_BT\,h_{00}\approx 0.0665\frac{k_BT}{\eta_s R_g},\\ \tau_1&\approx 0.147\frac{\eta_s}{k_BT}\left(Nb^2\right)^{3/2}\approx 6.111\frac{\eta_s R_g^3}{k_BT},\quad \tau_p=\frac{\tau_1}{p^{3/2}},\\ \left\langle \boldsymbol{X}_p^2\right\rangle&=\frac{3k_BT}{k_p}\approx 0.0127\frac{Nb^2}{p^2}\approx 0.152\frac{R_g^2}{p^2}.\end{aligned} \tag{66}$$

Just as for the Rouse model for a circular chain, the Zimm model also fulfills

$$\left\langle \boldsymbol{R}'^{2}_{\mathrm{seg}}(0)\right\rangle = 2\sum_{p=1}^{\infty}\left\langle \boldsymbol{X}_p^2(0)\right\rangle = \frac{1}{2}R_g^2 . \tag{67}$$

1.16. Zimm model for a swollen circular chain

For good-solvent conditions, we employ the approaches used for a swollen linear chain and an ideal circular chain. The segment distance distribution is described in analogy to Equation (17) and (63) as

$$\begin{aligned} \psi_{nm}(r) &\approx \frac{0.29}{\left(\mu^{3/5}b\right)^{3.28}}\, r^{0.28}\exp\left[-1.22\left(\frac{r}{\mu^{3/5}b}\right)^{5/2}\right], \\ \mu(m,n,N) &= \frac{|m-n|\left(N-m+1\right)}{N}, \quad 0 \le m,n \le N. \end{aligned} \tag{68}$$

This yields after the preaveraging approximation for the diagonal hydrodynamic interaction matrix

$$\begin{aligned} h_{pq} &\approx \frac{0.0568}{\eta_s N^{3/5} b}\frac{1}{q^{2/5}}\delta_{pq} \quad \text{for} \quad p,q \neq 0, \\ h_{00} &\approx \frac{0.287}{\eta_s N^{3/5} b}. \end{aligned} \tag{69}$$

Again, the generalized spring constant and the mode amplitudes can be calculated using the equipartition theorem stating that each mode carries an energy of

$$\frac{k_p}{2}\left\langle \boldsymbol{X}_p^2\right\rangle = \frac{3}{2}k_B T, \tag{70}$$

and with the same approach as used for the linear chain, yet replacing $|n-m|$ with $\mu(m,n,N)$ and executing some of the integrations numerically, the diffusion coefficient and the relaxation times and amplitudes read

$$\begin{aligned} D &\approx 0.0830\frac{k_B T}{\eta_s R_g}, \\ \tau_1 &\approx 0.0603\frac{\eta_s}{k_B T}N^{9/5}b^3 \approx 4.114\frac{\eta_s R_g^3}{k_B T}, \quad \tau_p = \frac{\tau_1}{p^{17/20}}, \\ \left\langle \boldsymbol{X}_p^2\right\rangle &\approx 0.0103\frac{\left(N^{3/5}b\right)^2}{p^{9/4}} \approx 0.172\frac{R_g^2}{p^{9/4}}. \end{aligned} \tag{71}$$

Again, Equation (67) is fulfilled.

1.17. Zimm model for branched polymers

As shown in the previous sections and concluded in previous publications [13, 20, 30-32], the dynamic properties of a polymer such as the diffusion coefficient as well as amplitudes and characteristic times of relaxation modes are mostly determined by the radius of gyration, which describes the effective volume occupied by the molecule, in only weak dependence on the topology and the compaction of the molecule. This could also be confirmed for star-like branched polymers whose relaxation is akin to linear molecules [33].

Zimm and Kilb [13] showed that for a given number N of segments of a non-draining polymer under theta-solvent conditions, the relaxation time depends on the branching ratio as $\tau_1 \propto f^{-3/2}$. This is in good agreement with our findings: combining Equation (21) and (49) yields $\tau_1 \propto R_g^3 \propto (3f-2)^{3/2} / f^3 \rightarrow f^{-3/2}$ for larger *f*. Grest *et al.* [31] found for a large branching ratio *f* under good-solvent conditions and $\tau_1 \propto f^{-1.7}$, which is again in quite good agreement with our findings: Equation (23) and (57) yield $\tau_1 \propto R_g^3 \propto (3.59f-2.59)^{1.5} / f^{3.3} \rightarrow f^{-1.8}$ for larger *f*. Therefore we conjecture that Equation (49), (57), (66) and (71) apply to both linear/circular and branched star-/rosette-like polymers, and the branching ratio dependence is covered by the respective dependencies of the radii of gyration, Equation (21)–(24), for both small and large *f*.

1.18. Scaling considerations to distinguish semi-dilute from dilute and concentrated conditions

All considerations and results above were obtained assuming a dilute system, i.e., only a single chain molecule is regarded. However, at higher concentrations, this assumption is not valid and separate chains become entangled. The application of scaling laws to semi-dilute polymer solutions showed that all interactions between chain segments are effectively screened above a characteristic distance, the correlation length [8, 9]. If this is smaller than the characteristic length of the molecules, e.g. the mean squared end-to-end distance, each molecule can be described as a chain of topologically and dynamically independent ‘blobs’. Their internal properties are identical to those of a single independent chain molecule, including hydrodynamic and excluded-volume interactions so that their dynamics can be described with the Rouse-Zimm formalism [23, 34-36]. The screening on length scales beyond the correlation length and corresonding times results in a purely Rouse-like behaviour of the chain of blobs on a significantly slower time scale. The transition from dilute to semi-dilute conditions sets in when the volume that a single independent chain would occupy becomes larger than the actually available volume or, in other words, when the actual global segment or monomer concentration c is higher than it would be inside a single independent chain, c^*. Using Equation (10) for a chain consisting of N Kuhn segments the critical concentration threshold is:

$$c^* = \frac{N}{3.03R_g^3}. \tag{72}$$

The number of monomers per blob [8] is given as:

$$N^* = N\left(\frac{c^*}{c}\right)^{5/4}. \tag{73}$$

When assuming a nucleosome concentration of 140 µM [37, 38], a range of 35–80 nm for the chromatin persistence length and 1.1–5.5 nucleosmes/11 nm for the mass density, we obtain a range of 1050–12000 chromatin segments/µm^3, well above the threshold of 13–46 segments/µm^3 critical concentration. On the other hand, the nuclear volume fraction occupied by chromatin is 10–20% [38, 39], i.e., well below the threshold for a concentrated polymer solution [1]. Therefore, the concentration regime of chromatin in mammalian interphase nuclei is semi-dilute, and blob formation is likely to occur. In addition to this generic formation of independent domains, further physical and topological constraints may contribute like the formation of loops, loop clusters or globules. Independent of the actual nature of the domains, the treatment of chromatin dynamics using the Rouse-Zimm formalism as carried out above is appropriate.

1.19. Adiabatic accessibilty of a fluctuating polymer for diffusive tracer molecules

The volume effectively occupied by a polymer molecule is characterized by its radius of gyration and Equation (10). The net volume of the polymer chain V_c, however, is determined by its contour length L and its diameter d. A repulsive interaction between the polymer and a tracer molecule of radius R_h will increase the volume, from which the tracer is excluded, such that the effective diameter of the polymer chain is increased by $2R_h$ [40]. The effective chain volume is thus

$$V_c = \frac{\pi}{4}\left(d + 2R_h\right)^2 L\,. \tag{74}$$

From a comparison of the effectively occupied volume, Equation (10), and the effective chain volume, Equation (74), the accessibility can be defined as

$$1 - \frac{V_c}{V} \approx 1 - \operatorname{erf}\left(\frac{V_c}{V}\right). \tag{75}$$

The dynamic properties of the polymer result in a fluctuating occupied volume. The time scale of these fluctuations is defined by the relaxation kinetics of the polymer as described above. When this is slower than the diffusional mobility of the tracer molecules, these fill the available volume, the complement to the effective chain volume, adiabatically. The diffusional accessibility of the polymer molecule is thus defined by the maximum rather than the mean occupied volume, i.e., in Equation (75) we replace V with $V + \delta V$, see Equation (11), and we get the dynamic accessibility

$$1 - \frac{V_c}{V + \delta V} \approx 1 - \operatorname{erf}\left(\frac{V_c}{V + \delta V}\right), \tag{76}$$

which is higher than the static accessibilty, Equation (75).

Fluorescence correlation spectroscopy of polymer relaxation

Photon correlation techniques, especially dynamic light scattering, are widely used approaches to study polymer dynamics [3, 21]. More recently, in a number of studies intramolecular dynamics have been investigated with FCS [41-48]. Especially the uncoupling of the center-of-mass (CM) diffusion from the higher order relaxation modes by trapping or tracking [45, 49] provided detailed insight into the internal dynamics, requiring a series representation of relaxation modes for a comprehensive understanding [45, 46, 48]. In summary, as shown for double-stranded DNA, the mean-squared displacement of polymer segments can be described as confined diffusion relative to the CM, the hydrodynamic interaction must be taken into account and molecules with a sufficiently large ratio of contour to persistence length, i.e., ‘soft’ polymers, show Zimm relaxation behaviour.

1.20. Diffusion in a harmonic potential as seen with FCS

The relaxation processes of a polymer result in local concentration fluctuations of polymer segments even for the case that the zero order relaxation, the center of mass diffusion, is negligible. Since every relaxation mode is independent of the others and has an exponentially decaying position correlation function [1], it can be represented by a diffusion process in a harmonic potential, which is an Ornstein-Uhlenbeck process, the simplest example of a stationary Markov process with a Gaussian probability distribution at all times [50].

Let us assume Brownian motion in a harmonic potential

$$U(\boldsymbol{r}) = \frac{1}{2}(\boldsymbol{r}-\boldsymbol{r}_c)\hat{\boldsymbol{K}}(\boldsymbol{r}-\boldsymbol{r}_c) \tag{77}$$

centered at $\boldsymbol{r}_c$. The Langevin equation is

$$m\frac{d^2\boldsymbol{r}(t)}{dt^2} = -\nabla U(\boldsymbol{r}) - \hat{\boldsymbol{\Gamma}}\frac{d\boldsymbol{r}(t)}{dt} + \boldsymbol{F}(t) = -\hat{\boldsymbol{K}}[\boldsymbol{r}(t)-\boldsymbol{r}_c] - \hat{\boldsymbol{\Gamma}}\frac{d\boldsymbol{r}(t)}{dt} + \boldsymbol{F}(t) \tag{78}$$

where the random force generates the fluctuations. Assuming isotropy, i.e., the spring constant and friction matrix become scalar, and overcritical damping, i.e., the inertia term can be neglected, the Langevin equation simplifies to

$$\gamma\boldsymbol{v}(t) = \gamma\frac{d\boldsymbol{r}(t)}{dt} = k[\boldsymbol{r}(t)-\boldsymbol{r}_c] + \boldsymbol{F}(t). \tag{79}$$

The resulting additional flux is represented by a corresponding term in the Smoluchowski or Fokker-Planck equation

$$\frac{\partial c(\boldsymbol{r},t)}{\partial t} = \frac{k}{\gamma}\nabla[(\boldsymbol{r}-\boldsymbol{r}_c)c(\boldsymbol{r},t)] + D_0\nabla^2 c(\boldsymbol{r},t). \tag{80}$$

The solution in 3D under the assumption that the diffusing particle is at time zero at a position $\boldsymbol{r}_1$, $P_D(\boldsymbol{r}_2,\tau|\boldsymbol{r}_1,0) = \delta(\boldsymbol{r}_2-\boldsymbol{r}_1)$, turns out to be

$$P_D(\boldsymbol{r}_2,\tau|\boldsymbol{r}_1,0) = \left(\frac{k}{2\pi D_0\gamma[1-\exp(-2k\tau/\gamma)]}\right)^{3/2}\exp\left[-\frac{k}{2D_0\gamma}\frac{|(\boldsymbol{r}_2-\boldsymbol{r}_c)-(\boldsymbol{r}_1-\boldsymbol{r}_c)\exp(-k\tau/\gamma)|^2}{1-\exp(-2k\tau/\gamma)}\right] \tag{81}$$

with the stationary distribution

$$W_D(\boldsymbol{r}) = \lim_{\tau\to\infty} P_D(\boldsymbol{r},\tau|\boldsymbol{r}_1,0) = \left(\frac{k}{2\pi D_0\gamma}\right)^{3/2}\exp\left[-\frac{k}{2D_0\gamma}(\boldsymbol{r}_2-\boldsymbol{r}_c)^2\right]. \tag{82}$$

The position autocorrelation function of such a diffusing particle decays with $\exp(-\tau/\tau_{\text{relax}})$, $\tau_{\text{relax}} = \gamma/k$ as expected.

The application of this Greens function to the FCS theory and subsequently averaging over all positions relative to the center of the FCS focus results in the autocorrelation function

$$G(\tau) = \frac{1}{N}\left[\left(1+\frac{1-\exp[-\tau/\tau_{\text{relax}}]}{\upsilon}\right)^{-1}\left(1+\frac{1-\exp[-\tau/\tau_{\text{relax}}]}{\kappa^2\upsilon}\right)^{-1/2} - \left(1+\frac{1}{\upsilon}\right)^{-1}\left(1+\frac{1}{\kappa^2\upsilon}\right)^{-1/2}\right] \tag{83}$$

where N is the number of molecules in the focus, $\upsilon = \tau_D / \tau_{\text{relax}}$ the ratio of diffusion correlation time and relaxation time and $\kappa = z_0 / w_0$ the structure parameter of the focal volume, i.e., the ratio of axial and lateral focal radii [51]. For an infinitely weak potential, the correlation function for free diffusion is recovered.

When disregarding the constant term in Equation (83), an estimation of the MSD of the segments can be extracted from the correlation function [47] by comparing it to

$$G(\tau) \approx \frac{1}{N}\left(1+\frac{2\left\langle\left[\boldsymbol{R}'_{\text{seg}}(t)-\boldsymbol{R}'_{\text{seg}}(0)\right]^2\right\rangle}{3w_0^2}\right)^{-1}\left(1+\frac{2\left\langle\left[\boldsymbol{R}'_{\text{seg}}(t)-\boldsymbol{R}'_{\text{seg}}(0)\right]^2\right\rangle}{3\kappa^2 w_0^2}\right)^{-1/2}. \tag{84}$$

1.21. Zimm relaxation modes in FCS

The polymer relaxation process can be described as a weighted sum of diffusive components, Equation (37), within the framework of the Zimm model for the different conditions and topologies. The weighting is based on the mode number dependence of the mode amplitudes $\left\langle \boldsymbol{X}_p^2 \right\rangle$. The only difference made between single chains (circular or linear) and branched molecules (stars or rosettes) is the dependence of the radius of gyration on the branching ratio. The relaxation time τ_1 from a fit of the model function to experimental data yields the radius of gyration according to Equation (49), (57), (62), (66) or (71), provided that the nuclear solvent viscosity is determined independently. With the knowlegde of the Kuhn segment length (through the persistence length), a branching ratio-dependent contour length can be determined. In the context of the 30 nm chromatin fiber, the genomic content is obtained.

1.22. Measuring the nucleoplasmic viscosity

The effective viscosity of the nucleoplasm affects chromatin segment diffusion. It is scale-dependent and varies between a small value for short distances as sensed by rotational diffusion and the value accessible with FCS when comparing apparent diffusion coefficients *in vivo* and in water on the scale of the observation volume, i.e., the focal volume of the confocal microscope [52, 53]. The corresponding intracellular apparent diffusion coefficient on different scales can be described using the concept of anomalous diffusion, which yields for the mean squared displacement

$$\left\langle\left[\boldsymbol{r}(t)-\boldsymbol{r}(0)\right]^2\right\rangle = \Gamma t^{\alpha} \quad \text{or} \quad t = \left\langle\left[\boldsymbol{r}(t)-\boldsymbol{r}(0)\right]^2\right\rangle^{-1/\alpha}\Gamma^{1/\alpha} \quad \text{for} \quad 0<\alpha<1 \tag{85}$$

parametrized by the transport coefficient Γ and the anomaly parameter α. For free diffusion e.g. in solution they become $\alpha = 1$ and $\Gamma = 6D$. The FCS autocorrelation function of fluorescent molecules inside living cells with the known model function for anomalous diffusion reads

$$G(\tau) = \frac{1}{N}\left[1-\Theta_T+\Theta_T \exp\left(\frac{\tau}{\tau_T}\right)\right]\left[1+\left(\frac{\tau}{\tau_D}\right)^{\alpha}\right]^{-1}\left[1+\frac{1}{\kappa^2}\left(\frac{\tau}{\tau_D}\right)^{\alpha}\right]^{-1} \tag{86}$$

where N is the mean number of molecules in the focal volume, Θ_T the fraction of molecules in a non-fluorescent state, τ_T their dwell time in this state, $\tau_D = w_0^2 / 4D$ the diffusional dwell time of the molecules having an apparent diffusion coefficient D inside the focal volume of a lateral diameter w_0

and a structure parameter κ. Fitting FCS data of fluorescent molecules acquired both inside cell nuclei and in solution with this model function yields diffusion times whose ratio determines the relative viscosity of the nucleoplasm compared to water on the length scale w_0 according to $\eta_{\text{rel}}(w_0) = \tau_{D,\text{cell}} / \tau_{D,\text{solution}}$. Using the mean squared displacement, Equation (85), and the measured intracellular anomaly parameter, the relative viscosity can be calculated for any length scale

$$\eta_{\text{rel}}(x) = \left(\frac{x}{w_0}\right)^{2/\alpha-2} \eta_{\text{rel}}(w_0). \tag{87}$$

In order to determine the effective nucleoplasmic viscosity this is averaged over the whole range $0 \le x \le w_0$:

$$\langle \eta_{\text{rel}} \rangle = \frac{1}{w_0} \int_0^{w_0} dx\, \eta_{\text{rel}}(x) = \eta_{\text{rel}}(w_0) \cdot \frac{\alpha}{2-\alpha} = \frac{\tau_{D,\text{cell}}}{\tau_{D,\text{solution}}} \cdot \frac{\alpha}{2-\alpha}. \tag{88}$$

Photobleaching experiments of chromatin-associated proteins

In order to estimate binding properties of a nuclear protein, we have combined fluorescence recovery/redistribution after photobleaching (FRAP) and continuous fluorescence photobleaching (CP) with optimized experimental settings.

1.23. FRAP of a two-dimensional strip

We performed FRAP experiments with reduced numerical aperture und increased pinhole size such that bleaching occurs approximately through the complete depth of the cell nucleus [54]. Moreover, we bleached the fluorescence in a strip-like area that spans the whole nucleus in one direction and is relatively small, of width $2a$, compared to the nuclear elongation in the other direction that we refer to as x-axis. Under these conditions, we can consider the diffusional redistribution of fluorescent molecules as an effectively one-dimensional process. A solution of the diffusion equation or Fick's 2nd law of diffusion for the one-dimensional concentration distribution over time

$$\frac{\partial c(x,t)}{\partial t} = D \nabla^2 c(x,t) \tag{89}$$

under the postbleach start condition with the bleach depth p

$$c(x,0) = c_0 - c_0 p [\Theta(x+a) - \Theta(x-a)] \quad \text{with} \quad 0 \le p \le 1 \tag{90}$$

is found to be

$$c(x,t) = c_0 - c_0 \frac{p}{2} \left[\operatorname{erf}\left(\frac{a+x}{\sqrt{\text{MSD}}}\right) - \operatorname{erf}\left(\frac{a-x}{\sqrt{\text{MSD}}}\right) \right], \quad \text{MSD} = 4Dt + x_0^2 \tag{91}$$

which can be transformed directly into a fluorescence intensity distribution over time for the postbleach image series. An initial broadening of the distribution results from diffusion during bleaching and the approximate Gaussian bleach and detection profile.

To account for diffusion and association to/dissociation from immobilized binding sites with dissociation rate k_off, albeit in an uncoupled manner and in pseudo-first-order approximation, the distribution can be integrated over the bleach region, $-a \le x \le a$. Assuming a rapidly diffusive free fraction, f_free, a slowly diffusive fraction, f_diff, and a transiently bound and immobilized fraction, $1 - f_\mathrm{free} - f_\mathrm{diff}$, this yields the intensity signal over time

$$F(t) = F(t \to \infty)\left(f_\mathrm{free} + f_\mathrm{diff}\left[1 + p\sqrt{\frac{Dt}{\pi a^2}}\left(1 - \exp\left[-\frac{a^2}{Dt}\right]\right) - p\,\mathrm{erf}\left(\sqrt{\frac{a^2}{Dt}}\right)\right] + p[1 - f_\mathrm{free} - f_\mathrm{diff}][1 - \exp(-k_\mathrm{off}t)] \right). \tag{92}$$

Fig. S11, S12 show how to experimentally assess the profile and how the two processes, binding and diffusion, contribute to the molecular redistribution in space and time.

1.24. Continuous photobleaching in the presence of two binding states

As an alternative to the FRAP approach, CP can be used to retrieve interaction properties, especially dissociation rates, for the binding and immobilization of nuclear proteins [55] because the choice of a diffraction-limited bleaching and observation volume in combination with sub-millisecond time resolution allows to decouple diffusion and binding. The FRAP analysis showed that the mobility behaviour can neither be described by a simple diffusion model nor by a simple reaction model. Moreover, the apparent diffusion coefficient obtained from FRAP using a combined diffusion and reaction model, Equation (92), is significantly smaller than measured with FCS. Therefore, we extend the established CP model function for a single association/dissociation step to two such steps, resulting in the modified model function for two bound fractions $f_\mathrm{bound,1}$, $f_\mathrm{bound,2}$ with small dissociation rates compared to the focal bleaching rate, i.e., $k_\mathrm{off,1}, k_\mathrm{off,2} \le \alpha$:

$$\begin{aligned} F(t) = {} & F(0) f_\mathrm{bound,1}\left(\frac{1}{1 + \alpha t/2 + \alpha^2 t^2/6} - \frac{12 k_\mathrm{off,1}/\alpha}{5 + 14 k_\mathrm{off,1}/\alpha}\frac{1}{1 + 3\alpha t/7}\right)\exp(-k_\mathrm{off,1}t) \\ & + F(0) f_\mathrm{bound,2}\left(\frac{1}{1 + \alpha t/2 + \alpha^2 t^2/6} - \frac{12 k_\mathrm{off,2}/\alpha}{5 + 14 k_\mathrm{off,2}/\alpha}\frac{1}{1 + 3\alpha t/7}\right)\exp(-k_\mathrm{off,2}t) \\ & + F(0)\left(f_\mathrm{bound,1}\frac{12 k_\mathrm{off,1}/\alpha}{5 + 14 k_\mathrm{off,1}/\alpha} + f_\mathrm{bound,2}\frac{12 k_\mathrm{off,2}/\alpha}{5 + 14 k_\mathrm{off,2}/\alpha} + f_\mathrm{free}\right)\exp(-\beta t). \end{aligned} \tag{93}$$

The bleaching rate β takes global bleaching of the pool of fluorescent molecules into account. Fitting CP data allows to obtain th two dissociation rates of two binding states of a nuclear chromatin-binding protein.

1.25. Point FRAP in the presence of diffusion and two binding states

We could show previously [56] that point FRAP can be used to study fast diffusion and binding processes. As shown there, one must take diffusion during the photobleaching step into consideration in the presence of a fast diffusive fraction. We did this here and fitted the recovery data with a combination of a coupled diffusion-reaction step and an uncoupled additional binding contribution, i.e., following the same scheme as used for CP. Details are as described in Im *et al.* [56].

1.26. Model for linker histone H1 binding

Based on the FRAP and CP observations and in agreement with other studies [57-61] we suggest the following model for linker histone H1 binding to nucleosomes:

- H1 has two binding sites for DNA,
- it binds loosely and reversibly at the nucleosome entry-exit site at binding site 1 with reate constants k_{on} and $k_{\text{off},1}$,
- the loosely associated complex of H1 and the nucleosome switches eventually and irreversibly to a tightly bound conformation by engaging binding site 2 with rate constant k_{switch},
- H1 dissociates from the tightly bound state with rate constant $k_{\text{off},2}$,
- re-association with chromatin only through the initial pathway.

The corresponding rate equations for the concentrations (and equivalently fractions) of free and bound H1 molecules read

$$\begin{aligned}\frac{\partial c_{\text{free}}}{\partial t} &= -k_{\text{on}} c_{\text{free}} + k_{\text{off},1} c_{\text{bound},1} + k_{\text{off},2} c_{\text{bound},2},\\ \frac{\partial c_{\text{bound},1}}{\partial t} &= k_{\text{on}} c_{\text{free}} - k_{\text{off},1} c_{\text{bound},1} - k_{\text{switch}} c_{\text{bound},1},\\ \frac{\partial c_{\text{bound},2}}{\partial t} &= k_{\text{switch}} c_{\text{bound},1} - k_{\text{off},2} c_{\text{bound},2}.\end{aligned} \tag{94}$$

In steady state equilibrium, i.e., $\partial c_i / \partial t = 0$ for all t, the dissociation rates and the fractions can be obtained from FRAP and CP, and for a complete description of the kinetics, the association and the switch rate can be derived using

$$\begin{aligned}k_{\text{on}} &= \frac{k_{\text{off},1} c_{\text{bound},1} + k_{\text{off},2} c_{\text{bound},2}}{c_{\text{free}}},\\ k_{\text{switch}} &= \frac{k_{\text{off},2} c_{\text{bound},2}}{c_{\text{bound},1}}.\end{aligned} \tag{95}$$

Determination of eu- and heterochromatin nucleosome concentration from images

We used an intensity threshold-based segmentation of the nucleus to determine the mass fractions of eu- and heterochromatin. Fig. S7 shows how we selected the lower intensity threshold for the overall chromatin distribution. The mean intensity of the segmented area served as reference for the mean nucleosome concentration. Next, we set an additional upper threshold such that ~12.5% of the area (and thus volume) were excluded additionally. Selecting for intensities lying between the thresholds provided us with a mean intensity representing the euchromatin concentration. Finally, we used the second threshold as a lower limit for segmentation of heterochromatin such that the corresponding mean intensity represented the heterochromatin concentration. In summary, this yielded a mass fraction of 19.0±1.5% and 81.0±1.5% and a relative nucleosome concentration of 1.56±0.05 and 0.91±0.01 for hetero- and euchromatin, respectively, compared to the mean concentration.

Determination of nuclear solvent viscosity

To determine the effective nuclear solvent viscosity as sensed by the chromatin fiber we had to take into consideration that fiber relaxations take place on all length scales between 0 and a few 100 nm. Since nuclear diffusion usually shows a pronounced deviation from free diffusion, we had to compare nuclear diffusion properties with those in aqueous solution in order to properly estimate the effective nuclear viscosity as described above. Therefore, we injected FITC-labeled 150 kDa dextran molecules with a hydrodynamic radius of ~13 nm [62], i.e., comparable to the dimensions of the chromatin fiber, into nontransfected MCF7 cell nuclei and acquired FCS data. This yielded a cellular diffusion correlation time τ_D = 890±37 µs and an anomaly parameter α = 0.80±0.02. In aqueous solution, we obtained τ_D = 136±6 µs and α = 1. By means of Equation (88), this resulted in an effective viscosity $\langle \eta_{\mathrm{rel}} \rangle = 4.3 \pm 0.3$.

Supplementary Figures

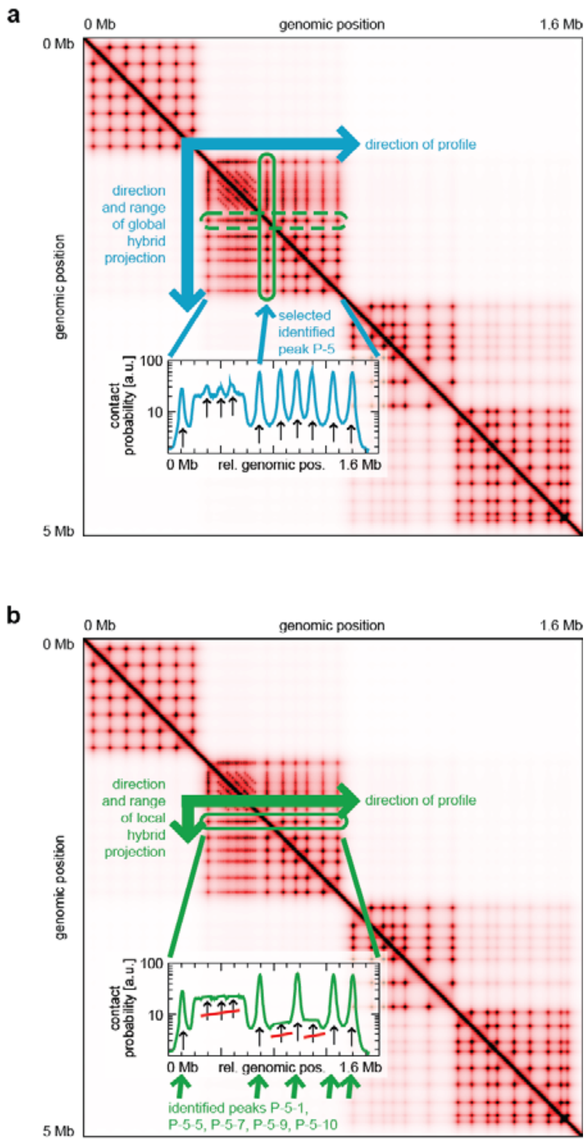

Supplementary Figure S1: Profile-based peak detection for genomic contact probability maps

a First step of peak detection, comprising a global hybrid, i.e., mean of average and maximum, projection over a manually selected domain and curve peak detection as described in Methods. **b** Second step, consisting of successive local mean of average and maximum projections at the peak locations detected in **a**, yielding pairs of interacting genomic sites.

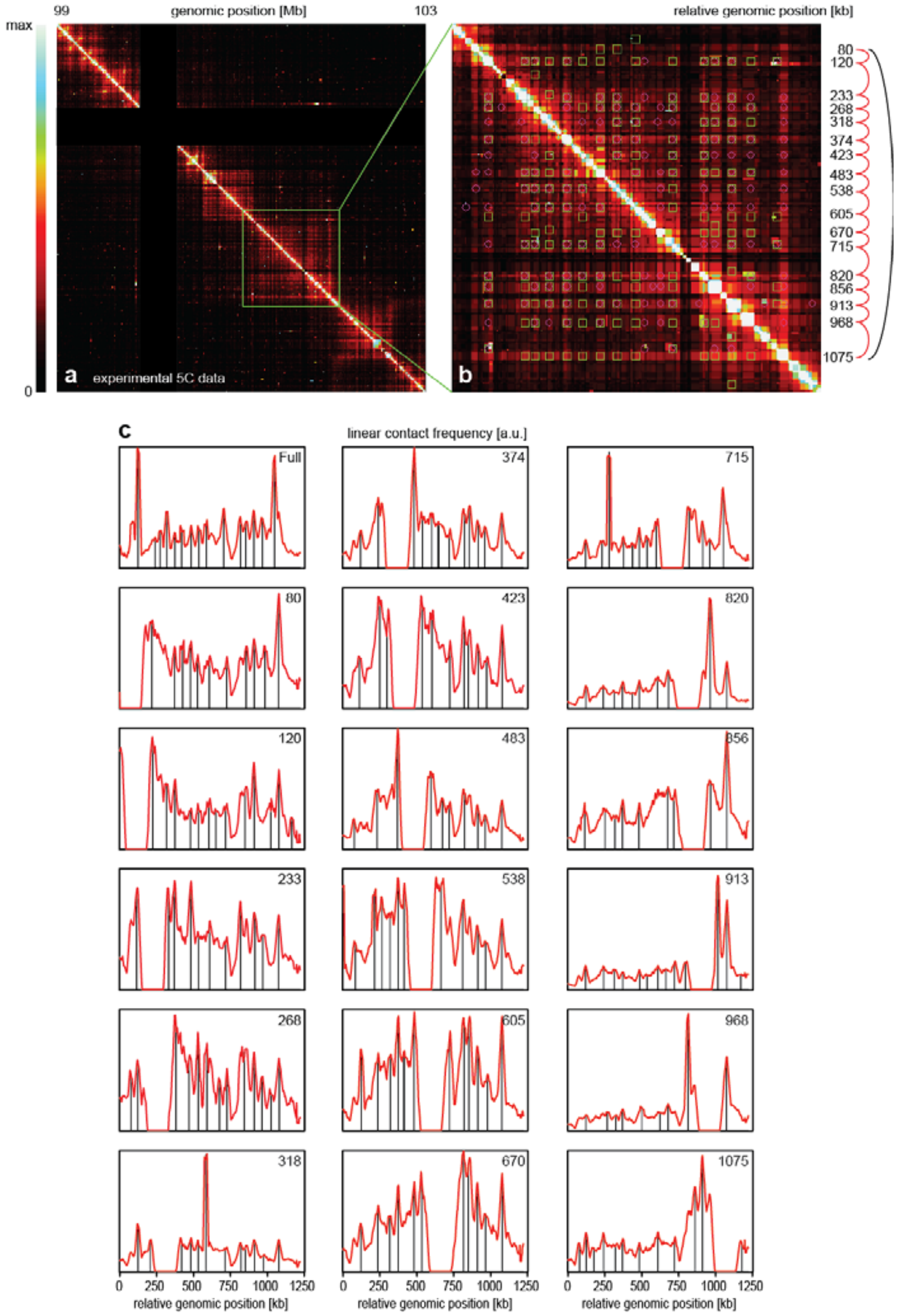

Supplementary Figure S2: Structural analysis of 5C data

a Symmetrized contact probability map extracted from experimental 5C data [63] in linear representation. The highlighted region corresponds to a domain that is shown in more detail in **b**, where the peak analysis described in Fig. S1 yielded local contact probability maxima identified in the one (green squares) and in the other projection direction (pink circles). Peaks were interpreted as sequence of loops between genomic site pairs (red arches) forming the domain (black arch). **c** Local projections (red) around the globally detected peak loci (relative genomic positions in kb given as numbers in panels) and locally detected peak loci (black).

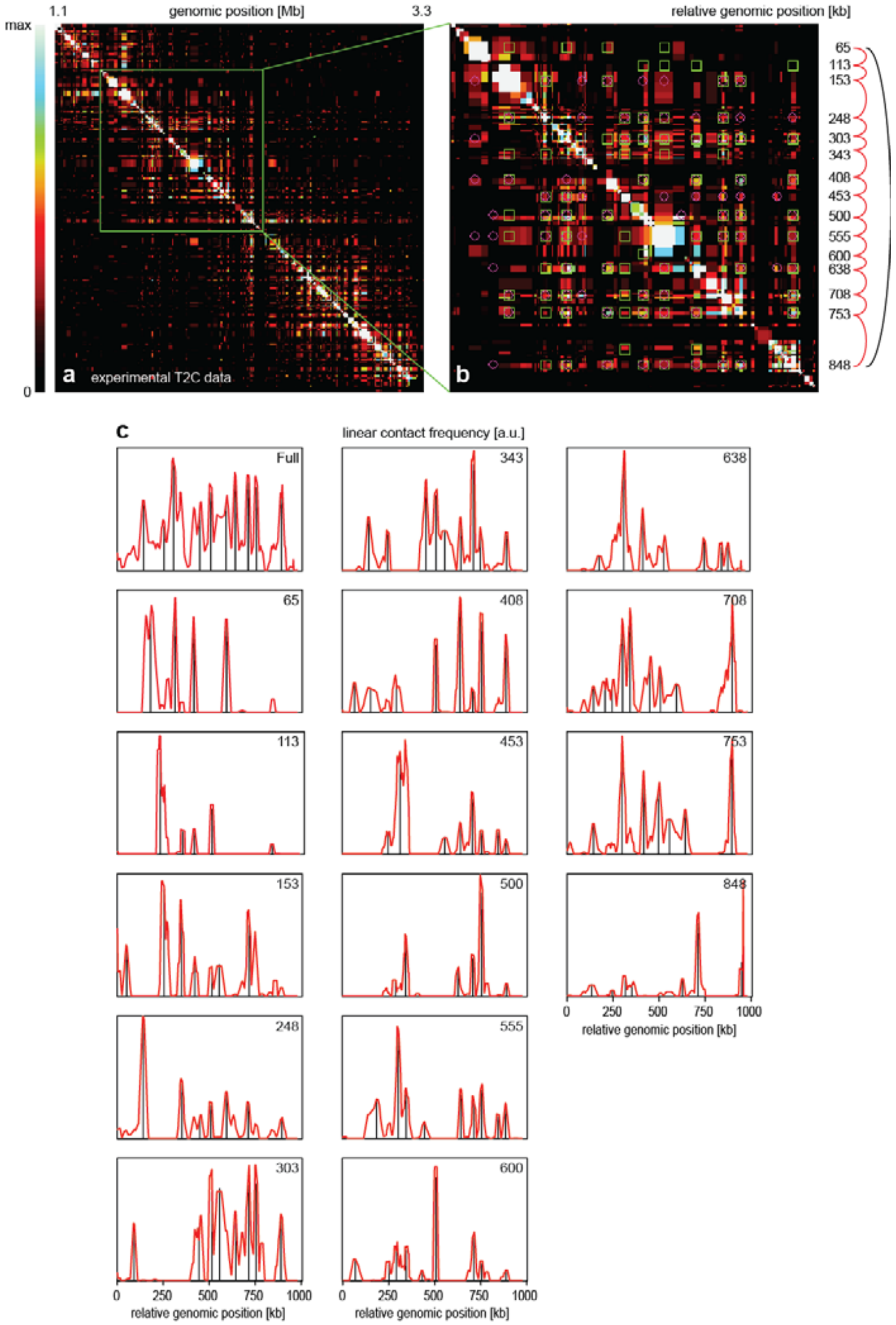

Supplementary Figure S3: Structural analysis of T2C data

a Symmetrized contact probability map extracted from experimental T2C data in linear representation. The highlighted region corresponds to a domain that is shown in more detail in **b**, where the peak analysis described in Fig. S1 yielded local contact probability maxima identified in the one (green squares) and in the other projection direction (pink circles). Peaks were interpreted as sequence of loops between genomic site pairs (red arches) forming the domain (black arch). **c** Local projections (red) around the globally detected peak loci (relative genomic positions in kb given as numbers in panels) and locally detected peak loci (black).

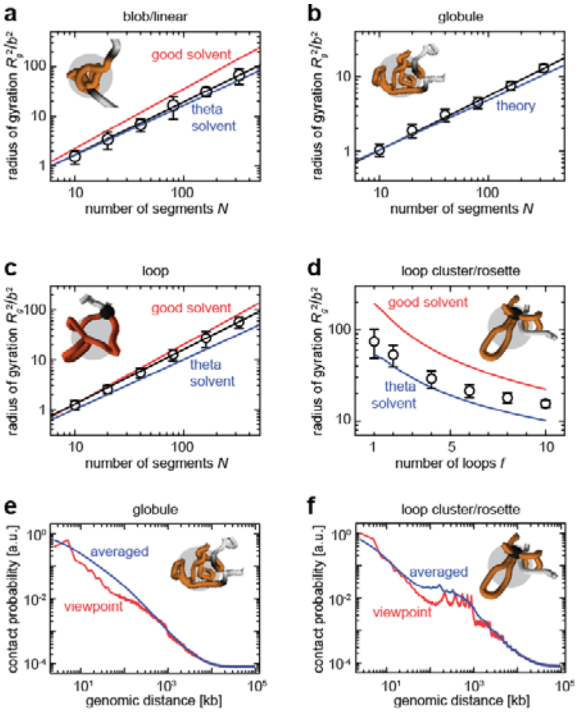

Supplementary Figure S4: Multiscale properties of simulated domain topologies

a To check the validity of the numerical model for chromatin conformations, we determined for 20 simulated conformations the averaged radius of gyration R_g for a linear chain, e.g. in a blob, depending on the number of Kuhn segments N of length b (circles). A fit with a power function (black line) yielded $R_g^2 \sim N^{1.06}$ and lay nicely between the expected dependences for theta- (blue) and good-solvent conditions (red), Equation S14. **b** Same as **a** for a globule. The fit yielded $R_g^2 \sim N^{0.73}$. **c** Same as **a** for a loop and Equation S20. The fit yielded $R_g^2 \sim N^{1.10}$. **d** Same as **a** for a loop cluster/rosette, but for N = 320 segments and depending on the number of loops per domain. The values lay nicely between the expected dependences for theta- (blue) and good-solvent conditions (red), Equation S22 and S23. **e** Linear contact probability calculated for a 20fold repetition of the globular domain configuration used for Fig. 1e and described in Methods, forming a virtual 100 Mb chromosome confined to a ~2.4 µm diameter volume. The viewpoint calculation (red) is based on a fixed first position at the beginning of the chromosome. After an initial steep decay, it shows a region with smaller slope between 100 kb and 1 Mb corresponding to the domain, followed by an again steeper decay that approaches a plateau due to the chromosomal confinement. Alternatively, the probabilities are averaged over all possible combinations (blue), resulting in a less modulated decay. **f** Same as **e** for a 20fold repetition of the loop/rosette domain configuration used for Fig. 1d and described in Methods. The viewpoint calculation (red) shows clear plateaus for the domains superimposed with peaks for the loops. The averaged calculation (blue) mostly features the first domain plateau.

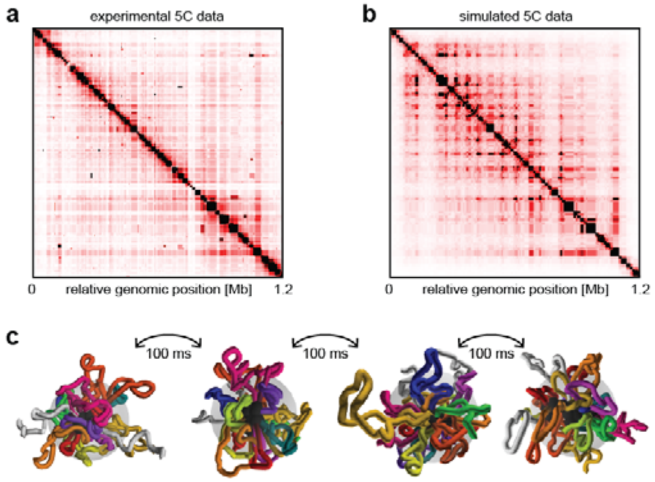

Supplementary Figure S5: Experimental and simulated 5C data and domain structure

a Experimental 5C data [63] corresponding to the highlighted domain in Fig. S2, from which peak locations where extracted. **b** Interpreting them as sequence of genomic site pairs connected by looping allowed to compute a simulated 5C map with Equation (25) at the same sampling, showing good agreement with the experimental map. **c** Renderings of statistically equivalent domain conformations formed by the loops (gray circles: radius of gyration). Transitions between such conformations are the relaxations observed with FCS and occur on the time scale of 100 ms.

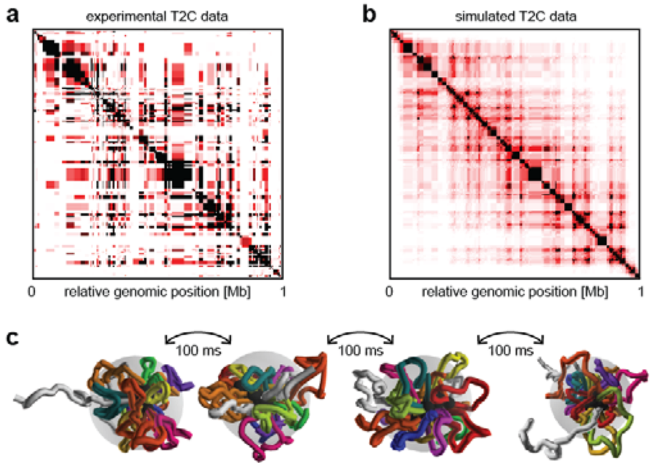

Supplementary Figure S6: Experimental and simulated T2C data and domain structure

a Experimental T2C data [64] corresponding to the highlighted domain in Fig. S3, from which peak locations where extracted. **b** Interpreting them as sequence of genomic site pairs connected by looping allowed to compute a simulated T2C map with Equation (25) at the same sampling, showing good agreement with the experimental map. **c** Renderings of statistically equivalent domain conformations formed by the loops (gray circles: radius of gyration). Transitions between such conformations are the relaxations observed with FCS and occur on the time scale of 100 ms.

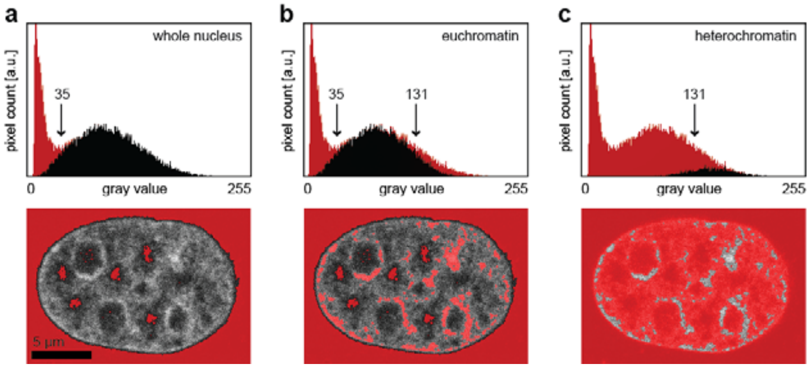

Supplementary Figure S7: Image intensity analysis and classification

a Definition of lower threshold for nuclear segmentation as minimum between background pixels (large peak left) and actual chromatin signal (smaller peak right). Disregarded pixels are highlighted in red both in the histogram and in the image. **b** The upper threshold is defined as described in the Supplementary Text, allowing to segment exclusively the euchromatin contribution. **c** The upper threshold is also used to segment exclusively the heterochromatin contribution.

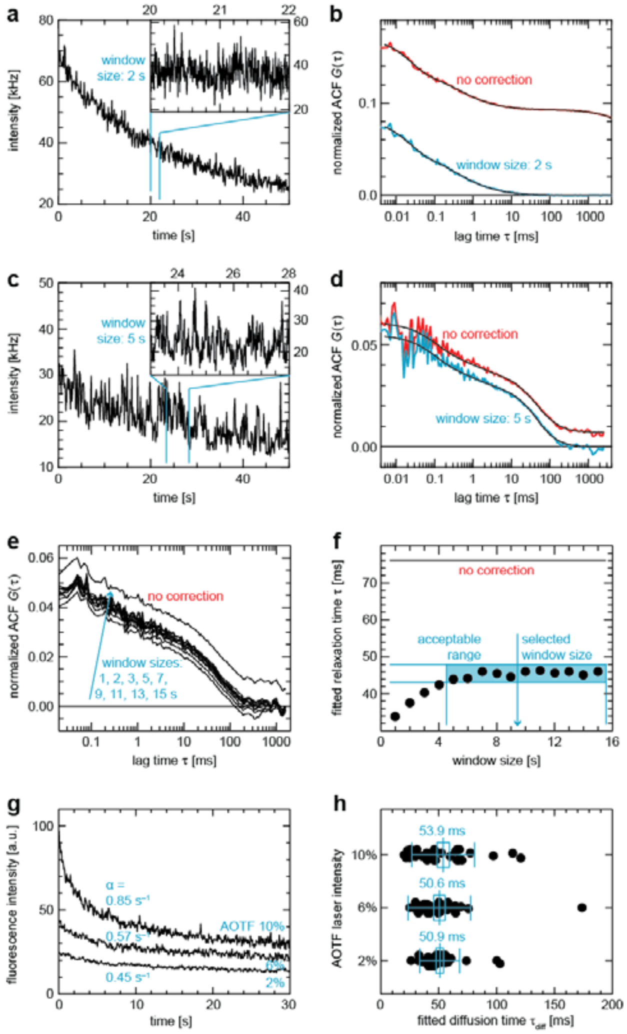

Supplementary Figure S8: FCS in the presence of photobleaching

a Fluorescence intensity trace of EYFP expressed in a HeLa cell [56], showing strong photobleaching. When zooming in to a smaller time window, the intensity is virtually stationary (insert). **b** When conventionally calculating the ACF (red), the photobleaching was reflected by an offset and a shoulder, making further analysis difficult. With a window size of 2 s, the local average-based ACF calculation, Equation S4, yielded an ACF (blue) that could be easily fitted with model functions. **c** Same as **a** for H1-EGFP in MCF7 cells as used in this study. **d** Same as **b** for a window size of 5 s. **e** Dependence of the ACF on the window size, suggesting a range of usable values. **f** Diffusion correlation times from fitting the tails of the AFCs in **e**. Without correction, the fit did not converge properly, whereas for a range of window sizes, we obtained virtually the same number so that a proper choice of the window size could be made as indicated. **g** Fluorescence intensity traces from FCS measurements of H2A-EGFP in a HeLa cell nucleus acquired with different laser intensities (2%, 6% and 10% nominal AOTF transmission), corresponding to 0.2, 0.9 and 2.2 µW excitation at 488 nm). **h** Fitting the resulting correlation functions with a pure diffusion model, Equation 5, yielded diffusion correlation times (slow component from a two-component fit) that did not depend on the laser intensity (N = 31, 31, 29 for the respective intensity values).

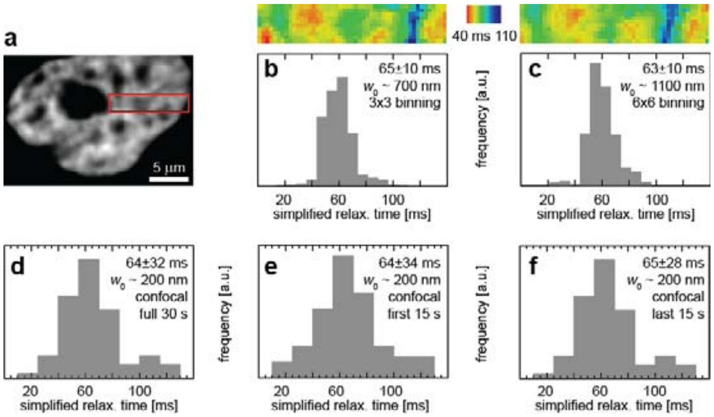

Supplementary Figure S9: Confocal and light-sheet FCS on different scales

a Light-sheet fluorescence intensity image of H2A-EGFP stably expressed in a HeLa cell (see [65] for the light-sheet imaging and 2D-FCS setup and method). Fitting the light-sheet 2D-FCS correlation functions acquired in the red region with a two-component anomalous diffusion model, Equation 5, allowed to generate maps and histograms of diffusion correlation times of the slow component. **b** 3x3 binning results in a focal volume with a radius of ~700 nm and **c** 6x6 binning in a radius of ~1100 nm. For both cases, the distributions of diffusion correlation times are very similar with almost identical mean values and standard deviations. **d** Moreover, extracting the same parameter from ~80 confocal FCS measurements (focal radius ~200 nm) in the same cell line resulted in a similar distribution and virutally the same mean value. If the relaxation times observed here were imaging artifacts, the observed relaxation times/diffusion correlation times would strongly depend on the focal size. However, they do not depend on the focal volume, strongly corroborating the interpretation of the fluctuations as polymer relaxations rather than free diffusion. **e** Analyzing only the first 30 s or **f** the second 30 s of each of the ~80 measurements from **d** yielded very similar distributions and mean values of the diffusion correlation time.

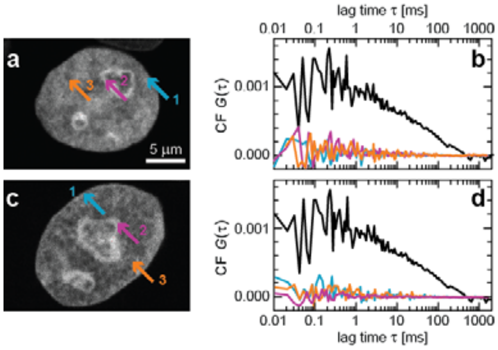

Supplementary Figure S10: FCS in fixed HeLa cells expressing H2A-EGFP

a, c Fixed HeLa cells expressing H2A-EGFP. **b, d** FCS measurements in the nuclear (1) and nucleolar (2) periphery and in the nucleoplasm (3) did not show any significant correlation, indicating that the fixation strongly suppresses the polymer relaxations as seen with FCS.

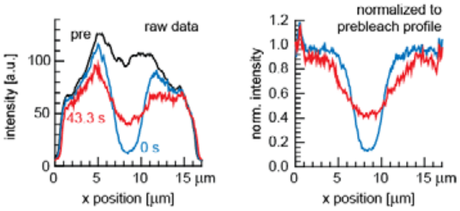

Supplementary Figure S11: Strip profile analysis of FRAP experiments

Intensity profiles extracted from the cell in Fig. 3a for the prebleach (pre), first postbleach (0 s) and a later postbleach time point (43.3 s). To remove the spatial heterogeneity distribution, the profiles were normalized to the prebleach distribution. Then they could be fitted well with Equation S91 to yield apparent diffusion coefficients.

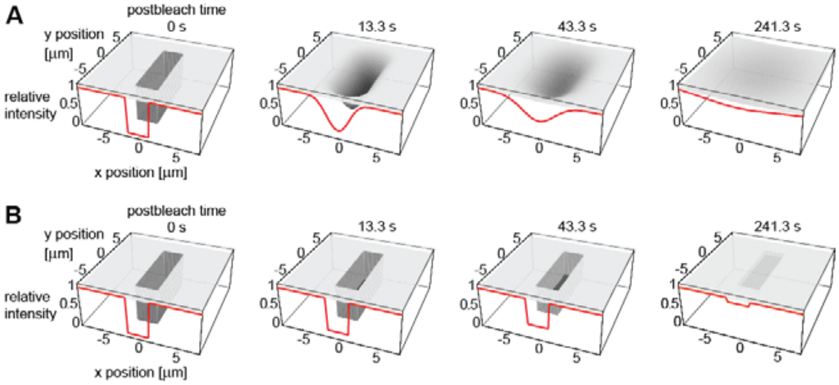

Supplementary Figure S12: Simulated FRAP experiments

a Visualized spatio-temporal distribution of purely diffusive molecules after bleaching a strip into an otherwise homogeneous distribution. The red profile represents the cross-section at $y = 0$. **b** Same as **a**, however, the molecules are immobilized such that bleached ones are only replaced following dissociation and subsequent association of still fluorescent ones. Diffusion is significantly faster than binding. Comparing the profiles revealed that (effective) diffusion contributed significantly to the H1.0 redistribution after photobleaching.

Supplementary References

1. Doi M, Edwards SF: The Theory Of Polymer Dynamics. Oxford: Oxford University Press; 1986.
2. Grosberg AY, Khokhlov AR: Statistical Physics Of Macromolecules. New York: AIP Press; 1994.
3. Berne B, Pecora R: Dynamic Light Scattering. New York: Wiley; 1976.
4. Flory PJ: Principles Of Polymer Chemistry. Ithaca, New York: Cornell University Press; 1953.
5. Kuhn W: Über die Gestalt fadenförmiger Moleküle in Lösungen. Kolloid-Z 1934,68:2-15.
6. Becker NB, Rosa A, Everaers R: The radial distribution function of worm-like chains. Eur Phys J E Soft Matter 2010,32:53-69.
7. Daniels HE: The Statistical Theory of Stiff Chains. Proc Royal Soc Edinburgh A Math 1952,63:290-311.
8. De Gennes PG: Dynamics of Entangled Polymer Solutions. II. Inclusion of Hydrodynamic Interactions. Macromolecules 1976,9:594-598.
9. Freed KF, Edwards SF: Polymer viscosity in concentrated solutions. J Chem Phys 1974,61:3626-3633.
10. Berg OG: Brownian motion of the wormlike chain and segmental diffusion of DNA. Biopolymers 1979,18:2861-2874.
11. Fujii M, Yamakawa H: Moments and Transport Coefficients of Wormlike Rings. Macromolecules 1975,8:792-799.
12. Ba X-W, Zhang S-W, Wang H-J, Wang S-J, Han Y-H: Fractal Dimension of Randomly Branched Polymers in a Good Solvent. Chin Phys Lett 2002,19:1135-1140.
13. Zimm BH, Kilb RW: Dynamics of branched polymer molecules in dilute solution. J Polymer Sci 1959,37:19-42.
14. Zimm BH, Stockmayer WH: The Dimensions of Chain Molecules Containing Branches and Rings. J Chem Phys 1949,17:1301-1314.
15. Belmont AS: Large-scale chromatin organization: the good, the surprising, and the still perplexing. Curr Opin Cell Biol 2014,26:69-78.
16. Dekker J, Rippe K, Dekker M, Kleckner N: Capturing chromosome conformation. Science 2002,295:1306-1311.
17. Gibcus JH, Dekker J: The Hierarchy of the 3D Genome. Mol Cell 2013,49:773-782.
18. Rouse PE: A Theory of the Linear Viscoelastic Properties of Dilute Solutions of Coiling Polymers. J Chem Phys 1953,21:1272-1280.
19. Bloomfield V, Zimm BH: Viscosity, Sedimentation, et Cetera, of Ring- and Straight-Chain Polymers in Dilute Solution. J Chem Phys 1966,44:315-323.
20. Zimm BH: Dynamics of Polymer Molecules in Dilute Solution: Viscoelasticity, Flow Birefringence and Dielectric Loss. J Chem Phys 1956,24:269-278.
21. Pecora R: Spectral Distribution of Light Scattered from Flexible-Coil Macromolecules. J Chem Phys 1968,49:1032-1035.
22. Sorlie SA, Pecora R: A Dynamic Light Scattering Study of a 2311 Base Pair DNA Restriction Fragment. Macromolecules 1988,21:1437-1449.
23. Bixon M: Polymer Dynamics in Solution. Annu Rev Phys Chem 1976,27:65-84.
24. Harnau L, Winkler RG, Reineker P: Dynamic structure factor of semiflexible macromolecules in dilute solution. J Chem Phys 1996,104:6355-6368.
25. Rotne J, Prager S: Variational treatment of hydrodynamic interaction in polymers. J Chem Phys 1969,50:4831-4837.
26. Yamakawa H: Transport Properties of Polymer Chains in Dilute Solution: Hydrodynamic Interaction. J Chem Phys 1970,53:436-443.
27. Zwanzig R, Kiefer J, Weiss GH: On the validity of the Kirkwood-Riseman theory. Proc Natl Acad Sci USA 1968,60:381-386.
28. Seils J, Pecora R: Photon correlation spectroscopy study of a 2311 bp relaxed circular DNA- - applicability of Rouse-Zimm and wormlike chain models. Biochem Soc Trans 1991,19:511-512.
29. Soda K: Theory of the dynamic light scattering properties for circular semiflexible chains in solution. Macromolecules 1984,17:2365-2375.
30. Allegra G, Ganazzoli F: Polymer dynamics in solution. Universal properties vs. individual behaviour in a unified approach. J Chem Soc, Faraday Trans 1997,93:2341-2353.
31. Grest GS, Kremer K, Milner ST, Witten TA: Relaxation of self-entangled many-arm star polymers. Macromolecules 1989,22:1904-1910.

32. Schaper A, Urbanke C, Maass G: Salt dependent changes in structure and dynamics of circular single stranded DNA of filamentous phages of Escherichia coli. J Biomol Struct Dyn 1991,8:1211-1232.
33. Sikorski A: Monte Carlo study of the dynamics of star-branched polymers. Macromol Theo Sim 1993,2:309-318.
34. Ahlrichs P, Everaers R, Dunweg B: Screening of hydrodynamic interactions in semidilute polymer solutions: A computer simulation study. Phys Rev E 2001,64:040501.
35. Freed KF, Perico A: Considerations on the multiple scattering representation of the concentration dependence of the viscoelastic properties of polymer systems. Macromolecules 1981,14:1290-1298.
36. Qian H: A mathematical analysis for the Brownian dynamics of a DNA tether. J Math Biol 2000,41:331-340.
37. Hihara S, Pack C-G, Kaizu K, Tani T, Hanafusa T, Nozaki T, Takemoto S, Yoshimi T, Yokota H, Imamoto N, et al: Local nucleosome dynamics facilitate chromatin accessibility in living mammalian cells. Cell Rep 2012,2:1645-1656.
38. Weidemann T, Wachsmuth M, Knoch TA, Müller G, Waldeck W, Langowski J: Counting nucleosomes in living cells with a combination of fluorescence correlation spectroscopy and confocal imaging. J Mol Biol 2003,334:229-240.
39. Knoch TA: Approaching The Three-Dimensional Organization Of The Human Genome. Ruprecht-Karls-Universität Heidelberg, Fakultät für Physik und Astronomie; 2002.
40. Minton AP: The influence of macromolecular crowding and macromolecular confinement on biochemical reactions in physiological media. J Biol Chem 2001,276:10577-10580.
41. Bonnet G, Krichevsky O, Libchaber A: Kinetics of conformational fluctuations in DNA hairpin-loops. Proc Natl Acad Sci USA 1998,95:8602-8606.
42. Bonnet G, Tyagi S, Libchaber A, Kramer FR: Thermodynamic basis of the enhanced specificity of structured DNA probes. Proc Natl Acad Sci USA 1999,96:6171-6176.
43. Edman L, Mets U, Rigler R: Conformational transitions monitored for single molecules in solution. Proc Natl Acad Sci USA 1996,93:6710-6715.
44. Lumma D, Keller S, Vilgis T, Radler JO: Dynamics of large semiflexible chains probed by fluorescence correlation spectroscopy. Phys Rev Lett 2003,90:218301.
45. McHale K, Mabuchi H: Precise Characterization of the Conformation Fluctuations of Freely Diffusing DNA: Beyond Rouse and Zimm. J Am Chem Soc 2009,131:17901-17907.
46. Petrov EP, Ohrt T, Winkler RG, Schwille P: Diffusion and Segmental Dynamics of Double-Stranded DNA. Phys Rev Lett 2006,97:258101.
47. Shusterman R, Alon S, Gavrinyov T, Krichevsky O: Monomer dynamics in double- and single-stranded DNA polymers. Phys Rev Lett 2004,92.
48. Tothova J, Brutovsky B, Lisy V: Monomer dynamics in single- and double-stranded DNA coils. Eur Phys J E Soft Matter 2007,24:61-67.
49. Cohen AE, Moerner WE: Principal-components analysis of shape fluctuations of single DNA molecules. Proc Natl Acad Sci USA 2007,104:12622-12627.
50. van Kampen NG: Stochastic Processes In Physics And Chemistry. Amsterdam: Elsevier; 1992.
51. Wachsmuth M: Fluoreszenzfluktuationsmikroskopie: Entwicklung Eines Prototyps, Theorie Und Messung Der Beweglichkeit Von Biomolekülen Im Zellkern. Ruprecht-Karls-Universität Heidelberg, Fakultät für Physik und Astronomie; 2001.
52. Baum M, Erdel F, Wachsmuth M, Rippe K: Retrieving the intracellular topology from multi-scale protein mobility mapping in living cells. Nat Comm 2014,5:4494.
53. Swaminathan R, Hoang CP, Verkman AS: Photobleaching recovery and anisotropy decay of green fluorescent protein GFP-S65T in solution and cells: cytoplasmic viscosity probed by green fluorescent protein translational and rotational diffusion. Biophys J 1997,72:1900-1907.
54. Wachsmuth M, Weisshart K: Fluorescence photobleaching and fluorescence correlation spectroscopy: Two complementary technologies to study molecular dynamics in living cells In Imaging Cellular And Molecular Biological Functions. Edited by Shorte SL, Frischknecht F: Springer; 2007: 179-228
55. Wachsmuth M, Weidemann T, Müller G, Hoffmann-Rohrer UW, Knoch TA, Waldeck W, Langowski J: Analyzing intracellular binding and diffusion with continuous fluorescence photobleaching. Biophys J 2003,84:3353-3363.
56. Im K-B, Schmidt U, Kang MS, Lee JY, Bestvater F, Wachsmuth M: Diffusion and binding analyzed with combined point FRAP and FCS. Cytometry A 2013,83:876-889.

57. Brown DT, Izard T, Misteli T: Mapping the interaction surface of linker histone H10 with the nucleosome of native chromatin in vivo. Nat Struct Mol Biol 2006,13:250-255.
58. Carrero G, Crawford E, Hendzel MJ, de Vries G: Characterizing fluorescence recovery curves for nuclear proteins undergoing binding events. Bull Math Biol 2004,66:1515-1545.
59. Catez F, Ueda T, Bustin M: Determinants of histone H1 mobility and chromatin binding in living cells. Nat Struct Mol Biol 2006,13:305-310.
60. Raghuram N, Carrero G, Stasevich TJ, McNally JG, Th'ng J, Hendzel MJ: Core histone hyperacetylation impacts cooperative behavior and high-affinity binding of histone H1 to chromatin. Biochemistry 2010,49:4420-4431.
61. Stasevich TJ, Mueller F, Brown DT, McNally JG: Dissecting the binding mechanism of the linker histone in live cells: an integrated FRAP analysis. EMBO J 2010,29:1225-1234.
62. Görisch SM, Wachsmuth M, Fejes Tóth K, Lichter P, Rippe K: Histone acetylation increases chromatin accessibility. J Cell Sci 2005,118:5825-5834.
63. Nora EP, Lajoie BR, Schulz EG, Giorgetti L, Okamoto I, Servant N, Piolot T, Berkum NLv, Meisig J, Sedat J, et al: Spatial partitioning of the regulatory landscape of the X-inactivation centre. Nature 2012,485:381-385.
64. Kolovos P, van de Werken HJ, Kepper N, Zuin J, Brouwer RW, Kockx CE, Wendt KS, van IWF, Grosveld F, Knoch TA: Targeted Chromatin Capture (T2C): a novel high resolution high throughput method to detect genomic interactions and regulatory elements. Epigenetics & chromatin 2014,7:10.
65. Capoulade J, Wachsmuth M, Knop, M: Quantitative fluorescence imaging of protein diffusion and interaction in living cells. Nat Biotechnol 2011, 29:835-839.